

ABSTRACT

Construction and Implementation of Multiphase Voxel Finite Elements for Use in Stiffness Tensor Prediction of Woven Fiber Composite Laminae

Christopher M. Boise, M.S.M.E.

Mentor: David A. Jack, Ph.D.

As woven fabric composites become a more popular choice of material, it becomes important to understand how various weave, fibers, and resin systems will react under loading. This can be done by performing a finite element analysis (FEA) of the representative volume element (RVE) to calculate the effective stiffness tensor; however, the complex geometry of the RVE makes meshing tedious. This thesis develops two novel multiphase voxel elements (MVEs) that can account for multiple materials within their domain by applying material properties and appropriate strain corrections at the Gauss integration points. Studies performed on simple geometries show exceptional agreement with traditional FEA results, being more accurate than previous MVEs presented in literature. These new MVEs are also used to analyze various woven composite laminae and they also show good agreement with the experimental results presented in literature and studies from traditional finite elements.

Construction and Implementation of Multiphase Voxel Finite Elements for Use in Stiffness Tensor
Prediction of Woven Fiber Composite Laminae

by

Christopher M. Boise, B.S.M.E.

A Thesis

Approved by the Department of Mechanical Engineering

Kenneth W. Van Treuren, Ph.D., Interim Chairperson

Submitted to the Graduate Faculty of
Baylor University in Partial Fulfillment of the
Requirements for the Degree
of
Master of Science in Mechanical Engineering

Approved by the Thesis Committee

David A. Jack, Ph.D., Chairperson

Douglas E. Smith, Ph.D.

Ronald Morgan, Ph.D.

Accepted by the Graduate School

December 2016

J. Larry Lyon, Ph.D., Dean

Copyright © 2016 Christopher M. Boise

All rights reserved

TABLE OF CONTENTS

List of Figures	viii
List of Tables	xii
Acknowledgments	xiv
Dedication	xvi
Chapter 1 Introduction	1
1.1 Research Motivation	1
1.2 Thesis Objectives	4
1.3 Thesis Outline	4
Chapter 2 Literature Review	8
2.1 Introduction to Woven Fabric Composites	8
2.2 Unidirectional Composites	11
2.2.1 Micromechanics of Unidirectional Laminae	11
2.2.2 Macromechanics of Unidirectional Laminates	13
2.3 Analytic Methods for Woven Composite Analysis	16
2.4 Finite Element Methods for Woven Composite Analysis	21
2.4.1 Geometry Generation	22
2.4.2 Alterations to the Finite Element Methods	23
2.4.3 Voxel Methods	26
2.5 The Extended Finite Element Method	30
Chapter 3 The Finite Element Method	33
3.1 The Finite Element Equations for Structural Mechanics	33
3.1.1 Continuum Mechanics First Principles	33
3.1.2 Development of the Weak Form	35
3.1.3 Approximating the Solution	37

3.1.4	From Index to Vector Notation	38
3.1.5	Assembling the Global System	41
3.2	The Linear Hexahedral Element	42
3.2.1	The Master Element	42
3.2.2	The Jacobian	43
3.2.3	Numerical Integration	46
3.3	Solving the Finite Element Problem for Material Stiffness Prediction .	47
3.3.1	Theory of Material Stiffness Property Prediction	48
3.3.2	Problem-Specific Simplifications to the Finite Element Equations	51
3.3.3	Boundary Conditions	53
3.3.4	Partitioning and Solving the Finite Element Equations	55
3.4	Post-Processing	56
Chapter 4 The Multiphase Voxel Element (MVE)		59
4.1	Motivation	59
4.2	Selected Multiphase Voxel Elements	61
4.2.1	Average Stiffness Element (ASE)	62
4.2.2	Basic Multiphase Voxel Element (B-MVE)	63
4.2.3	Tensile Modulus Corrected Multiphase Voxel Element (TMC-MVE)	64
4.2.4	Stiffness Tensor Corrected Multiphase Voxel Element (STC-MVE)	69
4.3	Volume Fraction Studies	74
4.3.1	Description of Test Method	74
4.3.2	Results — Two Isotropic Materials	77
4.3.3	Results — One Isotropic Material and One Transversely Isotropic Material	82
4.3.4	Results — Two Orthotropic Materials	87
4.4	Material Angle Study	92
4.4.1	Description of Test Method	92

4.4.2	Results	94
4.5	Boundary Angle Study	98
4.5.1	Description of Test Method	98
4.5.2	Results – Gauss Point Study	100
4.5.3	Results – Boundary Angle Study	102
4.6	Overall Conclusions	106
Chapter 5	Analysis of Woven Composites using Multiphase Voxel Elements	107
5.1	Structure of MATLAB Code	107
5.2	Analysis of a Plain Weave Composite Lamina	110
5.2.1	Geometry	112
5.2.1.1	Geometric Functions	112
5.2.1.2	Fiber Rotation	115
5.2.2	COMSOL Model	117
5.2.3	Results	119
5.2.3.1	Computation Time	121
5.2.3.2	Convergence	121
5.2.3.3	Comparison of Calculated Engineering Properties	124
5.2.4	Section Conclusion	127
5.3	Analyses of Other Weave Types	128
5.3.1	Twill Weave Lamina	128
5.3.1.1	Geometry	129
5.3.1.2	Results	131
5.3.2	Satin Weave Lamina	134
5.3.2.1	Geometry	134
5.3.2.2	Results	137
5.4	Concluding Remarks	140
Chapter 6	Conclusion	142
6.1	Revisiting the Thesis Objectives	142

6.1.1	Extend the Work of Caselman	143
6.1.2	Determine the Effectiveness of the MVEs	144
6.1.3	Expose the Shortcomings	145
6.2	Recommendations for Future Work	146
6.2.1	The Extended Finite Element Method	146
6.2.1.1	Theory	147
6.2.1.2	Applications in Composites	150
6.2.2	Recommendations	152
Appendix A	MATLAB Code for ASE	157
Appendix B	MATLAB Code for B-MVE	159
Appendix C	MATLAB Code for TMC-MVE	161
Appendix D	MATLAB Code for STC-MVE	164
Bibliography	167

LIST OF FIGURES

2.1	A comparison of a carbon fiber cello bow (left) with a pernambuco wood bow (right)	10
3.1	The numbering scheme for the stress tensor σ_{ij} (left) and for the strain tensor ε_{ij} (right). The schemes used are identical.	35
3.2	A general domain Ω with surface Γ and surface normal $\hat{\mathbf{n}}$. An element with domain Ω_e and surface Γ_e is also depicted.	36
3.3	The master element with domain $\hat{\Omega}_e$ for a linear hexahedral element in the local coordinates (ξ_1, ξ_2, ξ_3)	44
3.4	The Jacobian J_{ij} maps a deformed element Ω_e in the x_i coordinate system to the master element $\hat{\Omega}_e$ in the ξ_i coordinate system	44
3.5	An example of a cuboid representative volume element (RVE), with applied strains $\bar{\varepsilon}_{ij}$ and dimensions labeled.	51
3.6	A three-noded one-dimensional periodic system	55
4.1	The process for using traditional finite elements versus the process for using MVEs. For MVEs, the geometry can be considered as the system is being solved for.	62
4.2	A visual depiction of the spring analogy used by Caselman [1]	65
4.3	A visual demonstration showing which stiffness tensor components are accounted for in the axial effective stiffness components C_{iii}^{eff} . The white point is the integration point in question.	71
4.4	A visual demonstration showing how the shear stiffness tensor components are accounted for in the calculation of the effective shear stiffness component C_{2323}^{eff} . The white point is the integration point in question	72
4.5	The volume fraction study	75

4.6	An example of the “stairstep–like” plot produced when the stiffness component is evaluated at an arbitrary number of volume fractions. The vertical dashed lines represent the locations of Gauss points. . . .	77
4.7	The values of the stiffness tensor C_{ijkl} vs. volume fraction (V_f) for the two isotropic material system	79
4.8	The error of the stiffness tensor Err_{ijkl} vs. volume fraction (V_f) for the two isotropic material system, calculated using Equation (4.29)	80
4.9	The values of the stiffness tensor C_{ijkl} vs. volume fraction (V_f) for the isotropic/transversely isotropic material system	84
4.10	The error of the stiffness tensor Err_{ijkl} vs. volume fraction (V_f) for the isotropic/transversely isotropic material system, calculated using Equation (4.29)	85
4.11	The values of the stiffness tensor C_{ijkl} vs. volume fraction (V_f) for the two orthotropic material system	89
4.12	The error of the stiffness tensor Err_{ijkl} vs. volume fraction (V_f) for the two orthotropic material system, calculated using Equation (4.29)	90
4.13	The material angle study	93
4.14	The definitions of θ and ϕ , which define the coordinate system which material properties are rotated to.	94
4.15	The values of the stiffness tensor C_{ijkl} vs. material rotation angles θ and ϕ	96
4.16	The error of the stiffness tensor Err_{ijkl} vs. material rotation angles θ and ϕ , calculated using Equation (4.29)	97
4.17	The boundary angle study	99
4.18	The mesh for the true solution to boundary angle study for $\theta = 50^\circ$	100
4.19	The relative error of the MVEs versus the number of Gauss points. The dashed line represents 5% error, and the dashed–dotted line represents 1% error.	101

4.20	The values of the stiffness tensor C_{ijkl} vs. the boundary angle θ . . .	103
4.21	The error of the stiffness tensor Err_{ijkl} vs. the boundary angle θ , calculated using Equation (4.29)	104
5.1	The structure of the MATLAB code used in the finite element analyses performed with MVEs	108
5.2	A picture of carbon fiber plain weave fabric	111
5.3	Top and side views of a plain weave composite lamina. Fill strands (f) are represented in red, and warp strands (w) are represented in green.	112
5.4	2D cut-plane view of a plain-weave woven composite, with geomet- ric functions labeled. (a) View along the positive x_2 -axis to highlight geometry of fill, and (b) view along the positive x_1 -axis to highlight geometry of warp	113
5.5	The plain weave woven geometry as modeled in COMSOL. (a) The full RVE model domain, (b) the full RVE with the matrix is removed, and (c) the quarter RVE without matrix to highlight the tow geometry. .	117
5.6	The plain weave woven geometry as meshed in COMSOL, with (a) 1,064 elements, (b) 19,600 elements, and (c) 68,968 elements.	118
5.7	The relative error defined in Equation (5.12) of select engineering prop- erties through analysis in COMSOL. By 4,000 elements, most of the values converge to within 1% of the “true” solution	120
5.8	The relative error as defined in Equation (5.12) of select engineering stiffness properties through analysis of the plain weave lamina with the MVEs. The planar-to-thickness element ratio is 4:1	123
5.9	A picture of carbon fiber 2/2 twill weave fabric	128
5.10	Top and side views of 2/2 twill weave composite lamina. Fill strands (f) are represented in red, and warp strands (w) are represented in green.	129
5.11	A picture of a type of carbon fiber 5HS satin weave fabric	134

5.12	Top and side views of a 5–harness satin weave composite lamina. Fill strands (f) are represented in red, and warp strands (w) are represented in green.	135
5.13	The relative error as defined in Equation (5.12) of select engineering properties through analysis of the 8HS satin weave lamina with the MVEs.	139

LIST OF TABLES

4.1	List of all of the equations to determine the strain corrections for the STC–MVE	73
4.2	The properties of the two isotropic materials used in this study, adapted from [2]	78
4.3	The percent integral absolute error for the isotropic study, calculated using Equation (4.30)	81
4.4	The properties of the isotropic material (vinylester) and the transversely isotropic material (E–glass/vinylester) used in this study, from [3]	83
4.5	The percent integral absolute error for the isotropic/transversely isotropic study, calculated using Equation (4.30)	86
4.6	The properties of the two orthotropic materials (E–glass/vinylester composite and carbon/bakelite composite) used in this study, from [3]	88
4.7	The percent integral absolute error for the orthotropic study, calculated using Equation (4.30)	91
4.8	The percent integral absolute error for the material angle study, calculated using Equation (4.36)	95
4.9	The percent integral absolute error for the boundary angle study, calculated using Equation (4.38)	105
5.1	The geometric parameters of the plain weave lamina studied, from [3]	116
5.2	The properties of the plain weave lamina matrix (vinylester) and fiber tow (E–glass/vinylester) used in this study, from [3]	116
5.3	Comparison of computation time for the STC–MVE using various combinations of optimization methods	121
5.4	The calculated values of the plain weave lamina engineering stiffness properties with the MVEs, classic finite elements, and experimental values from [3]	125

5.5	The percent absolute error for the MVEs in the plain weave study as compared to COMSOL, calculated using Equation (5.14)	126
5.6	The geometric parameters of the 2/2 twill weave lamina, from [3] . . .	131
5.7	The properties of the 2/2 twill weave lamina matrix (Bakelite) and fiber tow (carbon/Bakelite) used in this study, from [3]	131
5.8	The MVE calculated values of the engineering stiffness properties of the twill weave compared against analytic and experimental results from [3]	132
5.9	The STC–MVE calculated values of the adjusted engineering stiffness properties of the twill weave compared against analytic and experimental results from [3]	133
5.10	The geometric parameters of the 8HS weave lamina studied, from [3]	136
5.11	The properties of the 8HS weave lamina matrix (epoxy) and fiber tow (E-glass/epoxy) used in this study, from [3]	136
5.12	The MVE calculated values of the engineering stiffness properties of the 8HS weave compared against analytic and experimental results from [3]	138

ACKNOWLEDGMENTS

First of all, I'd like to thank God for His love and support through this journey to obtain my master's degree. Without His strength and power, I would not have been able to finish. I thank Him for gifting me with the talents required to perform this research. May this thesis be an offering to Him for His glory.

I'd like to thank Dr. David Jack for his mentorship and support as I waded through the turbulent waters of research. His guidance was much appreciated and I learned much under him. I'd also like to thank him for his patience and jovial nature, even in the moments I was stubborn, being a perfectionist, or setting the fire alarms off in Rogers. I'd like to thank my other committee members, Dr. Douglas Smith and Dr. Ron Morgan, for being willing to read this behemoth of a thesis and provide suggestions on how to refine it.

I owe my family a huge thank you for their support. Thank you, Dad, for affording me the opportunity to pursue a passion of mine — even if it did mean not finding a job for another two years. Thank you, Mom, for supporting me spiritually and continually praying for me as I fought my battles. Thank you, Krystle and Josh, for your continual support and for keeping things light-hearted as I was busy microwaving plastic. And Krystle, to you I concede that, while I did get the brains of the family, you did get the better hair.

I would also like to thank the Ainsworth and Thomasy families for being my family away from my family here in Waco. You guys provided me with the

local support I needed to make it through this time. I'd also like to thank my close friends — especially Kaylee Sirovy, Jeff Cross, Travis Engel, Brian Crowder, Billy Kretschmer, Justin Keys, and Ethan Harlow. Without you guys, I would be a mess. Your prayers, support, guidance, and laughter have truly been a blessing when I was under a lot of pressure. Thank you.

To my fellow researchers — Ben Blandford, Colin Gregg, Jake Christoph, and Blake Heller — thanks for keeping me humble by making sure every mistake I made was held over my head for days at a time. Thanks for making sure the tone of the office never got too serious by continually using sarcasm. And thanks for making me paranoid about whether there was an air horn duct taped under my chair. This thesis was stressful enough; the last thing I needed was coworkers who took things too seriously.

I'd like to thank L3 Communications for their financial support. Without their funding, I would not have chosen to pursue this degree. Finally, I'd like to thank Baylor University for providing an atmosphere where I could learn about engineering through the lens of faith.

To the Creator of all things:

Thank you for engineering a world full of wonder—

A world that we can freely explore

And always be pointed back to Your beauty

CHAPTER ONE

Introduction

1.1 Research Motivation

In the past 40 years, woven fabric composites and other composite materials have become increasingly popular in many industries such as the automotive and aerospace industries. They are often favored over traditional materials such as steel and aluminum because they are much lighter while providing similar stiffness properties; this high strength-to-weight ratio can help provide savings in fuel costs.

Another growing application is in the world of musical instruments; because carbon fiber composites are more resistant to humidity and temperature change than wood is, some luthiers are creating more durable stringed instruments that can be used in more rugged applications, such as the outdoors. Further, this change from wood to laminated composites is also ecologically friendly. Traditionally, bows are made of pernambuco wood, but this is becoming an endangered species; carbon fiber bows can provide a superior sound quality at the mid-range price level [4].

With the growing applications of woven fabric composites, it has become necessary to understand how these materials will react to specific loading conditions, namely structural loading. In structural mechanics, the stress tensor σ_{ij} and the strain tensor ε_{ij} in the linear elastic regime are related through the stiffness tensor C_{ijkl} , a fourth-order tensor that can have up to 21 independent constants depending upon the degree of anisotropy. The stiffness tensor is an intrinsic property of the material in question (see e.g., [5]). Determining this stiffness tensor for a material is the key to characterizing the structural response of the material.

For metals in general, the stiffness tensor C_{ijkl} is simpler to characterize through experiment because metals are homogeneous and often isotropic, being dependent only upon two stiffness properties (see e.g., [6]). For woven fabric composites — heterogeneous structures that may be fully anisotropic — the stiffness tensor is dependent upon all 21 stiffness properties that are not always directly measurable through experiment (see e.g., [6]). Many woven fabrics have sufficient geometry symmetry that they may be considered orthotropic with nine independent stiffness parameters. Further, because woven fabric composites are manufactured structures created from combining two separate materials, manufacturing consistent test samples is often tedious and time-consuming. Therefore, alternative means of determining the stiffness tensor C_{ijkl} are required.

Because the properties of constituent materials of a woven fabric composite (the fiber tow and matrix) are easily determined through the use of experiments and micromechanics models, much focus has been placed on determining the stiffness tensor at the mesomechanical level; that is, the level of an individual lamina where the woven geometry of the fiber tows within the matrix are in effect. These properties can be determined by analyzing a representative volume element (RVE) of the composite, which is defined as the smallest repeating unit of a geometry that can build a woven composite.

These analyses historically were performed analytically through the use of closed-form geometric functions, but today, numerical methods, namely finite element analysis (FEA), is often preferred as it uses fewer assumptions about the stress and strain fields. FEA is a numerical analysis technique whereby a partial differential equation can be solved over a discretized domain via a set of linear algebraic equations. The geometry in FEA can be modeled without having to define closed-form geometric

functions. While spline functions are still used to build woven geometries (see e.g., [7]), geometry data can potentially be extracted pointwise from a three-dimensional ultrasound scan (see e.g. [8]) or a micro CT scan (see e.g. [9, 10]) and analyzed using FEA.

However, in order for a finite element analysis to be performed, the geometry of the RVE has to be discretized into a set of elements. These elements traditionally have to cohere to material boundaries because each one can only have one set of continuous material properties within their domain. This poses a problem for woven composite geometries because their internal structure is often quite complex; very small elements are required to accurately define geometry which can sometimes become ill-conditioned, which leads to high memory costs and numerical instabilities in the solution.

One of the methods presented in the literature to circumvent this issue is to instead apply the stiffness tensor C_{ijkl} at the integration points within the element instead of the element as a whole (see e.g., [1, 11, 12]). With this type of approach, the mesh can be built independent of the geometry, and therefore, a consistent mesh can be created without the risk of ill-conditioned elements. The use of these elements are termed voxel methods in some applications.

Lippmann *et al.* [11] and Zeng [12] simply applied the corresponding stiffness tensor at each Gauss point, but Caselman [1] determined this approach was not sufficient for accuracy. He extended this method by including strain corrections at each integration point for applications in short fiber composites with reasonable success. While this element developed was a step in the right direction, there is more room for greater accuracy in the transverse shear stiffness terms; further, this method can be applied to woven composites.

1.2 Thesis Objectives

The objective of the research presented in this thesis is to

Construct a multiphase voxel finite element (MVE) allowing the construction of a mesh independent of internal geometry variations by incorporating material properties determined at the integration points for use in correctly predicting the averaged material stiffness tensor C_{ijkl} over the representative volume element (RVE) of a woven fabric composite lamina.

In broad terms, the research aims to

- Expand upon the work of Caselman [1] by generalizing the strain correction factors within the MVE formulation to better account for the shear effect
- Determine the effectiveness of the existing methods that can be expressed in the general MVE form proposed in this thesis and the two newly proposed MVEs in calculating the averaged stiffness tensor C_{ijkl} of woven fabric composite laminae
- Expose shortcomings of the investigated MVEs in order to suggest further improvements and demonstrate the improved performance of the two newly proposed MVEs

1.3 Thesis Outline

Chapter Two begins with a broad overview of the currently available literature applicable to the stiffness property prediction of woven composite laminae. A discussion on some unidirectional micromechanics models are presented first, followed by several analytic methods that laid the foundation for woven fiber composite stiffness property prediction with particular attention given to MESOTEX [3, 13] for later comparisons. This is followed by a presentation of several methods that utilize finite elements to perform woven composite analyses. Various techniques in applying FEA

will be looked at to show how previous researchers overcame the obstacle of analyzing a woven composite RVE. A close look at voxel elements will be presented as it forms the basis of this thesis. Finally, a brief overview of the extended finite element method (XFEM) will be presented; future applications of MVEs in XFEM will be left to the future work chapter.

Chapter Three presents the derivation of the finite element method for three-dimensional structural mechanics; this derivation intends to provide a basic demonstration of how the finite element process works and to form the basis for Chapter 4. The methods on how to solve the finite element equations will focus specifically on how to obtain the stiffness tensor C_{ijkl} from a heterogeneous structure.

Chapter Four will introduce the formulation of the four multiphase voxel elements (MVEs) studied in this research. The four MVEs are

1. The Average Stiffness Element (ASE), constructed by determining the volume average of each component of the stiffness tensor. The ASE is similar to the volume fraction-based homogenization method presented by Kim and Swan [14] and Watanabe *et al.* [15].
2. The Basic Multiphase Voxel Element (B-MVE), constructed as described in Zeng *et al.* [12].
3. The Tensile Modulus Corrected Multiphase Voxel Element (TMC-MVE), a newly developed MVE adapted from the element of isotropic materials used by Caselman [1] with enhancements presented in this thesis for use with orthotropic materials.
4. The Stiffness Tensor Corrected Multiphase Voxel Element (STC-MVE), a newly developed MVE utilizing components of the stiffness tensor for strain correction, as well as improved methods for accounting for shear stiffness.

These MVEs will then be used to determine the stiffness properties of simple geometries using custom MATLAB code. The first test developed to provide a comparison is the volume fraction test to determine how a shifting material boundary affects the accuracy of the MVEs. The second test, the material angle test, determines how the MVEs are affected by a rotating material reference frame. Finally, the boundary angle test seeks to determine the effect of an angled boundary on the MVEs.

Chapter Five applies the MVEs to the determination of the material stiffness tensor of various woven fiber composite laminae using code written in MATLAB. Specifically, a plain weave composite lamina is defined using geometric functions adapted from Scida *et al.* [13], and then analyzed using the MVEs. These results are compared to the results provided from COMSOL Multiphysics, a commercial finite element code, and experimental results from Scida *et al.* [3] to complete the validation of the model. The chapter concludes with studies of satin and twill weave composite laminae to demonstrate the versatility of the MVEs.

Chapter Six concludes the thesis by revisiting the objectives presented in Section 1.2. Each objective is thoroughly discussed using the results from the previous chapter. Also included is a discussion of future work, including potential ways to unite the MVEs with the extended finite element method (XFEM). XFEM is an emerging area of research; it includes the ability to enrich the solution space of the element, allowing for higher resolution within the element without the addition of nodes. Because XFEM and the MVEs have similar goals (the modeling of material discontinuities within an element), there is potential ground to use both methods together. Some applications of XFEM to composites from the literature will also be

described. Finally, recommendations for future work will be provided, including improvements to the MVEs, the ways to test the MVEs, and the MATLAB code used in this research.

CHAPTER TWO

Literature Review

This chapter will introduce the motivation and background behind the analysis of laminated woven composites. A discussion will be had on some of the key analytic and numerical techniques previously developed for stiffness property prediction of heterogeneous materials. Further, discussion on some new emerging techniques in finite elements that are currently being studied will be presented.

2.1 Introduction to Woven Fabric Composites

A fiber-reinforced polymer (FRP) is a composite material system composed of two materials: a fiber and a polymer matrix. The matrix material in this research is a thermosetting epoxy, but thermoplastics are also common. The thermoset resin can be easily poured or molded into the desired shape, and, after curing, can hold that desired shape. The polymeric material does not have the stiffness or strength properties needed for the applications desired; thus they require some form of reinforcement in order to be useful in structural applications.

The fiber reinforcing material is often glass, carbon, boron, etc., with the selection made based on the desired application. Due to some limiting factor (cost to manufacture, difficult to manufacture, high weight, etc), it is not prudent or sometimes even possible to use this material in bulk. There is often a desire to use as little of the reinforcing material as possible.

The fiber and polymer matrix are combined because the strengths of one complement the weaknesses of other. When a material is manufactured into a fiber, it exhibits similar or even enhanced tensile properties when compared to the bulk

form [6], but it loses any bending stiffness. For example, even though steel is a very stiff metal, it easily “droops” under its own weight when made into a rod. However, when a fiber material is combined with a matrix material to hold the fiber into the shape for the desired application; the matrix acts as a binder to prevent the fibers from moving. Even though the manufactured composite is not as stiff or strong as the fiber reinforcing material by itself [6], the other properties of the composite (shapability, strength-to-weight ratio, etc.) make this heterogeneous structure more versatile than the individual constituent materials.

There are many different methods to manufacture FRPs. Chopped fiber-filled polymers are obtained by mixing short or long fibers into a preferential orientation state such as in compression or injection molding. Alternatively, continuous fibers can be braided together and held in place by infusing the braided fibers with polymer matrix. The manufacturing method studied in this research is a method whereby the individual fibers are formed into a strand, then the strands are woven together into a fabric. This fabric is then infused with a low viscosity polymer matrix, and the matrix is allowed to cure while holding the desired shape. The produced part with woven fabrics and a polymer matrix will be called a woven fabric composite in this thesis.

In the early 1980s, woven fabric composite materials, especially unidirectional and woven composites, saw a growth in the number of applications, especially in structural applications (see e.g., [16]). In both the automotive and aerospace industries, the high strength-to-weight ratio of FRP composites is quite desirable, particularly as the demand for more fuel-efficient vehicles continues to grow. These relatively light structures can replace traditional, and heavier, metals such as aluminum and steel in the structure of the vehicles to save on fuel costs. In the music industry,

the acoustic properties of carbon fiber have been found to be comparable to that of the oft preferred pernambuco wood for stringed-instrument bows [4]. As the world supply of pernambuco wood has diminished due to consumer demand, there is a push to switch to carbon fiber bows. In some instances, carbon fiber bows are more durable, cheaper, more resistant to temperature and humidity, and match the sound quality of similarly-priced pernambuco bows [4]. A comparison of a carbon fiber and pernambuco bow is provided in Figure 2.1.



Figure 2.1: A comparison of a carbon fiber cello bow (left) with a pernambuco wood bow (right)

To further the use of fiber reinforced composites, effective and accurate methods to quantify the material properties of these woven composites is desired. While experimental standards are available to determine the stiffness properties of these laminae (see e.g., [17]), the methods require the fabrication of many samples. This is a costly and time-prohibitive process, especially if it is desired to determine a suitable system from a broad selection. This becomes prohibitive as the number of design variables in woven composites is quite high, and there often are several valid options for a desired set of performance metrics. A number of analytic and numerical methods have therefore been developed to predict the properties of composite

laminae. Unlike homogeneous metals, the heterogeneous nature of these composites require that the interaction between the fiber and matrix materials are considered when estimating their material properties.

2.2 Unidirectional Composites

Unidirectional composites are FRPs where the fibers are all aligned in one direction; this provides the best strength and stiffness properties in the direction of the fibers. While unidirectional composites are not specifically analyzed in this research, some of the methods used for their analysis form the basis of the discussion of woven composites. Specifically, the micromechanical models for individual laminae of unidirectional fibers is used to provide the material properties of an infused fiber bundle in a woven lamina. Similarly, the macromechanical laminate analysis methods provide the basis for the earliest analytic models for woven composites (see e.g., [18]).

2.2.1 Micromechanics of Unidirectional Laminae

When referring to the micromechanics of unidirectional laminae, the mechanics of how a single fiber interacts with the surrounding matrix are in consideration. Extensive research has been performed into analytic models that are able to predict the mechanical properties of a discontinuous fiber in matrix; these models are often functions of the aspect ratio of the fiber, labeled α and defined as

$$\alpha = \frac{\ell}{d} \tag{2.1}$$

where ℓ is the length of the fiber, and d is the diameter. Fortunately, it has been shown in literature (see e.g., [19]) that for large aspect ratios ($\alpha \gtrsim 100$), the fibers are often considered to be infinitely long. In the case of unidirectional laminae, they often have aspect ratios much greater than 100. The discontinuous fiber models with

a large aspect ratio as the input can be used to predict the micromechanical behavior of a fiber infused with resin (assuming the fiber is straight).

The most commonly used micromechanics model used in industry is the Halpin–Tsai model [20] due to its algebraic simplicity, but not necessarily its accuracy. The material properties of the fiber composite that are affected by changes in aspect ratio (E_{11} , G_{12} , and ν_{12}) are represented as simple ratios of the constituent material properties of the fiber (E_f , G_f , ν_f) and matrix (E_m , G_m , ν_m), the aspect ratio α of the fiber, and the volume fraction of the fiber V_f as

$$\frac{E_{11}}{E_m} = \frac{1 + \eta V_f}{1 - \eta V_f}, \quad \text{where} \quad \eta = \frac{\frac{E_f}{E_m} - 1}{\frac{E_f}{E_m} + 2\alpha} \quad (2.2)$$

$$\frac{G_{12}}{G_m} = \frac{1 + \eta V_f}{1 - \eta V_f}, \quad \text{where} \quad \eta = \frac{\frac{G_f}{G_m} - 1}{\frac{G_f}{G_m} + 1} \quad (2.3)$$

$$\nu_{12} \sim V_f \nu_f + (1 - V_f) \nu_m \quad (2.4)$$

Despite the popularity of the Halpin–Tsai equations, there are several models that have been developed that are more accurate. Tucker and Liang [21] provide a review of the more common micromechanics models and validate the results, using a finite element model as a reference for comparison. They determined that, of the models tested, Mori–Tanaka type models [22] provided the best predictions. The Mori–Tanaka model is based on a theory from Eshelby [23] for an ellipsoidal inclusion in an infinite matrix; the authors expanded the model from Eshelby to include fiber interaction through the stress field, and therefore predict the stiffness with greater accuracy for higher volume fractions.

Tandon and Weng [19], a Mori–Tanaka type model, expanded the average stress and strain formulations of Mori and Tanaka with further use of Eshelby’s tensor. Further, the Tandon–Weng formulation include calculations for all material properties, not just the ones that are affected by changing aspect ratio. One drawback to

this method is the requirement that ν_{12} be calculated iteratively, but Tucker and Liang [21] provide an alternate closed-form formulation.

The Halpin–Tsai and Tandon–Weng methods were both analyzed by Gusev *et al.* [24] and compared against a finite element model. The conclusion was that the Halpin–Tsai equations poorly predicted the models analyzed. The Tandon–Weng model provided reasonable results for composites of high aspect ratio and low volume fraction.

Unidirectional analyses have also been performed in finite element packages. It has already been mentioned that Tucker and Liang [21] used a finite element model to determine the accuracy of some analytic models. Sun and Vaidya [2] presented a means to predict the overall elastic constants of a heterogeneous periodic structure by averaging the stress and strain fields. Xia *et al.* [25] provided a means of applying periodic boundary conditions to a periodic structure without overconstraining the system. These new boundary conditions allow opposite material boundaries to displace in relation to each other without overconstraining the system by forcing the boundaries to remain planar, like previously accepted boundary conditions did.

2.2.2 Macromechanics of Unidirectional Laminates

The macromechanics of a unidirectional laminate refers to how an infused stack of multiple unidirectional laminae at various orientations interact to affect the overall properties of the entire laminate. A short discussion of the macromechanical theory is included as the theory behind this analysis forms the basis of the earliest woven composite analytic models (see e.g., [18]).

Classical laminate theory (CLT) provides a means to calculate the planar strain properties of a laminate undergoing loads and moments. CLT uses the two-dimensional rotated stiffness matrix of each lamina in a stack to relate the applied

forces and moments to the resulting mid-plane strains and curvatures (or vice versa). A reduced presentation of CLT will be presented here, based on the full discussion found in Jones [6].

CLT is developed with the following assumptions (see e.g., [6])

- Plane stress ($\sigma_z = \sigma_{xz} = \sigma_{yz} = 0$)
- Thin laminate ($\varepsilon_z = \gamma_{xz} = \gamma_{yz} = 0$)
- Linear elastic
- Homogeneous stiffness through the thickness of each lamina

The planar stress vector $[\boldsymbol{\sigma}]_k$ and strain vector $[\boldsymbol{\varepsilon}]_k$ of the k^{th} composite lamina in a stack of N laminae (with $k = 1$ being the top lamina) can be related through the rotated planar material stiffness matrix $[\bar{\mathbf{Q}}]_k$ as [6]

$$[\boldsymbol{\sigma}]_k = [\bar{\mathbf{Q}}]_k [\boldsymbol{\varepsilon}]_k \quad (2.5)$$

where

$$[\boldsymbol{\sigma}]_k = \begin{bmatrix} \sigma_x & \sigma_y & \sigma_{xy} \end{bmatrix}_k^\top \quad (2.6)$$

$$[\boldsymbol{\varepsilon}]_k = \begin{bmatrix} \varepsilon_x & \varepsilon_y & \gamma_{xy} \end{bmatrix}_k^\top \quad (2.7)$$

$$[\bar{\mathbf{Q}}]_k = \begin{bmatrix} \bar{Q}_{11} & \bar{Q}_{12} & \bar{Q}_{16} \\ \bar{Q}_{12} & \bar{Q}_{22} & \bar{Q}_{26} \\ \bar{Q}_{16} & \bar{Q}_{26} & \bar{Q}_{66} \end{bmatrix}_k \quad (2.8)$$

The value of $[\bar{\mathbf{Q}}]_k$ can be determined for each lamina by taking the reduced stiffness matrix tensor expressed only in terms that contribute to the plane stress $[\mathbf{Q}]_k$ and rotating it at the angle of the lamina θ_k using the rotation matrix $\mathbf{T}(\theta_k)$ as [6]

$$[\bar{\mathbf{Q}}]_k = [\mathbf{T}(\theta_k)]^{-1} [\mathbf{Q}]_k [\mathbf{T}(\theta_k)]^{-\top} \quad (2.9)$$

where $-\top$ refers to the transpose of the inverse, and

$$\mathbf{T}(\theta) = \begin{bmatrix} \cos^2 \theta & \sin^2 \theta & 2 \sin \theta \cos \theta \\ \sin^2 \theta & \cos^2 \theta & -2 \sin \theta \cos \theta \\ -\sin \theta \cos \theta & \sin \theta \cos \theta & \cos^2 \theta - \sin^2 \theta \end{bmatrix} \quad (2.10)$$

$$[\mathbf{Q}]_k = \begin{bmatrix} Q_{11} & Q_{12} & 0 \\ Q_{12} & Q_{22} & 0 \\ 0 & 0 & Q_{66} \end{bmatrix}_k \quad (2.11)$$

The individual $[\bar{\mathbf{Q}}]_k$ can be related by first splitting the strain vector $[\boldsymbol{\varepsilon}]_k$ into a vector of strains $[\boldsymbol{\varepsilon}^\circ]_k$, located at the mid-plane of a laminate stack, and a vector of mid-plane curvatures $[\boldsymbol{\kappa}]_k$ as

$$[\boldsymbol{\varepsilon}]_k = [\boldsymbol{\varepsilon}^\circ]_k + z[\boldsymbol{\kappa}]_k \quad (2.12)$$

where z is the coordinate along the laminate thickness from the mid-plane of the laminate. This reduction can be made under the Kirchhoff hypothesis, which assumes the laminae are thin plates (see e.g., [6]).

The second step is to integrate the stresses to calculate the reaction forces \mathbf{N} and reaction moments \mathbf{M} per unit thickness as (see e.g., [6])

$$\mathbf{N} = \int_{-\frac{t}{2}}^{\frac{t}{2}} \boldsymbol{\sigma} dz \quad \mathbf{M} = \int_{-\frac{t}{2}}^{\frac{t}{2}} z \boldsymbol{\sigma} dz \quad (2.13)$$

where t is the full thickness of the laminate. The result of using (2.12) in (2.5) and then integrating with (2.13) results in

$$\begin{bmatrix} \mathbf{N} \\ \mathbf{M} \end{bmatrix} = \begin{bmatrix} \mathbf{A} & \mathbf{B} \\ \mathbf{B} & \mathbf{D} \end{bmatrix} \begin{bmatrix} \boldsymbol{\varepsilon}^\circ \\ \boldsymbol{\kappa} \end{bmatrix} \quad (2.14)$$

where

$$A_{ij} = \sum_{k=1}^N (\bar{Q}_{ij})_k (z_k - z_{k-1}) \quad (2.15)$$

$$B_{ij} = \sum_{k=1}^N (\bar{Q}_{ij})_k (z_k^2 - z_{k-1}^2) \quad (2.16)$$

$$D_{ij} = \sum_{k=1}^N (\bar{Q}_{ij})_k (z_k^3 - z_{k-1}^3) \quad (2.17)$$

where z_k refers to the z -coordinate of the bottom of the k^{th} lamina.

Equation (2.14) is the full form of CLT that describes how a laminate reacts to applied loading. Note that the form does not relate stress and strain, but rather

reaction forces and moments to mid-plane strains and curvatures via a stiffness matrix, the inverse of the compliance matrix. For a general loading state, a composite laminate made up of unidirectional composite laminae must be treated as a structure and not a material; this means that attempting to derive an effective set of stiffness properties from CLT will inherently ignore the coupling between bending and extension (denoted as \mathbf{B}). However, this issue is not present when a laminate is symmetric about the mid-plane and is only subject to extensional loading [6].

2.3 Analytic Methods for Woven Composite Analysis

The analysis of woven laminated composites is complicated beyond that of a unidirectional laminae by the woven architecture of the lamina. The strands weave and undulate, and thus the material properties will be functions of internal variations and rotations of the strands. Further, as the lamina is deformed, the strands will straighten, causing the lamina to be stiffer. Therefore, improved models have been proposed that are better suited for woven composite laminae.

Outside of experimental methods, two broad categories exist by which estimations of the material properties of woven fabric composites can be obtained. Analytic methods use closed-form equations based on the geometry of the representative volume element (RVE) of the composite and the material properties of the constituent fiber and matrix to calculate the overall properties of the composite. Numerical methods, specifically the finite element method, numerically approximates the solution of the structural mechanics partial differential equation for the modeled RVE with the constituent material properties as inputs.

This section will focus on the development of analytic methods for woven composites, whereas the next section will cover finite element methods. The mesomechanical models presented here is not an exhaustive collection or discussion, and

only select highlights are presented. For a more complete discussion, see Crookston *et al.* [26], Dixit and Mali [27], and ElAgamy and Laliberté [16].

Analytic models are often computationally faster than numerical solutions of the governing partial differential equations (see e.g., [28]). The ability to quickly compute the properties from an analytic model means the results can be retrieved rapidly; this can be useful when computing damage progression in a more robust finite element model (see e.g., [29]). Further, because the analytic methods are generally a set of closed-form expressions, they provide easier analysis for when the effect of a certain set of design parameters are being studied. Optimization of these design parameters are also simplified because of the closed-form nature (see e.g., [30]).

For the general governing set of partial differential equations for stress and strain, there does not exist a closed form solution, thus there are often a set of assumptions made about either the geometry or the stress and strain field within the geometry (see e.g., [26]). These assumptions can either reduce the accuracy of the analytic methods or create a computationally prohibitive and complicated analysis of the expressions.

Ishikawa and Chou [18,31–34] are often credited with being the first to use a specialized model to predict the mechanical properties of woven composites. They developed three models for one-dimensional mechanical property analysis of satin weave laminae: the mosaic model, the fiber undulation model, and the bridging model. The mosaic model [18,31] idealizes the woven pattern as an assembly of asymmetric cross-ply laminae; in other words, the RVE is treated as a unidirectional stack of a fill strand and a warp strand, with the stacks swapped where the strand crosses over the opposing strand. The model was analyzed with both non-hybrid [31] and hybrid [18] weaves. The fiber undulation model [32,33] includes a set of sinusoidal functions to

better represent the undulation of the fibers passing over one another. The bridging model [32] uses the fiber undulation model surrounded by unidirectional ply stacks representing the fill and warp strands; this model was created to represent the gap between fiber crossover regions. All models use a form of classical laminate theory (CLT) to compute upper and lower bounds of the stiffness properties of the laminae. These models were experimentally validated in [34].

Raju and Wang [35] later expanded the mosaic model for three-dimensional analysis of thermomechanical properties, removing some of the original assumptions made by Ishikawa and Chou. The overall stiffness results are similar to that of Ishikawa and Chou, but the authors noted that the coefficient of thermal expansion analyses were unsatisfactory.

Naik *et al.* [36,37] also expanded upon the methods for predicting the effective lamina stiffness tensor of Ishikawa and Chou for two dimensions by accounting for the strand thickness transverse to the loading direction. In [36], Naik and Shembekar present a series-parallel (SP) model and a parallel-series model (PS), using an infinitesimal CLT approach similar to the methods presented by Ishikawa and Chou, which is then simplified in [37].

With an assumed geometry, CLT can be performed at each infinitesimal slice to obtain a stiffness or compliance matrix at each (x, y) location. The equations that define the $\mathbf{A}(x, y)$, $\mathbf{B}(x, y)$, and $\mathbf{D}(x, y)$ matrices of Equations (2.15) – (2.17) are defined using the assumed geometric functions of the weave and the $\bar{\mathbf{Q}}$ matrices of the warp, fill, and matrix (see [36] for these formulae). Note now that the force and moment values of Equation (2.14) are now spatially dependent; thus, the form of the infinitesimal CLT stiffness matrix becomes [36]

$$\begin{bmatrix} \mathbf{N}(x, y) \\ \mathbf{M}(x, y) \end{bmatrix} = \begin{bmatrix} \mathbf{A}(x, y) & \mathbf{B}(x, y) \\ \mathbf{B}(x, y) & \mathbf{D}(x, y) \end{bmatrix} \begin{bmatrix} \boldsymbol{\varepsilon}^\circ(x, y) \\ \boldsymbol{\kappa}(x, y) \end{bmatrix} \quad (2.18)$$

which can be inverted to obtain the compliance matrix as

$$\begin{bmatrix} \boldsymbol{\varepsilon}^\circ(x, y) \\ \boldsymbol{\kappa}(x, y) \end{bmatrix} = \begin{bmatrix} \mathbf{a}(x, y) & \mathbf{b}(x, y) \\ \mathbf{b}(x, y) & \mathbf{d}(x, y) \end{bmatrix} \begin{bmatrix} \mathbf{N}(x, y) \\ \mathbf{M}(x, y) \end{bmatrix} \quad (2.19)$$

Note that \mathbf{a} , \mathbf{b} , and \mathbf{d} are not the inverses of \mathbf{A} , \mathbf{B} , and \mathbf{D} . The infinitesimal stiffness or compliance matrices can be averaged over the domain to obtain an effective stiffness or compliance matrix. From this process, SP and PS models can be determined. The SP model first averages the compliance matrices given in Equation (2.19) in the direction of the load (assumed to be in the x -direction, or along the fill strand) as [36]

$$\bar{a}_{ij}^s(y) = \frac{1}{L_w} \int_0^{L_w} a_{ij}(x, y) dx \quad (2.20)$$

$$\bar{b}_{ij}^s(y) = \frac{1}{L_w} \int_0^{L_w} b_{ij}(x, y) dx \quad (2.21)$$

$$\bar{d}_{ij}^s(y) = \frac{1}{L_w} \int_0^{L_w} d_{ij}(x, y) dx \quad (2.22)$$

where L_w is the length of the RVE in the warp direction and $i, j \in \{1, 2, 3\}$. The compliance matrices $\bar{a}_{ij}^s(y)$, $\bar{b}_{ij}^s(y)$, $\bar{d}_{ij}^s(y)$ are put into the concatenated matrix form in Equation (2.19), which is then inverted to obtain the stiffness matrices $\bar{A}_{ij}^s(y)$, $\bar{B}_{ij}^s(y)$, $\bar{D}_{ij}^s(y)$. With an iso-strain condition, these stiffness matrices are averaged transverse to the loading direction as [36]

$$\bar{A}_{ij}^{sp} = \frac{1}{L_f} \int_0^{L_f} \bar{A}_{ij}^s(y) dy \quad (2.23)$$

$$\bar{B}_{ij}^{sp} = \frac{1}{L_f} \int_0^{L_f} \bar{B}_{ij}^s(y) dy \quad (2.24)$$

$$\bar{D}_{ij}^{sp} = \frac{1}{L_f} \int_0^{L_f} \bar{D}_{ij}^s(y) dy \quad (2.25)$$

where L_f is the length of the RVE in the fill direction and $i, j \in \{1, 2, 3\}$. The results of this analysis provides the formulation for the SP model. A similar formulation is presented for the PS model, starting instead with averaging the infinitesimal stiffnesses in Equation (2.18) along y , inverting to obtain the compliances, then averaging

again along x assuming an iso-stress condition. The SP model provides lower bounds for the stiffness and upper bounds for the compliance, and the PS model provides upper bounds for the stiffness and lower bounds for the compliance.

Scida *et al.* [3, 13] expanded the work of Naik and colleagues. They developed a model termed MESOTEX (MEchanical Simulation Of TEXTiles) based on the methods of Naik and Shembekar [36]. The main improvement is that, in [13], Scida *et al.* provide analytic forms of approximate geometric functions for both satin and twill weave composite laminae. Further, in [3], they expand the analysis for three-dimensional properties and compare the analytic results to experimental results, with good agreement to experimental results available for select components of the stiffness moduli. This particular model is used as a means of comparison for the twill and satin weave laminae in Chapter Five when no finite element model is available; this is chosen in part because of the amount of experiment results available for comparison for different systems.

A subset of analytic models are cell models (see e.g., [28, 29, 38]). These models, based upon a method introduced by Aboudi [39], use multiple homogenization steps to combine easily analyzed “cells” into one system. These methods are a compromise between the fast but low accuracy analytic models and the highly accurate but slow finite element models [28]. Further, more complicated analyses can be made as there is no need to generate one closed-form solution for the entire RVE.

One of the more prominent cell models in literature is one presented by Vardeurzen *et al.* [38, 40, 41]. In [38], they build a library of 108 possible subcells from which virtually any lamina could be built from. These subcells are then homogenized together and material properties predicted [40]. This method can also be used to calculate local stresses and strains [41]; after the cells are homogenized, a

stress state is applied and the cells are broken back down to determine local stresses and strains.

Despite the increased use of finite element methods in analysis of woven composite laminae, analytic methods are still being developed and analyzed for various purposes. Lua [29] developed a cell model that can determine the thermomechanical properties of a composite lamina at a given state of damage. This type of analytic method can be used in tandem with a finite element model to recalculate the material properties of the composite as damage propagates through the part. Zuo and Xie [30] used the effective property functions from Liu *et al.* [42] to optimize the effective stiffness of composite laminae based on several design parameters. The functions presented in Liu *et al.* [42] are unique in their own right. The functions developed disprove the idea that the Voigt estimate of material properties (i.e., rule of mixtures) is the upper bound of stiffness; the model presented by Liu accounts for Poisson effect, which alters the bounds of stiffness in a composite.

2.4 Finite Element Methods for Woven Composite Analysis

Another means of predicting the material properties of a woven composite lamina is to use a numerical method, specifically the finite element method. Finite element analysis (FEA) is a numerical method that recasts a partial differential equation as a set of linear equations which can be solved through matrix manipulation. Chapter Three provides an in-depth look into the formulation of the structural mechanics finite element problem; here, a discussion of the merits of the method itself as applied to woven composites as well as some previously developed finite element methods are presented. The finite element method has as its prime advantage that it yields solution accuracy of the internal stress and strain state that is only limited by the machine precision of the computer.

One major advantage that FEA has over analytic methods is that there are few assumptions about stress and strain field. The derivation of the structural mechanics finite element problem starts from basic continuum principles; numerical approximations are made only within the displacement field of a single element. Because the problem is solved numerically, there is no need to make assumptions about how the geometry affects the resulting mechanical response because there is no closed-form analytic form that needs to be derived. A derivation of the three-dimensional structural mechanics problem is presented in Chapter Three.

A major disadvantage, especially in woven composite lamina analysis, is meshing the geometry. Traditionally, a single finite element contains has smooth and continuous functions for the material behavior, so the mesh must conform to material boundaries. Due to the complex internal geometry of woven composite RVEs, however, the mesh can become very difficult and time-consuming to generate, as well as computationally expensive to solve. As computational resources are limited for these analyses, some researchers seek ways to work around these issues.

2.4.1 Geometry Generation

Because the mesh is a direct function of the geometry, it is natural to assume a form of the geometry that is more easily meshed than a more realistic model. Early on, authors such as Thom [43] and Chapman and Whitcomb [44] would have to investigate what assumptions about the geometry had the least affect in the accuracy of the model. As computers continued to improve, assumptions on the geometry were replaced with analytic models that worked in tandem with finite element software (see e.g., [29, 45]). These homogenization models were best suited for progressive damage models, where the material properties of the composite could be homogenized through an analytic model, sent to the finite element code to calculate the next step of the

crack propagation, then the new parameters would be returned to the analytic model, etc.

Recently, some authors (see e.g., [46]) have been relying heavily on specialized software packages to generate woven composite RVEs, such as WiseTex [47] or TexGen [7, 48]. These packages automatically generate meshes of more complex and more realistic RVEs for woven, three dimensional, and braided composites than analytic functions can easily provide.

To obtain the most realistic geometries for analysis, a physical composite structure can be digitally scanned to generate a two dimensional image or three dimensional model. For example, Stair *et al.* [8] demonstrated a method for using ultrasound to scan woven composites for the internal fiber architecture and orientation. Goris and Osswald [9] used micro CT scans on short fiber filled composites to determine fiber orientation within the composite. Middleton [10] also used micro CT scans of long fiber composites to determine the stiffness properties using FEA. These physical methods do not directly generate the geometry, but produce a pointwise description of material behavior, which is not easily mapped over to tradition finite elements.

2.4.2 Alterations to the Finite Element Methods

Because it is desirable to analyze the most realistic geometry possible for the most accurate results, alterations to the geometric model are undesirable. Another option to simplifying the analysis of complex geometries is to alter the traditional finite element process. Some unique methods have been developed over time to overcome the difficulties in analyzing complex internal geometries; some of those methods will be presented here.

Whitcomb and Woo [49–51] presented a number of methods to develop what are termed “macroelements”. The macroelements were developed by using a preex-

isting mesh for an RVE and relating unwanted degrees of freedom to the macroelement degrees of freedom; these macroelements would then be used as building blocks to build more complex composite structures.

In Woo and Whitcomb [49], a method termed “subdomain integration” is derived by adding another Jacobian transformation to the calculation. Essentially, a deformed element containing multiple materials would be related to a master element by the Jacobian matrix, then the multiple materials within this master element would be related to their own master elements through another application of the Jacobian matrix. This formulation was simplified in [50], where the unwanted degrees of freedom were instead directly related to the macroelement degrees of freedom via the interpolation functions. A “multi-field” approach to macroelements is presented in [51]; the interior boundary degrees of freedom are related to the boundary degrees of freedom for the macroelement using static condensation. After the application of static condensation, the boundary degrees of freedom are related to the macroelement degrees of freedom using a method based on the work performed by the boundary nodes.

Both the subdomain integration method and the multi-field method were evaluated against a homogenized approach by Maxwell and Whitcomb [52]. It was determined that both methods performed better overall as compared to the homogenized method. The subdomain integration method provided shorter solution times, but the multi-field approach provided marginally better results.

Cox *et al.* [53,54] presented a binary model for three-dimensional textile composites. The formulation of the element consists of modeling the axial properties of each yarn as two-noded line elements, whereas the remaining properties of the yarn

and surrounding matrix (deemed the “effective medium”) is modeled as a solid three-dimensional element [53]. When compared to experimental results, the binary model showed some improvement over orientation averaging methods [54].

Chen *et al.* [55] presented a method similar to that of Whitcomb and Woo [50] for applications in three-dimensional braided composites. The method consists of separately analyzing three regions of the braided composite: the interior, the surface, and the corner. The material properties of these regions are determined using a fine mesh. The entire composite is then analyzed using the properties of these smaller regions using a much coarser mesh. The resulting analysis provided good results as compared to experimental results, but experimental results were only available for E_{11} , ν_{12} , and ν_{13} , thus limiting the validated terms.

Wang and Sun [56] presented a novel means of modeling yarn architecture using what the authors termed as the “digital element”. The yarn is modeled as a one-dimensional linkage of cylindrical rods and frictionless pins, where the rods maintain the tensile properties of the rod and the pins maintain the flexibility. When two yarns are in contact, the frictional force between them can be calculated to determine if the yarns stick or slip. This method of simplifying the model down to a one-dimensional model simplifies the calculation of the stiffness matrix, although a perturbation has to be included to prevent singularities in the solution.

Nakai *et al.* [57] presented a superposition method whereby the local mesh of the strands are superimposed upon the global mesh of the matrix. In other words, the mesh is created for the matrix alone, and then the mesh for the strands are placed on top of this mesh. The full stiffness matrix \mathbf{K} is composed of three submatrices: one for the global RVE \mathbf{K}^G , one for the local strands \mathbf{K}^L , and a global/local correlation submatrix \mathbf{K}^{GL} . This method was first tested on a unidirectional fiber and

matrix micromechanics model to measure the effects of volume fraction on material properties. As compared to a traditional finite element model, the proposed method showed excellent agreement. The method was then used to predict the stiffness and strength of a plain weave composite lamina; as compared to the traditional finite element model, the superposition model showed good agreement.

Iarve *et al.* [58], similar to Nakai *et al.* [57], also proposed that the yarn and matrix should be meshed separately. In a method proposed by Iarve, the yarns are meshed first as usual, but then the entire domain of the RVE is meshed using cuboid elements as if the yarns were not present. Using a penalty factor, the effect of the elements occupying the same space as the yarn elements are removed; the remaining elements are used to represent the matrix. A method to refine the elements around the material boundary is also presented. A comparison of this model was made to experimental results, showing good match of results.

Gager and Pettermann [59] proposed the use of shell elements instead of solid elements to model woven geometries. Shell elements are two-dimensional elements that exist in three-dimensions. The idea behind this was to reduce the number of degrees of freedom required to solve by modeling the fiber and resin as two-dimensional geometries instead of three-dimensional ones. The stress-strain curve from an analysis of a twill weave composite showed excellent agreement with a traditionally meshed RVE.

2.4.3 Voxel Methods

Another trick to work around geometric complexities is to use a mesh of simple cuboid elements, termed “voxels”, that do not fully conform to the material boundaries; rather, as the mesh becomes more refined, the mesh itself converges to

the material boundaries. This type of method has become collectively referred to as “voxel methods.”

In the present context, this approach was first suggested in 2003 by Kim and Swan [14] for applications in textile composites. In the method they proposed, when a voxel contains a material boundary, the element is homogenized based on the volume fraction of the materials contained within the element. A rule of mixtures approach was proposed in [14] to generate an upper bound on material properties, whereas an inverse rule of mixtures approach was used generate a lower bound on material properties. In addition to this homogenization scheme, the authors also detailed a means of refining the mesh around material boundaries through the use of nonconforming elements; that is, elements that had nodes on the edges of other elements. Similar to Whitcomb and Woo [50], these nodes could be slaved to the master edge. When compared to a traditional mesh, both the upper and lower bound converged to the results obtained from the traditional mesh. Although there was an increase in computational cost, the authors in [14] argue that this is offset by a reduction in the time required to mesh the geometry.

An identical method was proposed by Watanabe *et al.* [15] for applications in electromagnetism. The voxel elements sitting upon a rounded boundary could be homogenized based on the permeability of the two materials contained; rule of mixtures was used to determine the tangential component and inverse rule of mixtures was used to determine the normal component. Results as compared to a traditional voxel method showed a faster convergence in inductance for the homogenized voxel elements. Sato *et al.* [60] extended upon the voxel element strategy with a method for refining the voxels around material boundaries, similar to Kim and Swan [14].

The results showed an improved calculation of all results except for magnetic force as the homogenization affected the distribution of the magnetic flux density.

Smitheman *et al.* [61] presented a two-level numerical homogenization scheme to determine the thermomechanical properties a woven composite. The RVE is first divided into cuboids, and each cuboid is divided into subcuboids. Within each subcuboid, the material at the centroid is determined; if the centroid is within resin, the properties of the entire subcuboid are assumed to be that of the resin. If the centroid lands in a yarn, the subcuboid is sampled at a number of equally distributed points to estimate the volume fraction of the subcuboid, which is then used in a micromechanics model to estimate the thermomechanical properties of the subcuboid. Once the properties are known in each subcuboid, the thermomechanical properties of the cuboid are estimated to be the average of each of the subcuboids properties. On the carbon/epoxy plain weave composite tested in [61], the proposed method predicted the planar tensile modulus and Poissons ratio within 1% accuracy of experimental results. However, all other properties were predicted poorly (over 6% error), especially the planar shear moduli, predicting a property with over 20% error as compared to experimental data.

The biggest downside of voxel-based methods is that a very fine mesh is still necessary to obtain the necessary resolution needed for accuracy. In addition, the sharp edges of the voxel elements can cause stress stress concentrations, thus limiting their use in damage modeling. In 2015, Doitrand *et al.* [62] compared a traditional finite element mesh with a voxel mesh in the application of material property prediction and damage prediction of a meso-scale model of a woven fabric composite. It was determined that, while voxel elements performed well for homogenization studies at finer resolutions, due to the local stress concentrations and oscillations at the

sharp edges of the voxel elements, damage prediction was poor. While a smoothing method could be applied (such as the stress-averaging technique proposed by Fang *et al.* [63]), this also removes stress concentrations that agree with the traditional model. The authors in [62] urge caution with the application of voxel methods where studying the local stress concentrations are required.

The resolution of an individual element can be increased by considering the points used by the numerical integration scheme to calculate the elemental stiffness matrix. Lippmann *et al.* [11] proposed a three dimensional multiphase element where material properties are applied at the Gaussian integration points as a means to increase resolution. The application sought was for easier analysis of metallic composites. An identical method was proposed by Zeng *et al.* [12,64] for applications in the mechanical analysis of three-dimensional braided composites. In [12], the authors test the method for mechanical properties against the braid angle of the composite; compared against experimental results from literature, the method showed reasonable accuracy for planar tensile modulus while showing exceptional accuracy for out-of-plane tensile modulus. No comparisons were made for the shear moduli or Poisson's ratios. In [64], the authors used the element to reproduce the nonlinear stress-strain curve of a braided composite, taking failure into account. Again, the multiphase element presented showed reasonable accuracy compared to experiment.

Caselman, in his thesis [1], sought to improve upon the accuracy of the finite element proposed by Zeng *et al.* [12] for applications in RVE analysis of short fiber composites. He proposed that the accuracy within the element was affected because of the change in the strain field that occurred across the discontinuous material boundary; therefore, it was hypothesized that simply using the material found at each integration point was not enough for sufficient accuracy. Using the analogy

of a one-dimensional spring model, Caselman derived a set of strain correction factors that could be applied at each integration point. For a simple one-dimensional system, these corrections provided an exact result as compared to a traditional finite element model. For a simple three-dimensional system, the trends were noted to be nearly exact except for the calculation of the transverse shear modulus G_{23} . Using the UEL function in ABAQUS, a custom element was made and applied to the single fiber models of Tucker and Liang [21] and Xia [25], providing results in good agreement with these previous models. The element was then used to analyze an RVE of randomly oriented short fibers in matrix. This element was also used by Middleton [10] for the analysis of micro CT data of a long fiber composite, to good accuracy. A summary of the findings in both Caselman’s thesis [1] and Middleton’s thesis [10] can be found in Smith [65].

The elements proposed by Kim and Swan [14], Zeng *et al.* [12], and Caselman [1] are discussed in further detail in Chapter Four.

2.5 The Extended Finite Element Method

Here, a brief overview of the extended finite element method (XFEM) will be given, but a more in-depth review of the theory and applications will be given in Chapter Six as a part of discerning the future work of the presented research. While the XFEM method is not directly applied in this research, the ideas presented in this thesis can in theory reasonably be applied in conjunction with XFEM to potentially construct a more accurate multiphase voxel element (MVE).

The extended finite element method (XFEM) is an extension upon standard finite element methods that utilize “enrichment functions” that allow for greater resolution within the element. This allows discontinuities, such as cracks or material boundaries, to exist within an element without the addition of more nodes; rather,

the nodes are enriched through the addition of extra degrees of freedom. Therefore, XFEM can be reasonably extended to applications in material property predicting of woven composite laminae. A methodical summary of the XFEM process can be found in Fries and Belytschko [66]; a summary of XFEM as it applies to material studies can be found in Huynh and Belytschko [67] and Belytschko *et al.* [68].

The mathematical basis for the XFEM process is the partition of unity method, first proposed by Melenk and Babuška [69]; they propose a mathematical means for including local phenomena within the finite element space. Belytschko and Black [70] used this parity of unity method to develop a means of studying elastic crack growth within a finite element model without discretely modeling the crack itself.

The basic premise is that the displacement within an element field is estimated as (see e.g., [66, 68])

$$\mathbf{u}(\mathbf{x}) = \underbrace{\sum_{i \in I} u_i \psi_i(\mathbf{x})}_{\mathbf{u}^{\text{FE}}} + \underbrace{\sum_{i \in I} q_i \psi_i(\mathbf{x}) \Phi(\mathbf{x})}_{\mathbf{u}^{\text{enr}}} \quad \forall \mathbf{x} \in \Omega \quad (2.26)$$

The first part of this equation, labeled \mathbf{u}^{FE} , is the standard approximation of the displacement field used in finite elements, where u_i refers to the i^{th} nodal displacement in the domain of the geometry Ω , and $\psi_i(\mathbf{x})$ is the corresponding interpolation function. This form will be discussed in more detail in Chapter Three, where the standard finite element methods are presented.

The second part of Equation (2.26), \mathbf{u}^{enr} , refers to the displacement caused by the enrichment function $\Phi(\mathbf{x})$. This enrichment function describes a local phenomenon that is occurring within the domain of an element. An example of this enrichment function for crack propagation (an example of a strong discontinuity) is provided Belytschko *et al.* [68]; Moës *et al.* [71] developed an enrichment function that is used to describe a material boundary (an example of a weak discontinuity).

To determine the efficiency of XFEM as compared to current methods, Lian *et al.* [72] directly compared XFEM to a voxel-based method. The models selected to perform the comparison include a two-dimensional randomly generated composite with circular inclusions, a two dimensional ceramic-metallic composite from a digital image, and a three dimensional foam material generated from a scan. It was determined that, while XFEM had a higher computational cost due to the added degrees of freedom, the method converged faster than the voxel-based methods and is therefore overall more numerically efficient.

A concern with using the enrichment functions is the numerical integration [73]. As will be discussed further in Chapter Three, the calculation of the stiffness matrices require numerical integration, which is traditionally done through the use of Gauss quadrature. In XFEM, the solution space is enriched with singular or discontinuous functions; the numerical integration of these functions are inaccurate when using standard Gauss quadrature. An alternate scheme is required, such as an adaptive scheme or a subdomain quadrature; see [73] for a full list of suggestions. Yazdani *et al.* [74] performed studies on some traditional numerical integration techniques (Gauss quadrature, Newton-Cotes, and Lobatto quadrature) to determine the accuracy of each technique. They determined that Lobatto quadrature performed best overall, but many attempts to obtain a converged solution resulted in oscillations in the solution curve. Because the method of MVEs relies on application of material properties at integration points in Gauss quadrature, then this could pose a problem when combining an MVE-like approach with XFEM.

CHAPTER THREE

The Finite Element Method

In this chapter, a list of methods for use in finite elements and their derivations will be presented and discussed. The purpose of this discussion is to provide a theoretical background on tools that were used in this research.

Note that in the equations contained in the following sections, vectors will be represented as bold letters (e.g., \mathbf{a}), whereas scalars and tensor/matrix components will be represented with italics (e.g., a or a_i). Further, unless otherwise noted, Einstein summation convention will be used in order to reduce the complexity of the written equations. This convention says that repeated indices imply summation from 1 to 3; for example, $a_{ii} = a_{11} + a_{22} + a_{33}$, and $a_i b_i = a_1 b_1 + a_2 b_2 + a_3 b_3$. Under this convention, partial derivatives with respect to the global coordinates x_j are represented with a comma, so the partial derivative of a_i with respect to x_j is represented as $a_{i,j}$. Derivatives with respect to the local coordinates ξ_χ will be represented with the Greek letter χ , so the derivative of a_i with respect to ξ_χ is represented as $a_{i,\chi}$.

3.1 The Finite Element Equations for Structural Mechanics

This section will focus on deriving the constituent finite element equations used in the structural analysis of a three-dimensional geometry. The derivation following will start from first principles found in continuum mechanics and then derive the approximation of the weak form following the Petrov–Galerkin formulation.

3.1.1 Continuum Mechanics First Principles

In order to derive the finite element form of the structural mechanics problem, three relations are needed. The first equation, the strain–displacement relationship,

relates the six strain states ε_{ij} to the displacement u_i as (see e.g., [5])

$$\varepsilon_{ij} = \frac{1}{2} (u_{i,j} + u_{j,i}) \quad (3.1)$$

Note that this linear relationship assumes small strains. The second relationship required are the three local equations of motion. These equations state that the sum of the derivative of the six stresses σ_{ij} plus internal body forces per unit volume f_i at every material point is equivalent to the density ρ times the acceleration \ddot{u}_i of the local point. Moving all the terms to the left-hand side, the local equations of motion are expressed mathematically as (see e.g., [5])

$$-\sigma_{ij,j} - f_i + \rho\ddot{u}_i = 0 \quad (3.2)$$

The numbering scheme for both the stress tensor σ_{ij} and the strain tensor ε_{ij} is presented in Figure 3.1; the two schemes are identical.

The final equation is referred to as generalized Hooke's law, expressed as (see e.g., [5])

$$\sigma_{ij} = C_{ijkl}\varepsilon_{kl} \quad (3.3)$$

This equation relates the stress σ_{ij} on a body to the strain ε_{kl} through C_{ijkl} , which is the fourth-order stiffness tensor and is an intrinsic property of the material. The tensor C_{ijkl} may be shown to contain symmetry through work-energy and Hooke's Law (see e.g., [6]), meaning some terms with interchanged indicies are equivalent to each other. Therefore, while C_{ijkl} has 81 terms in total, there are only 21 independent terms [6]. The equivalent terms are

$$C_{ijkl} = C_{jikl} = C_{ijlk} = C_{jilk} = C_{klij} = C_{klji} = C_{lki j} = C_{lkji} \quad (3.4)$$

The property will be useful in the derivation of the finite element form as it will help simplify formulae with redundant terms.

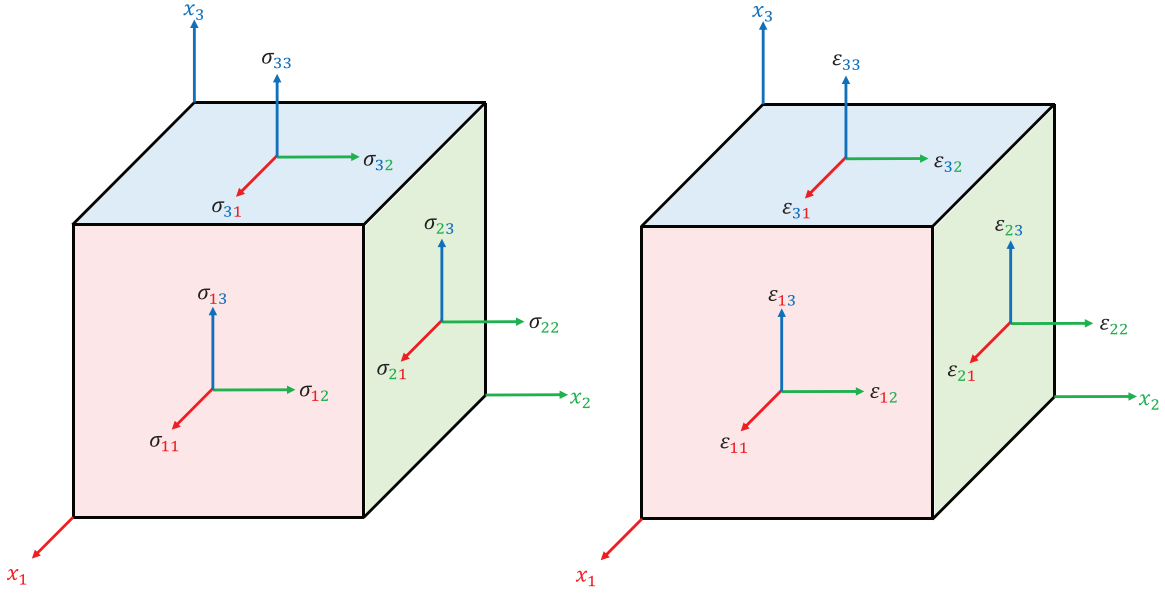


Figure 3.1: The numbering scheme for the stress tensor σ_{ij} (left) and for the strain tensor ϵ_{ij} (right). The schemes used are identical.

3.1.2 Development of the Weak Form

The first step in deriving the finite element equations in the Petrov–Galerkin formulation is to develop the weak form of the differential equation over a general body, represented in Figure 3.2. The domain of the general body is labeled Ω , the surface of the body is labeled Γ , and the surface normal vector is labeled $\hat{\mathbf{n}}$. The derivation of this form will follow a similar to one commonly presented in finite element textbooks (see e.g., [75]). To start, Equation (3.2) is multiplied by an arbitrary continuous and sufficiently differentiable weight function $w = w(\mathbf{x})$ and integrated over the domain as

$$\int_{\Omega} w (\sigma_{ij,j} - f_i + \rho \ddot{u}_i) \, d\Omega = 0 \quad (3.5)$$

The weight function is distributed to the terms in the parentheses, and the integral is split as

$$-\int_{\Omega} w \sigma_{ij,j} \, d\Omega - \int_{\Omega} w f_i \, d\Omega + \int_{\Omega} w \rho \ddot{u}_i \, d\Omega = 0 \quad (3.6)$$

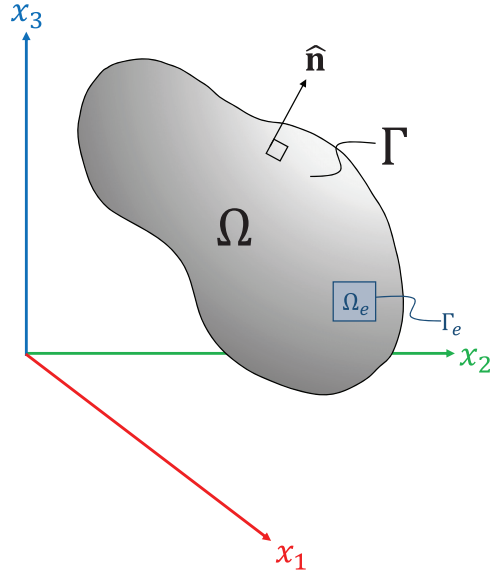


Figure 3.2: A general domain Ω with surface Γ and surface normal $\hat{\mathbf{n}}$. An element with domain Ω_e and surface Γ_e is also depicted.

From Equation (3.3), the stress is a function of strain, which from Equation (3.1) is in turn a function of gradients of the displacement u_i . Thus in Equation (3.6), the derivative of stress can be thought of as being a function of the second derivatives of displacement. To reduce the order of the derivative on σ_{ij} — thereby reducing the order of differentiation on u_i — divergence theorem can be invoked, resulting in an integral around the closed surface of the domain Γ . Thus the first term in Equation (3.6) is recast as

$$-\int_{\Omega} w \sigma_{ij,j} d\Omega = \int_{\Omega} w_{,j} \sigma_{ij} d\Omega - \oint_{\Gamma} w n_j \sigma_{ij} d\Gamma \quad (3.7)$$

where n_i is the i^{th} component of the surface normal vector $\hat{\mathbf{n}}$. With the above equation, Equation (3.6) is expressed as

$$\int_{\Omega} w_{,j} \sigma_{ij} d\Omega + \int_{\Omega} w \rho \ddot{u}_i d\Omega = \int_{\Omega} w f_i d\Omega + \oint_{\Gamma} w n_j \sigma_{ij} d\Gamma \quad (3.8)$$

an expression termed the weak form in terms of the stress σ_{ij} .

To recast Equation (3.8) in terms of the displacement u_i , Equations (3.1) and (3.3) can be substituted into the first term of Equation (3.8) as

$$\int_{\Omega} w_{,j} \sigma_{ij} \, d\Omega = \int_{\Omega} w_{,j} C_{ijkl} \varepsilon_{kl} \, d\Omega = \int_{\Omega} \frac{1}{2} w_{,j} C_{ijkl} (u_{k,l} + u_{l,k}) \, d\Omega \quad (3.9)$$

As described in Equation (3.4), the tensor C_{ijkl} is a symmetric tensor. Further, as the indicies k and l are repeated, they are arbitrary. These properties can be invoked here to simplify Equation (3.9) as

$$\begin{aligned} \int_{\Omega} \frac{1}{2} w_{,j} (C_{ijkl} u_{k,l} + C_{ijlk} u_{l,k}) \, d\Omega &= \int_{\Omega} \frac{1}{2} w_{,j} (C_{ijkl} u_{k,l} + C_{ijlk} u_{k,l}) \, d\Omega \\ &= \int_{\Omega} \frac{1}{2} w_{,j} (C_{ijkl} u_{k,l} + C_{ijlk} u_{k,l}) \, d\Omega \\ &= \int_{\Omega} w_{,j} C_{ijkl} u_{k,l} \, d\Omega \end{aligned} \quad (3.10)$$

This reduces Equation (3.8) to the weak form in terms of the displacements and boundary stress.

$$\int_{\Omega} w_{,j} C_{ijkl} u_{k,l} \, d\Omega + \int_{\Omega} w \rho \ddot{u}_i \, d\Omega = \int_{\Omega} w f_i \, d\Omega + \oint_{\Gamma} w n_j \sigma_{ij} \, d\Gamma \quad (3.11)$$

3.1.3 Approximating the Solution

The domain Ω is next discretized into smaller subdomains called “elements”, each with domain Ω_e and closed boundary Γ_e , as shown in Figure 3.2. Each element is defined by N nodes, where the node $n \in \{1, 2, \dots, N\}$ is globally located at \mathbf{x}^n and has a time-dependent displacement of $u_i^n(t)$. These nodes are used to estimate the displacement of the element.

The displacement field within the element is estimated by a set of N spatially-dependent interpolation functions $\psi^n(\mathbf{x})$. These interpolation functions have two conditions, referred to as the partition of unity, given as (see e.g, [75])

$$\psi^n(\mathbf{x}^j) = \begin{cases} 1 & \text{if } n = j \\ 0 & \text{if } n \neq j \end{cases} \quad (3.12)$$

$$\sum_{n=1}^N \psi^n(\mathbf{x}) \equiv 1 \quad \forall \mathbf{x} \in \Omega_e \quad (3.13)$$

Using the nodal displacements $u_i^n(t)$ and the interpolation functions $\psi^n(\mathbf{x})$, the displacement at a location $\mathbf{x} \in \Omega_e$ can be numerically estimated as

$$u_i(\mathbf{x}, t) = \sum_{n=1}^N u_i^n(t) \psi^n(\mathbf{x}) \quad (3.14)$$

For the present work, these interpolation functions will also serve as the arbitrary weight function. Substituting $w(\mathbf{x}) = \psi^m(\mathbf{x})$ and the approximation in Equation (3.14) into the weak form in Equation (3.11) for each element Ω_e yields

$$\int_{\Omega_e} \psi_{,j}^m C_{ijkl} \psi_{,l}^n d\Omega_e u_k^n + \int_{\Omega_e} \rho \psi^m \psi^n d\Omega_e \ddot{u}_i^n = \int_{\Omega_e} f_i \psi^m d\Omega_e + \oint_{\Gamma_e} n_j \sigma_{ij} \psi^m d\Gamma_e \quad (3.15)$$

where $i, j, k, l \in \{1, 2, 3\}$ and $m, n \in \{1, 2, \dots, N\}$, where N is the number of nodes in the element. Notice in Equation (3.15), for each value of i , there are N equations, one for each value of n . Further, the free indicies are i and m .

3.1.4 From Index to Vector Notation

The index form of Equation (3.15), although correct, is cumbersome for some computational implementations; it would be much more convenient for the equation to be written in a matrix form so that matrix operations can be performed in lieu of a series of nested `for` loops. The matrix formulation will be presented first, and then equivalency between this matrix form and the index form in Equation (3.15) will be shown.

The matrix form of the three-dimensional structural mechanics problem is given as (see e.g., [75])

$$\int_{\Omega_e} \mathbf{B}^T \mathbf{C} \mathbf{B} d\Omega_e \mathbf{u}^e + \int_{\Omega_e} \rho \mathbf{\Psi}^T \mathbf{\Psi} d\Omega_e \ddot{\mathbf{u}}^e = \int_{\Omega_e} \mathbf{\Psi}^T \mathbf{f} d\Omega_e + \oint_{\Gamma_e} \mathbf{\Psi}^T (\boldsymbol{\sigma} \hat{\mathbf{n}}) d\Gamma_e \quad (3.16)$$

where \mathbf{u}^e is a $3N \times 1$ vector containing the elemental displacements, given as

$$\mathbf{u}^e = [u_1^1 \quad u_2^1 \quad u_3^1 \quad \cdots \quad u_1^N \quad u_2^N \quad u_3^N]^T \quad (3.17)$$

\mathbf{f} is a 3×1 vector containing the elemental body forces from Equation (3.2), given as

$$\mathbf{f} = [f_1 \quad f_2 \quad f_3]^\top \quad (3.18)$$

\mathbf{B} , termed the strain–displacement matrix, is a $6 \times 3N$ matrix given as

$$\mathbf{B}(x_1, x_2, x_3) = [\mathbf{B}_1 \mid \mathbf{B}_2 \mid \cdots \mid \mathbf{B}_N] \quad (3.19)$$

$$\mathbf{B}_m(x_1, x_2, x_3) = \begin{bmatrix} \psi_{,1}^m & 0 & 0 \\ 0 & \psi_{,2}^m & 0 \\ 0 & 0 & \psi_{,3}^m \\ 0 & \psi_{,3}^m & \psi_{,2}^m \\ \psi_{,3}^m & 0 & \psi_{,1}^m \\ \psi_{,2}^m & \psi_{,1}^m & 0 \end{bmatrix} \quad (3.20)$$

Ψ is a $3 \times 3N$ matrix representing the interpolation functions as

$$\Psi = \begin{bmatrix} \psi^1 & 0 & 0 & \psi^2 & 0 & 0 & \cdots & \psi^N & 0 & 0 \\ 0 & \psi^1 & 0 & 0 & \psi^2 & 0 & \cdots & 0 & \psi^N & 0 \\ 0 & 0 & \psi^1 & 0 & 0 & \psi^2 & \cdots & 0 & 0 & \psi^N \end{bmatrix} \quad (3.21)$$

and \mathbf{C} is the contracted form of the stiffness tensor, a symmetric 6×6 matrix representing only the 21 independent terms of the stiffness tensor C_{ijkl} , given as

$$\mathbf{C} = \begin{bmatrix} C_{1111} & C_{1122} & C_{1133} & C_{1123} & C_{1113} & C_{1112} \\ C_{1122} & C_{2222} & C_{2233} & C_{2223} & C_{2213} & C_{2212} \\ C_{1133} & C_{2233} & C_{3333} & C_{3323} & C_{3313} & C_{3312} \\ C_{1123} & C_{2223} & C_{3323} & C_{2323} & C_{2313} & C_{2312} \\ C_{1113} & C_{2213} & C_{3313} & C_{2313} & C_{1313} & C_{1312} \\ C_{1112} & C_{2212} & C_{3312} & C_{2312} & C_{1312} & C_{1212} \end{bmatrix} \quad (3.22)$$

For most of the terms in Equation (3.15), the transition from index to matrix form is trivial. This is not true for the first term on the left hand side, however, and a more involved proof must be demonstrated; this equivalency can be demonstrated by multiplying in the individual matrices one–at–a–time. Note that the symmetry on C_{ijkl} in Equation (3.4) will be invoked here. For the m^{th} interpolation function,

$$\mathbf{B}_m^T \mathbf{C} = \begin{bmatrix} \psi_{,j}^m C_{1j11} & \psi_{,j}^m C_{1j22} & \psi_{,j}^m C_{1j33} & \psi_{,j}^m C_{1j23} & \psi_{,j}^m C_{1j13} & \psi_{,j}^m C_{1j12} \\ \psi_{,j}^m C_{2j11} & \psi_{,j}^m C_{2j22} & \psi_{,j}^m C_{2j33} & \psi_{,j}^m C_{2j23} & \psi_{,j}^m C_{2j13} & \psi_{,j}^m C_{2j12} \\ \psi_{,j}^m C_{3j11} & \psi_{,j}^m C_{3j22} & \psi_{,j}^m C_{3j33} & \psi_{,j}^m C_{3j23} & \psi_{,j}^m C_{3j13} & \psi_{,j}^m C_{3j12} \end{bmatrix} \quad (3.23)$$

This expression is postmultiplied by \mathbf{B}_n to give the form

$$\mathbf{B}_m^T \mathbf{C} \mathbf{B}_n = \begin{bmatrix} \psi_{,j}^m C_{1j1l} \psi_{,l}^n & \psi_{,j}^m C_{1j2l} \psi_{,l}^n & \psi_{,j}^m C_{1j3l} \psi_{,l}^n \\ \psi_{,j}^m C_{2j1l} \psi_{,l}^n & \psi_{,j}^m C_{2j2l} \psi_{,l}^n & \psi_{,j}^m C_{2j3l} \psi_{,l}^n \\ \psi_{,j}^m C_{3j1l} \psi_{,l}^n & \psi_{,j}^m C_{3j2l} \psi_{,l}^n & \psi_{,j}^m C_{3j3l} \psi_{,l}^n \end{bmatrix} \quad (3.24)$$

The displacement vector in Equation (3.17) is postmultiplied into this result as

$$\mathbf{B}_m^T \mathbf{C} \mathbf{B}_n \mathbf{u}^n = \begin{bmatrix} \psi_{,j}^m C_{1jkl} \psi_{,l}^n u_k^n \\ \psi_{,j}^m C_{2jkl} \psi_{,l}^n u_k^n \\ \psi_{,j}^m C_{3jkl} \psi_{,l}^n u_k^n \end{bmatrix} \quad (3.25)$$

The form in equation (3.25) suggests that the i^{th} row of $\mathbf{B}_m^T \mathbf{C} \mathbf{B}_n \mathbf{u}$ can be evaluated as

$$(\mathbf{B}_m^T \mathbf{C} \mathbf{B}_n \mathbf{u}^n)_i = \psi_{,j}^m C_{ijkl} \psi_{,l}^n u_k^n \quad (3.26)$$

Thus the index form in Equation (3.15) and the matrix form in Equation (3.16) are equivalent.

Equation (3.16) is merely a set of linear algebra equations. The form becomes more obvious when the following relations are made:

$$\mathbf{K}^e = \int_{\Omega_e} \mathbf{B}^T \mathbf{C} \mathbf{B} \, d\Omega_e \quad (3.27)$$

$$\mathbf{M}^e = \int_{\Omega_e} \rho \mathbf{\Psi}^T \mathbf{\Psi} \, d\Omega_e \quad (3.28)$$

$$\mathbf{F}^e = \int_{\Omega_e} \mathbf{\Psi}^T \mathbf{f} \, d\Omega_e \quad (3.29)$$

$$\mathbf{Q}^e = \oint_{\Gamma_e} \mathbf{\Psi}^T (\boldsymbol{\sigma} \hat{\mathbf{n}}) \, d\Gamma_e \quad (3.30)$$

This leads to the final form of the finite element equations for one element with domain Ω_e .

$$\mathbf{K}^e \mathbf{u}^e + \mathbf{M}^e \ddot{\mathbf{u}}^e = \mathbf{F}^e + \mathbf{Q}^e \quad (3.31)$$

where \mathbf{K}^e and \mathbf{M}^e are $3N \times 3N$ matrices, and \mathbf{F}^e and \mathbf{Q}^e are $3N \times 1$ matrices. The final solution form of Equation (3.31) has recast the differential equations of (3.1)–(3.3) as a set of linear algebraic equations.

The matrix \mathbf{K}^e is commonly referred to as the “stiffness matrix” (not to be confused with Equation (3.22), the contracted form of the stiffness tensor \mathbf{C}) and relates local displacements in the system to a force required to cause that displacement. The matrix \mathbf{M}^e is referred to as the “mass matrix” and similarly relates local accelerations in the system to a force. The load vector \mathbf{F}^e refers to applied internal body forces within the system, and the reaction force vector \mathbf{Q}^e refers to the nodal reaction forces caused by the applied displacements, point loads, and surface tractions.

3.1.5 Assembling the Global System

Equation (3.31) is a linear algebraic system of equations that define one three-dimensional N -noded element with domain Ω_e . To approximate the differential equations in Equations (3.1) through (3.3) for the entire domain Ω as shown in Figure 3.2, a global system of equations can be assembled from the result of each of the elemental matrices in Equations (3.27) through (3.30). This is done by considering that a global node is a part of multiple elements and that the individual contribution from the stiffness matrix \mathbf{K}^e of each element is simply added together at that degree of freedom. Thus, this element connectivity can be used to combine the individual elemental matrices in Equations (3.27) through (3.30) into a final global system of the form (see e.g., [75])

$$\mathbf{K}\mathbf{u} + \mathbf{M}\ddot{\mathbf{u}} = \mathbf{F} + \mathbf{Q} \quad (3.32)$$

This system of equations is the system that is solved once the boundary conditions are applied, with all the unknown variables contained within the nodal displacement vector \mathbf{u} , the nodal acceleration vector $\ddot{\mathbf{u}}$, and the nodal reaction force vector \mathbf{Q} at each time step.

3.2 The Linear Hexahedral Element

With the finite element equations defined, a set of spatially dependent interpolation functions $\psi^n(\mathbf{x})$ must be selected for use in the strain displacement submatrix \mathbf{B}_m in Equation (3.20). These interpolation functions are defined by the shape of the element and the location of the nodes \mathbf{x}^j within the element, and the number of interpolation functions is equal to the number of nodes N . A constraint of the Petrov–Galerkin method is that the functions themselves equal one at the node it is associated with and zero at the other nodes, as described in Equation (3.12). Further, the sum of all N interpolation functions equal one at any given point $\mathbf{x} \in \Omega_e$, as described in Equation (3.13).

Because real–world geometries are complex, elements often have to be irregular in order to mesh the geometry accordingly. It would be cumbersome to have to define and derive a new set of interpolation functions in the global coordinate system defined by (x_1, x_2, x_3) for every irregular element with domain Ω_e in the system. To simplify this process, a simple “master element” with domain $\hat{\Omega}_e$ is defined, and then the irregular elements are mapped to this master element before calculating the element stiffness matrix in Equation (3.27). This master element is defined in its own local orthogonal coordinate system defined by (ξ_1, ξ_2, ξ_3) ; the local nodal locations $\boldsymbol{\xi}^j$ and the interpolation functions $\psi^n(\boldsymbol{\xi})$ are therefore defined in this local coordinate system. The Jacobian J_{ij} maps the irregular element in \mathbf{x} to the master element in $\boldsymbol{\xi}$.

3.2.1 The Master Element

In theory, any polyhedron can be selected to be a master element, but the tetrahedral element, triangular prism, and hexahedral element are commonly used. The interpolation functions for these elements are often simple polynomial expressions, i.e., linear, quadratic, cubic, etc. Computationally, however, the linear hexahedral

element is the simplest because the edges of the element align with the local orthogonal coordinate system $\boldsymbol{\xi}$. The master element for the linear hexahedral element is shown in Figure 3.3. The linear hexahedral master element is an 8-noded element in the shape of a cube centered at the origin of a local coordinate system defined by (ξ_1, ξ_2, ξ_3) and has side lengths of 2, as shown in Figure 3.3. That is to say, the local coordinates $\boldsymbol{\xi}^n = [\xi_1^n \quad \xi_2^n \quad \xi_3^n]$ at each node n is

$$\begin{pmatrix} \xi^1 \\ \xi^2 \\ \xi^3 \\ \xi^4 \\ \xi^5 \\ \xi^6 \\ \xi^7 \\ \xi^8 \end{pmatrix} = \begin{bmatrix} -1 & -1 & -1 \\ 1 & -1 & -1 \\ 1 & 1 & -1 \\ -1 & 1 & -1 \\ -1 & -1 & 1 \\ 1 & -1 & 1 \\ 1 & 1 & 1 \\ -1 & 1 & 1 \end{bmatrix} \quad (3.33)$$

The partition of unity, given in Equations (3.12) and (3.13), can be used with the nodal coordinates $\boldsymbol{\xi}^n$ to define a system of N equations to determine the N interpolation functions for the master element. The final result of this work for the 8-noded linear hexahedral element is a vector $\boldsymbol{\psi}(\xi_1, \xi_2, \xi_3)$ of eight interpolation functions, given as (see e.g., [75])

$$\boldsymbol{\psi}(\xi_1, \xi_2, \xi_3) = \begin{pmatrix} \psi^1 \\ \psi^2 \\ \psi^3 \\ \psi^4 \\ \psi^5 \\ \psi^6 \\ \psi^7 \\ \psi^8 \end{pmatrix} = \frac{1}{8} \begin{pmatrix} (1 - \xi_1)(1 - \xi_2)(1 - \xi_3) \\ (1 + \xi_1)(1 - \xi_2)(1 - \xi_3) \\ (1 + \xi_1)(1 + \xi_2)(1 - \xi_3) \\ (1 - \xi_1)(1 + \xi_2)(1 - \xi_3) \\ (1 - \xi_1)(1 - \xi_2)(1 + \xi_3) \\ (1 + \xi_1)(1 - \xi_2)(1 + \xi_3) \\ (1 + \xi_1)(1 + \xi_2)(1 + \xi_3) \\ (1 - \xi_1)(1 + \xi_2)(1 + \xi_3) \end{pmatrix} \quad (3.34)$$

3.2.2 The Jacobian

The master element serves as a mathematically convenient way to use the same set of equations to calculate the stiffness matrix \mathbf{K}^e for multiple unique 8-noded elements. In order to fully utilize the master element, the deformed element with

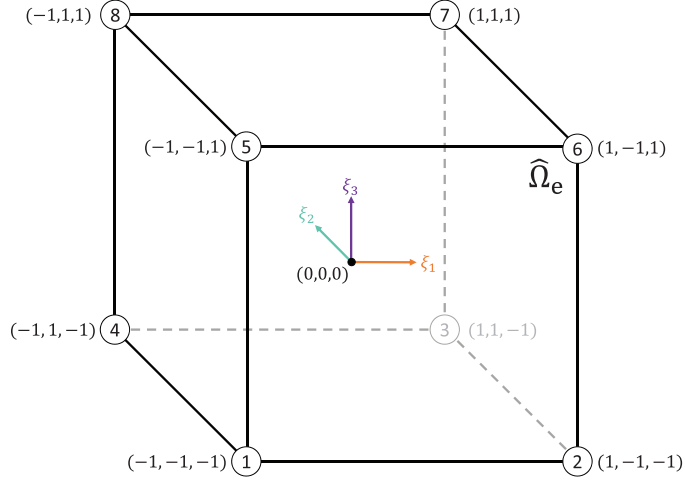


Figure 3.3: The master element with domain $\hat{\Omega}_e$ for a linear hexahedral element in the local coordinates (ξ_1, ξ_2, ξ_3)

domain Ω_e needs to be mapped to the master element with domain $\hat{\Omega}_e$. This can be achieved through the use of the Jacobian matrix. Figure 3.4 visually demonstrates the relationship of the deformed element and the master element through the Jacobian.

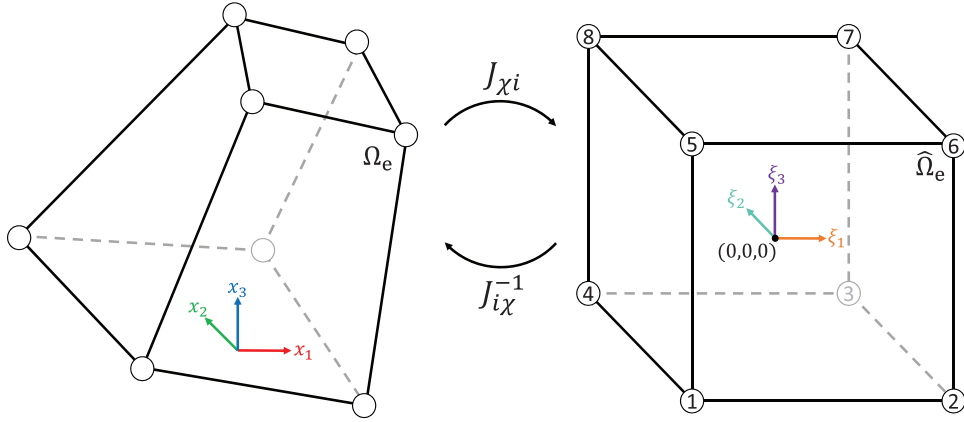


Figure 3.4: The Jacobian J_{ij} maps a deformed element Ω_e in the x_i coordinate system to the master element $\hat{\Omega}_e$ in the ξ_i coordinate system

The Jacobian \mathbf{J} is a matrix with components J_{χ^i} defined as the derivative of the global coordinates \mathbf{x} with respect to the local coordinates $\boldsymbol{\xi}$ as (see e.g., [75])

$$J_{\chi^i} \equiv \frac{\partial x_i}{\partial \xi_{\chi}} = x_{i,\chi} \quad (3.35)$$

Note here that the derivative of the global coordinate x_i with respect to the local

coordinate ξ_χ is represented as $x_{i,\chi}$; this notation will be used to represent the derivative with respect to ξ_χ . The inverse of the Jacobian can be shown (see e.g., [5]) to be the derivative of the local coordinates with respect to the global coordinates as

$$J_{i\chi}^{-1} = \xi_{\chi,i} \quad (3.36)$$

The global coordinates (x_1, x_2, x_3) of any local coordinate (ξ_1, ξ_2, ξ_3) can be found using the interpolation functions and the N local nodal locations $(\xi_1^n, \xi_2^n, \xi_3^n)$ in Equation (3.33) as

$$x_i = \sum_{n=1}^N \xi_i^n \psi^n(\boldsymbol{\xi}) \quad (3.37)$$

Using Equation (3.37) in Equation (3.35) yields

$$J_{\chi i} = \sum_{n=1}^N \xi_i^n \psi_{,\chi}^n \quad (3.38)$$

The Jacobian is applied within the strain–displacement submatrix \mathbf{B}_m in Equation (3.20). Currently, the submatrix \mathbf{B}_m contains derivatives of ψ^m with respect to the global coordinates \mathbf{x} , but the interpolation functions defined in Equation (3.34) are functions with respect to the local coordinates $\boldsymbol{\xi}$. Therefore, to find the derivatives of $\psi(\boldsymbol{\xi})$ with respect to \mathbf{x} , chain rule is used along with Equation (3.36).

$$\psi_{,i}^m = \xi_{\chi,i} \psi_{,\chi}^m = J_{i\chi}^{-1} \psi_{,\chi}^m \quad (3.39)$$

These equations are then applied in the \mathbf{B}_m matrix in Equation (3.20) to map any valid 8–noded element to the master element as

$$\mathbf{B}_m(\xi_1, \xi_2, \xi_3) = \begin{bmatrix} J_{1\chi}^{-1} \psi_{,\chi}^m & 0 & 0 \\ 0 & J_{2\chi}^{-1} \psi_{,\chi}^m & 0 \\ 0 & 0 & J_{3\chi}^{-1} \psi_{,\chi}^m \\ 0 & J_{3\chi}^{-1} \psi_{,\chi}^m & J_{2\chi}^{-1} \psi_{,\chi}^m \\ J_{3\chi}^{-1} \psi_{,\chi}^m & 0 & J_{1\chi}^{-1} \psi_{,\chi}^m \\ J_{2\chi}^{-1} \psi_{,\chi}^m & J_{1\chi}^{-1} \psi_{,\chi}^m & 0 \end{bmatrix} \quad (3.40)$$

allowing the finite element equations to be expressed in the local coordinates $\boldsymbol{\xi}$ of the master element instead of the global coordinates \mathbf{x} of the system.

The Jacobian is also used to transform the global volume integral over Ω_e in Equation (3.16) to a local volume integral over $\hat{\Omega}_e$ as (see e.g., [5])

$$d\Omega_e = dx_1 dx_2 dx_3 = \det(\mathbf{J}) d\xi_1 d\xi_2 d\xi_3 = \det(\mathbf{J}) d\hat{\Omega}_e \quad (3.41)$$

3.2.3 Numerical Integration

For a general element without orthogonal sides, there are not closed form expressions to express the solution to Equation (3.16). Thus a numerical approach to approximate the solution is necessary. Numerical methods allow for a numerical estimation of a complex analytic mathematical operation without calculating the analytic function itself.

There are many ways to numerically evaluate an integral, but the method often chosen for use in finite elements is Gauss quadrature. Gauss quadrature estimates an integral from -1 to 1 by a sum of the integrand evaluated at N_{gp} integration points (or Gauss points) $\hat{\xi}^n$ multiplied by a corresponding weight coefficient w^n as

$$\int_{-1}^1 f(\xi) d\xi \approx \sum_{n=1}^{N_{gp}} w^n f(\hat{\xi}^n) \quad (3.42)$$

Note that the superscript n refers to the n^{th} term in the series and is not a power; this notation is selected in order to reserve the subscript as a reference to the dimension of the variable, as discussed shortly.

Equation (3.42) has N_{gp} unknown weights w_i and N_{gp} unknown integration points $\hat{\xi}_i$, or $2N_{gp}$ unknowns for one equation. To calculate all $2N_{gp}$ unknowns, the Equation (3.42) is evaluated for simple choices of $f(\xi)$, namely

$$f(\xi) = \xi^\alpha \quad \alpha \in \{0, 1, \dots, 2N_{gp} - 1\} \quad (3.43)$$

Solving Equation (3.42) using the equations in (3.43), the weights and locations of the Gauss points for any value of N_{gp} can be solved for (see e.g., [76]). Therefore,

this numerical integration is exact for a polynomial of order $2N_{gp} - 1$, which is the most significant advantage of Gauss quadrature.

The Gauss quadrature method can easily be extended for use in multiple dimensions. Further note that it can be extended to integrals other than from -1 to 1; however, the use of the Jacobian above transforms the integration in Equation (3.16) to the required domain for Gauss quadrature to be used.

$$\int_{-1}^1 \int_{-1}^1 \int_{-1}^1 f(\xi_1, \xi_2, \xi_3) d\xi_1 d\xi_2 d\xi_3 \approx \sum_{m=1}^{N_{gp}^1} \sum_{n=1}^{N_{gp}^2} \sum_{p=1}^{N_{gp}^3} w_1^m w_2^n w_3^p f(\hat{\xi}_1^m, \hat{\xi}_2^n, \hat{\xi}_3^p) \quad (3.44)$$

where N_{gp}^χ refers to the number of Gauss points in the ξ_χ direction as the number of Gauss points used in each direction need not be equivalent.

The use of Gauss quadrature approximates the triple integrals in Equations (3.27) through (3.29) as triple summations. For example, the form of the Equation for the \mathbf{K}^e in Equation (3.27) now becomes

$$\begin{aligned} \mathbf{K}^e &= \int_{-1}^1 \int_{-1}^1 \int_{-1}^1 [\mathbf{B}(\xi_1, \xi_2, \xi_3)]^T \mathbf{C} \mathbf{B}(\xi_1, \xi_2, \xi_3) \det(\mathbf{J}) d\xi_1 d\xi_2 d\xi_3 \\ &\approx \sum_{m=1}^{N_{gp}^1} \sum_{n=1}^{N_{gp}^2} \sum_{p=1}^{N_{gp}^3} w_1^m w_2^n w_3^p [\mathbf{B}(\hat{\xi}_1^m, \hat{\xi}_2^n, \hat{\xi}_3^p)]^T \mathbf{C} \mathbf{B}(\hat{\xi}_1^m, \hat{\xi}_2^n, \hat{\xi}_3^p) \det(\mathbf{J}) \end{aligned} \quad (3.45)$$

3.3 Solving the Finite Element Problem for Material Stiffness Prediction

Now that the finite element equations have been fully developed, Equation (3.32) can now be used to solve specific problems. A geometry is created and then discretized into specific elements (called a mesh). Once the mesh is created, a series of boundary and initial conditions can be applied to the global system in Equation (3.32) and the system solved.

The methods presented in Section 3.2 were discussed in general for any structural mechanics problem. The specific problem being considered in this study is the stiffness tensor prediction of a stationary heterogeneous material representative

volume element (RVE). Therefore the methods for solving Equation (3.32) will be presented in this section with this context in mind. Further, the RVE in question is allowed to be a heterogeneous material, where each constituent material has a known stiffness matrix; for example, the stiffness properties could be that of a fiber and resin system forming a laminated fabric composite.

3.3.1 Theory of Material Stiffness Property Prediction

The theory for determining the components of the concatenated form of the stiffness tensor \mathbf{C} in Equation (3.22) can be explained by looking at the matrix form of the generalized Hooke's Law in Equation (3.3). For a given \mathbf{C} , when a strain $\boldsymbol{\varepsilon}$ is applied, the resulting stresses $\boldsymbol{\sigma}$ can be calculated as

$$\begin{Bmatrix} \sigma_{11} \\ \sigma_{22} \\ \sigma_{33} \\ \sigma_{23} \\ \sigma_{13} \\ \sigma_{12} \end{Bmatrix} = \begin{bmatrix} C_{1111} & C_{1122} & C_{1133} & C_{1123} & C_{1113} & C_{1112} \\ C_{1122} & C_{2222} & C_{2233} & C_{2223} & C_{2213} & C_{2212} \\ C_{1133} & C_{2233} & C_{3333} & C_{3323} & C_{3313} & C_{3312} \\ C_{1123} & C_{2223} & C_{3323} & C_{2323} & C_{2313} & C_{2312} \\ C_{1113} & C_{2213} & C_{3313} & C_{2313} & C_{1313} & C_{1312} \\ C_{1112} & C_{2212} & C_{3312} & C_{2312} & C_{1312} & C_{1212} \end{bmatrix} \begin{Bmatrix} \varepsilon_{11} \\ \varepsilon_{22} \\ \varepsilon_{33} \\ \varepsilon_{23} \\ \varepsilon_{13} \\ \varepsilon_{12} \end{Bmatrix} \quad (3.46)$$

However, if \mathbf{C} is unknown, as is the case in the present context of an RVE, then the values of the components of \mathbf{C} must be determined “experimentally”. In other words, the RVE of the object is placed under a strain state in finite elements, the average stresses are measured, and then the components of \mathbf{C} calculated. Unfortunately, the problem is now underdefined for a single strain state where one has 6 equations for 21 unknowns.

It is reasonable to apply a set of randomized strain states to an RVE and determine the concatenated form of the stiffness tensor using some form of optimization scheme. In the present work, a more direct approach is used: Each of six individual strain states are applied one at a time to determine uniquely a given column of the concatenated form of the stiffness tensor \mathbf{C} . For example, if a ε_{11} is applied while all

other strains are 0, then the system in Equation (3.47) becomes

$$\begin{Bmatrix} \sigma_{11} \\ \sigma_{22} \\ \sigma_{33} \\ \sigma_{23} \\ \sigma_{13} \\ \sigma_{12} \end{Bmatrix} = \begin{bmatrix} C_{1111} & C_{1122} & C_{1133} & C_{1123} & C_{1113} & C_{1112} \\ C_{1122} & C_{2222} & C_{2233} & C_{2223} & C_{2213} & C_{2212} \\ C_{1133} & C_{2233} & C_{3333} & C_{3323} & C_{3313} & C_{3312} \\ C_{1123} & C_{2223} & C_{3323} & C_{2323} & C_{2313} & C_{2312} \\ C_{1113} & C_{2213} & C_{3313} & C_{2313} & C_{1313} & C_{1312} \\ C_{1112} & C_{2212} & C_{3312} & C_{2312} & C_{1312} & C_{1212} \end{bmatrix} \begin{Bmatrix} \varepsilon_{11} \\ 0 \\ 0 \\ 0 \\ 0 \\ 0 \end{Bmatrix} \quad (3.47)$$

which simplifies down to a set of six algebraic expressions in terms of ε_{11} and the resulting σ_{ij} values.

$$C_{1111} = \frac{\sigma_{11}}{\varepsilon_{11}}, C_{1122} = \frac{\sigma_{22}}{\varepsilon_{11}}, C_{1133} = \frac{\sigma_{33}}{\varepsilon_{11}}, C_{1123} = \frac{\sigma_{23}}{\varepsilon_{11}}, C_{1113} = \frac{\sigma_{13}}{\varepsilon_{11}}, C_{1112} = \frac{\sigma_{12}}{\varepsilon_{11}} \quad (3.48)$$

As ε_{11} is applied, and the resulting σ_{ij} can be measured from the finite element analysis, the first column of \mathbf{C} can be calculated. This process can be repeated for the other five applied strain states to fully determine \mathbf{C} . The RVE is geometrically periodic, or one repeating cell of an infinitely expansive volume, so even if the cell is deformed, it must remain periodic without overlap. If this condition is met, the calculated stiffness tensor will naturally be symmetric.

In order to calculate the stresses from the finite element model, it is convenient to have a uniform strain state on the boundary of the RVE. However, as Xia *et al.* [25] pointed out, this is not as simple as fixing one boundary and then prescribing a displacement on the opposing boundary; in fact, this method will overconstrain the system and the boundaries will not be able to displace freely. Periodic boundary conditions with added displacement allow for source and destination boundaries to be displaced relative to one another while still allowing the geometry to deform according to the applied strains.

A cuboid RVE, as represented in Figure 3.5, has six faces whose normal vectors are parallel to one of the three coordinate axes. The RVE occupies the region $\{0 \leq x_1 \leq \Delta x_1; 0 \leq x_2 \leq \Delta x_2; 0 \leq x_3 \leq \Delta x_3\}$; in order for the RVE to be periodic in all

directions, the following conditions must be imposed (see e.g., [25])

$$\begin{aligned}
u_1(\Delta x_1, x_2, x_3) &= u_1(0, x_2, x_3) + \bar{\varepsilon}_{11} \Delta x_1 \\
u_1(x_1, \Delta x_2, x_3) &= u_1(x_1, 0, x_3) + \frac{\bar{\varepsilon}_{12} \Delta x_2}{2} \\
u_1(x_1, x_2, \Delta x_3) &= u_1(x_1, x_2, 0) + \frac{\bar{\varepsilon}_{13} \Delta x_3}{2} \\
u_2(\Delta x_1, x_2, x_3) &= u_2(0, x_2, x_3) + \frac{\bar{\varepsilon}_{12} \Delta x_1}{2} \\
u_2(x_1, \Delta x_2, x_3) &= u_2(x_1, 0, x_3) + \bar{\varepsilon}_{22} \Delta x_2 \\
u_2(x_1, x_2, \Delta x_3) &= u_2(x_1, x_2, 0) + \frac{\bar{\varepsilon}_{23} \Delta x_3}{2} \\
u_3(\Delta x_1, x_2, x_3) &= u_3(0, x_2, x_3) + \frac{\bar{\varepsilon}_{13} \Delta x_1}{2} \\
u_3(x_1, \Delta x_2, x_3) &= u_3(x_1, 0, x_3) + \frac{\bar{\varepsilon}_{23} \Delta x_2}{2} \\
u_3(x_1, x_2, \Delta x_3) &= u_3(x_1, x_2, 0) + \bar{\varepsilon}_{33} \Delta x_3
\end{aligned} \tag{3.49}$$

where $\bar{\varepsilon}_{ij}$ refers to an applied averaged strain state. Note that for an applied shear strain ($\bar{\varepsilon}_{23}$, $\bar{\varepsilon}_{13}$, and $\bar{\varepsilon}_{12}$), two separate boundary conditions are necessary. Further, for shear deformation, the applied displacement is halved in order to account for the difference in true shear strain and engineering shear strain. Notice that all of these conditions must be applied regardless of the strain state prescribed. The methods on mathematically applying the boundary conditions in Equations (3.49) will be presented in detail in Section 3.3.3.

The system needs to be anchored at some point in the body to prevent rigid body translations. For simplicity, the node at the origin is chosen to be fixed, thus

$$\begin{aligned}
u_1(0, 0, 0) &= 0 \\
u_2(0, 0, 0) &= 0 \\
u_3(0, 0, 0) &= 0
\end{aligned} \tag{3.50}$$

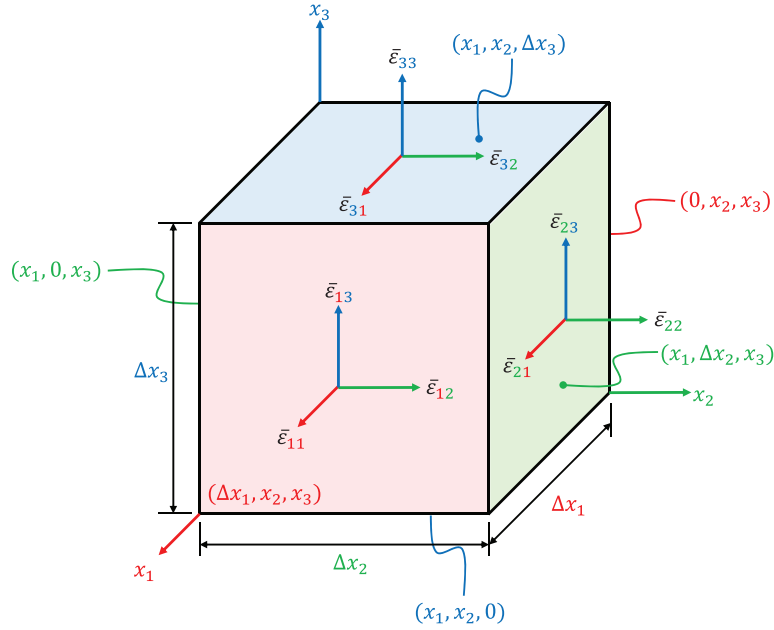


Figure 3.5: An example of a cuboid representative volume element (RVE), with applied strains $\bar{\epsilon}_{ij}$ and dimensions labeled.

3.3.2 Problem-Specific Simplifications to the Finite Element Equations

Now that the theory behind RVE material stiffness property prediction has been established, the finite element approach to perform these tasks can be established. The three-dimensional structural mechanics problem was shown in Equation (3.32). However, problem-specific simplifications can be made to the general finite element form to reduce the complexity of the finite element equations further. The simplifications pertinent to the material stiffness property prediction problem are as follows:

- **Stationary System.** Some problems have a load or displacement that is applied over a time period, such as modeling the material response to an impact; this, however, is not required for linear elastic material property prediction, so $\ddot{\mathbf{u}} = \mathbf{0}$ in Equation (3.32).

- **No Internal Body Forces.** In Equation (3.29), \mathbf{f} refers to applied internal body forces on an object, which are assumed to be negligible, i.e., $\mathbf{F} = \mathbf{0}$.
- **No Applied Surface Traction or Point Loads.** Equation (3.30) defines the \mathbf{Q} vector, containing the resulting nodal reaction forces caused by applied point loads, surface tractions, and displacements. There is no applied point loads or surface tractions, meaning the nodal reaction force is zero when the nodal displacement is unknown.

These three simplifications reduce the global finite element equation to

$$\mathbf{K}\mathbf{u} = \mathbf{Q} \tag{3.51}$$

Typically in stationary solid mechanics systems, both \mathbf{u} and \mathbf{Q} are column vectors having the length of the number of nodal degrees of freedom (3) times the nodes (N). However, multiple displacement states can be calculated simultaneously by concatenating P desired displacement states into one matrix and the P applied loads in another. In other words, \mathbf{u} and \mathbf{Q} , respectively, become

$$\mathbf{u} = [\mathbf{u}^1 \quad \mathbf{u}^2 \quad \dots \quad \mathbf{u}^P] \quad \mathbf{Q} = [\mathbf{Q}^1 \quad \mathbf{Q}^2 \quad \dots \quad \mathbf{Q}^P] \tag{3.52}$$

Thus, multiple solutions to the global system in Equation (3.51) can be solved simultaneously as

$$[\mathbf{u}^1 \quad \mathbf{u}^2 \quad \dots \quad \mathbf{u}^P] = \mathbf{K}^{-1} [\mathbf{Q}^1 \quad \mathbf{Q}^2 \quad \dots \quad \mathbf{Q}^P] \tag{3.53}$$

greatly reducing computational efforts. This becomes particularly useful in material property prediction as the same stiffness matrix \mathbf{K} can be used to simultaneously calculate the reaction forces from all six strain states.

3.3.3 Boundary Conditions

In order for the finite element equations to be properly utilized, boundary conditions need to be applied. In Equation (3.51), boundary conditions can be prescribed through a displacement within \mathbf{u} or a boundary force in \mathbf{Q} . Often, there will be a mix of displacements and boundary forces, thus various components of \mathbf{u} or \mathbf{Q} will be known, but at every nodal degree of freedom, either the displacement or force will be known. If no displacement is specifically applied at a node, because no surface tractions or point loads are applied, the resulting reaction force is zero; if there is an applied displacement, then the reaction force remains unknown.

Periodic boundary conditions, as presented in Equation (3.49), refer to a special form of conditions where the value of displacements or forces at one boundary of the geometry (the destination) is dependent on the value of the displacements or forces on the opposing boundary (the source). This form of boundary condition is used when a large geometry can be fully represented by a reduced, geometrically periodic RVE.

The periodicity in this thesis is enforced through the displacements, where the displacement on the destination face (u_d) is equivalent to the displacements on the source face (u_s) plus a constant c [25].

$$u_d = u_s + c \quad (3.54)$$

The constant c is related to the average strain $\bar{\epsilon}$, where

$$\bar{\epsilon} \approx \frac{u_d - u_s}{\Delta x} \quad (3.55)$$

where Δx is the distance between the source and destination faces. Thus, from Equations (3.54) and (3.55),

$$c = \bar{\epsilon} \Delta x \quad (3.56)$$

To ensure that periodicity of the geometry is maintained in the boundary forces in the absence of body forces, the reaction forces on the opposing faces are equivalent in magnitude, but opposite in direction by the balance of forces (see e.g., [25]).

$$Q_s = -Q_d \quad (3.57)$$

To demonstrate how to implement the periodic boundary conditions, a one-dimensional system of three nodes shall be considered. The three nodes are shown in Figure 3.6, where x_s and x_d are, respectively, the source and displacement positions, and x_o is some nodal location between them. Upon assembly, the full system looks like (see e.g. [77])

$$\begin{bmatrix} \mathbf{K}_{ss} & \mathbf{K}_{sd} & \mathbf{K}_{so} \\ \mathbf{K}_{ds} & \mathbf{K}_{dd} & \mathbf{K}_{do} \\ \mathbf{K}_{os} & \mathbf{K}_{od} & \mathbf{K}_{oo} \end{bmatrix} \begin{Bmatrix} u_s \\ u_d \\ u_o \end{Bmatrix} = \begin{Bmatrix} Q_s \\ Q_d \\ Q_o \end{Bmatrix} \quad (3.58)$$

where the subscript s refers to the source, d refers to the destination, and o refers to the other non-periodic nodes in the system. With Equations (3.54) and (3.57), the system becomes

$$\begin{bmatrix} \mathbf{K}_{ss} & \mathbf{K}_{sd} & \mathbf{K}_{so} \\ \mathbf{K}_{ds} & \mathbf{K}_{dd} & \mathbf{K}_{do} \\ \mathbf{K}_{os} & \mathbf{K}_{od} & \mathbf{K}_{oo} \end{bmatrix} \begin{Bmatrix} u_s \\ u_s + c \\ u_o \end{Bmatrix} = \begin{Bmatrix} -Q_d \\ Q_d \\ Q_o \end{Bmatrix} \quad (3.59)$$

The first and second rows of this matrix system can be added together in order to eliminate the Q_d terms. Simplifying the equation yields

$$(\mathbf{K}_{dd} + \mathbf{K}_{ds} + \mathbf{K}_{sd} + \mathbf{K}_{ss}) u_s + (\mathbf{K}_{do} + \mathbf{K}_{so}) u_o = -c(\mathbf{K}_{dd} + \mathbf{K}_{sd}) \quad (3.60)$$

The third row of the matrix equation can be simplified as well.

$$(\mathbf{K}_{od} + \mathbf{K}_{os}) u_s + \mathbf{K}_{oo} u_o = Q_o - c\mathbf{K}_{od} \quad (3.61)$$

Reformatting Equations (3.60) and (3.61) into matrix form yields (see e.g., [77])

$$\begin{bmatrix} \mathbf{K}_{dd} + \mathbf{K}_{ds} + \mathbf{K}_{sd} + \mathbf{K}_{ss} & \mathbf{K}_{do} + \mathbf{K}_{so} \\ \mathbf{K}_{od} + \mathbf{K}_{os} & \mathbf{K}_{oo} \end{bmatrix} \begin{Bmatrix} u_s \\ u_o \end{Bmatrix} = \begin{Bmatrix} -c(\mathbf{K}_{dd} + \mathbf{K}_{sd}) \\ Q_o - c\mathbf{K}_{od} \end{Bmatrix} \quad (3.62)$$

Equation (3.62) demonstrates that the displacements of the destination nodes are not calculated directly during the solution process, but rather are calculated in the post-processing phase by using Equation (3.54).

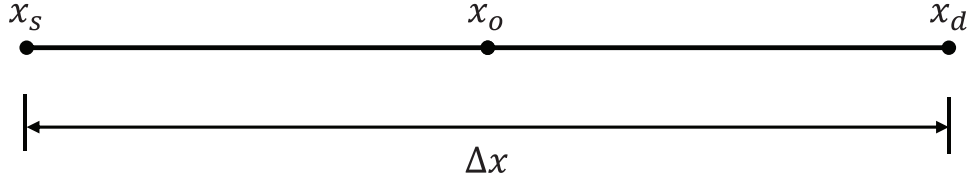


Figure 3.6: A three-noded one-dimensional periodic system

3.3.4 Partitioning and Solving the Finite Element Equations

Once the boundary conditions are applied to the global system, the matrix system in Equation (3.51) is ready to be solved. As mentioned previously, each nodal degree of freedom will either have an unknown displacement or an unknown reaction force, but not both. Further, the stiffness matrix \mathbf{K} is calculated from selected interpolation functions $\psi^m(\mathbf{x})$ and from the selected contracted form of the stiffness tensor \mathbf{C} .

Before solving the system of equations, it is beneficial to partition the system in terms of the free nodes \mathbf{u}_f and the prescribed nodes \mathbf{u}_p . This form allows rapid implementation within the computational framework. The displacement vector is recast as

$$\mathbf{u} = \begin{Bmatrix} \mathbf{u}_f \\ \mathbf{u}_p \end{Bmatrix} \quad (3.63)$$

using elementary row operations. The finite element form of Equation (3.51) is then rewritten as

$$\begin{bmatrix} \mathbf{K}_{ff} & \mathbf{K}_{fp} \\ \mathbf{K}_{pf} & \mathbf{K}_{pp} \end{bmatrix} \begin{Bmatrix} \mathbf{u}_f \\ \mathbf{u}_p \end{Bmatrix} = \begin{Bmatrix} \mathbf{Q}_f \\ \mathbf{Q}_p \end{Bmatrix} \quad (3.64)$$

The unknowns in Equation (3.64) are \mathbf{u}_f and \mathbf{Q}_p . Knowing this, the entire system

can be solved within two steps. The first series of rows are rewritten as

$$\mathbf{u}_f = \mathbf{K}_{ff}^{-1}(\mathbf{Q}_f - \mathbf{K}_{fp}\mathbf{u}_p) \quad (3.65)$$

Then, from the second series of rows from Equation (3.64), once \mathbf{u}_f is known, yields the solution for the reaction forces \mathbf{Q}_p

$$\mathbf{Q}_p = \mathbf{K}_{pf}\mathbf{u}_f + \mathbf{K}_{pp}\mathbf{u}_p \quad (3.66)$$

Thus solutions of Equations (3.65) and (3.66) yields the unknown displacements \mathbf{u}_f and unknown reaction forces \mathbf{Q}_p .

3.4 Post-Processing

After performing the matrix operations necessary to solve for all of the displacements and reaction forces in the system, the contracted form of the stiffness tensor \mathbf{C} of the RVE in Figure 3.5 can be calculated. This is performed as described in Equation (3.48); the average stress over the RVE can be divided by the applied strain state $\bar{\varepsilon}$ to determine each component in the appropriate column of \mathbf{C} .

To calculate the average stresses $\bar{\sigma}_{ij}$, each component of the stress tensor σ_{ij} is integrated over the domain and divided by the total volume $V = \Delta x_1 \Delta x_2 \Delta x_3$ as

$$\bar{\sigma}_{ij} = \frac{1}{V} \int_{\Omega} \sigma_{ij} \, d\Omega \quad (3.67)$$

While this is a valid way of determining the average stresses in the system, Gauss theorem and the local equations of motion from Equation (3.2) can be used to simplify the calculation to directly use the reaction forces on the boundaries found in \mathbf{Q} (see e.g., [2, 25]). To start, it can be shown that σ_{ij} is equivalent to $(\sigma_{ik}x_j)_{,k}$ by expanding out the latter term using product rule as

$$(\sigma_{ik}x_j)_{,k} = \sigma_{ik,k}x_j + \sigma_{ik}x_{j,k} \quad (3.68)$$

Based on the assumptions presented in Section 3.3.2, there are no body forces or acceleration in the system, so the local equations of motion in Equation (3.2) reduces down to

$$\sigma_{ij,j} = 0 \quad (3.69)$$

Using Equation (3.69), Equation (3.68) can continue to be expanded as

$$(\sigma_{ik}x_j)_{,k} = \sigma_{ik,k}x_j + \sigma_{ik}x_{j,k} = \sigma_{ik}\delta_{jk} = \sigma_{ij} \quad (3.70)$$

where δ_{ij} refers to the Kronecker delta function. Thus it has been shown that $\sigma_{ij} = (\sigma_{ik}x_j)_{,k}$, so Equation (3.69) becomes

$$\bar{\sigma}_{ij} = \frac{1}{V} \int_{\Omega} (\sigma_{ik}x_j)_{,k} d\Omega \quad (3.71)$$

Gauss theorem can be applied to Equation (3.71) to recast the volume integral to a surface integral as (see e.g., [5])

$$\bar{\sigma}_{ij} = \frac{1}{V} \int_{\Omega} (\sigma_{ik}x_j)_{,k} d\Omega = \frac{1}{V} \int_{\Gamma} \sigma_{ik}x_j n_k d\Gamma \quad (3.72)$$

Using the assumption that the reactions on opposite faces are periodic as in Equation (3.57), and that $n_k = -1$ on the source face Γ_k^s and $n_k = 1$ on the destination face Γ_k^d , this can be further reduced to (see e.g., [25])

$$\frac{1}{V} \int_{\Gamma} \sigma_{ik}x_j n_k d\Gamma = \frac{1}{V} \left(\int_{\Gamma_k^d} \sigma_{ik}^d x_j^d d\Gamma - \int_{\Gamma_k^s} \sigma_{ik}^s x_j^s d\Gamma \right) = \frac{1}{V} \int_{\Gamma_k^d} \sigma_{ik}^d (x_j^d - x_j^s) d\Gamma \quad (3.73)$$

where s refers to the source face and d refers to the destination face. If $k \neq j$, then the integral reduces to 0 as $x_j^d - x_j^s = 0$. However, if $k = j$, then $x_j^d - x_j^s = \Delta x_j$, which is constant. This Δx_j term then can be pulled out of the integral as

$$\bar{\sigma}_{ij} = \frac{\Delta x_j}{V} \int_{\Gamma_j} \sigma_{ij} d\Gamma \quad (3.74)$$

The integral of σ_{ij} over the surface Γ_j is sum of the reaction forces on the positive x_j face. Therefore, the calculation of $\bar{\sigma}_{ij}$ is (see e.g., [25])

$$\bar{\sigma}_{ij} = \frac{R_{ij}}{S_j} \quad (\text{no sum on } j) \quad (3.75)$$

where S_j refers to the surface area of the positive x_j face, and R_{ij} refers to the sum of the reaction forces acting in the x_i direction upon the positive x_j face.

Once the average stresses are calculated, the components of the concatenated form of the stiffness tensor are calculated by dividing the column of the average stresses by the applied strain, as in Equation (3.48). When this is performed for all 6 applied strain states, the full 6×6 contracted form of the stiffness tensor of the RVE \mathbf{C} is determined.

CHAPTER FOUR

The Multiphase Voxel Element (MVE)

Now that a foundational understanding of the various processes involved in solving finite element problems has been built, a discussion can be had on the four types of multiphase voxel elements (MVEs) developed and studied in this thesis. This chapter will go in depth into the theory behind how each MVE is constructed, as well as provide studies on simple materials to compare the effectiveness of each method.

4.1 Motivation

The goal of this research is to develop a finite element for use in the Petrov-Galerkin formulation capable of containing multiple materials while also being entirely independent of internal material boundaries. WiseTex [47] and TexGen [7,48] are effective meshing programs for select weave geometries; this work seeks to formulate an alternative meshing configuration that can be applied to multiple-material systems.

Research has already been performed by Whitcomb *et al.* [49–52] on a type of homogenized element termed a “macroelement”. Nakai *et al.* [57] and Iarve *et al.* [58] both determined methods for superimposing the local mesh of the fiber upon the global homogeneous mesh of the matrix. However, these methods require that a geometry-specific mesh be defined and solved for each representative volume element (RVE) that constitutes the entire woven geometry. Sometimes, geometry data is only available pointwise, as extracted from a three-dimensional ultrasound scan (see e.g., [8]) or a micro CT scan (see e.g., [9, 10]). It would be convenient to have a means to analyze these geometries without having to explicitly model and mesh the data. Further, some meshes of complex geometries contain ill-conditioned elements,

whereby the Jacobian of the element approaches singularity. It would be beneficial to have an element that can build a consistent mesh with no risk of ill-conditioned elements.

Recent developments in extended finite elements (XFEM) have proven promising for studies in crack propagation (see e.g., [68]). The power of XFEM is through the superposition of enrichment functions that allow greater refinement within an element; this means that elements built through the XFEM process can ignore material discontinuities. However, in order to enrich the element, extra degrees of freedom have to be added, and therefore more computational resources are required.

The use of voxel elements is an alternative to the traditional meshing process whereby a mesh of equal-sized and shaped elements can be superimposed upon a two-dimensional image or three-dimensional scan (see e.g., [72]). The material property within each voxel can either be the material with the highest volume fraction within the element (see e.g., [62]) or some homogenization method for these voxels are employed (see e.g., [11, 14]). However, the former is usually selected to reduce model setup and computational effort which can produce sharp spikes in stress due to “stairstep-like” material boundaries [62]. The homogenized voxel methods often used in literature range from using rule-of-mixtures to homogenize voxels containing material boundaries (see e.g., [14, 15]) to applying the material properties at the integration points (see e.g., [11, 12]). Caselman showed in his thesis [1] that the use of the latter method can be improved upon through the use of strain corrections at each integration point. The purpose of the present study is to further improve upon these homogenized voxel elements where material properties are applied at the Gauss points; these shall be termed “multiphase voxel elements” (MVEs) in this thesis.

Figure 4.1 shows two flowcharts comparing the process behind using traditional finite elements versus MVEs. The desired characteristics of an MVE are to

1. Accurately predict the stiffness tensor of heterogeneous structures with complex geometries using material information at the integration points.
2. Evaluate an element domain that contains more than one material type with an infinite gradient in properties along an internal boundary, such as between the resin and the fiber tow.
3. Mesh a domain entirely independent of internal geometry. In other words, the mesh can be generated before internal geometry is considered (as shown in Figure 4.1).

4.2 Selected Multiphase Voxel Elements

For this research, four types of MVEs are investigated, and the construction of each element is discussed in detail in this section. Studies on simple geometries are provided in this chapter to highlight strengths and weaknesses of each method. The application of each method to woven composite material stiffness properties are presented in Chapter Five.

An algorithm scans each element for the materials contained within its domain at discrete points and uses that information to build an element that approximates the homogenized stiffness properties of the element as a whole. Because the stiffness matrix \mathbf{K}^e is often computed through Gauss quadrature (or a similar numerical scheme), it is convenient to have the material information collected along with applying any corrections at the individual Gauss points. For each of the elements presented, it is assumed that an equal number of N_{gp} Gauss points are used in each of the coordinate directions.

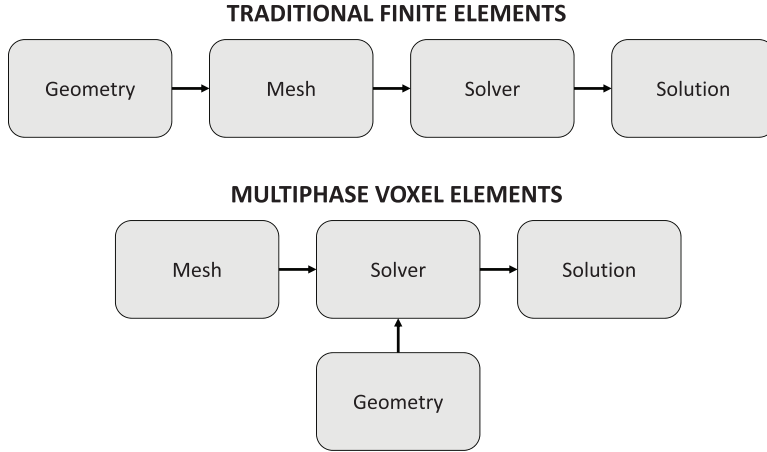


Figure 4.1: The process for using traditional finite elements versus the process for using MVEs. For MVEs, the geometry can be considered as the system is being solved for.

4.2.1 Average Stiffness Element (ASE)

The average stiffness element (ASE) is the simplest of the MVEs investigated. The concept is that the element-wise average $\langle C_{ijkl} \rangle$ of the individual stiffness tensor components $\tilde{C}_{ijkl}(\mathbf{x})$ over the volume of the element, calculated as

$$\langle C_{ijkl} \rangle = \frac{1}{V} \iiint_V \tilde{C}_{ijkl}(\mathbf{x}) dV \quad (4.1)$$

is used as the stiffness property within the finite element calculation in Equation (3.27). This formulation is similar to the volume fraction-based homogenization method presented by Kim and Swan [14] and Watanabe *et al.* [15], but extended for more than two materials in the element.

To evaluate this integral numerically is straight-forward. The values of the stiffness tensor is determined at each of the Gauss points within the element, and then all of the individual stiffness tensors are summed and divided by the total number of Gauss points, evaluated as

$$\langle C_{ijkl} \rangle = \frac{1}{N_{gp}^3} \sum_{m=1}^{N_{gp}} \sum_{n=1}^{N_{gp}} \sum_{p=1}^{N_{gp}} \tilde{C}_{ijkl}(\hat{\xi}_m, \hat{\xi}_n, \hat{\xi}_p) \quad (4.2)$$

The integration in (3.45) is then calculated independent of any spatial variation in \mathbf{C} .

This method is not provided as a potential solution, but merely as the reference which the other methods will be compared to in order to demonstrate improvement. It is expected that a more realistic MVE should perform as good as or better than the averaging method.

4.2.2 Basic Multiphase Voxel Element (B-MVE)

Zeng *et al.* [12,64] devised a simple method to homogenize elements for use in mechanical and failure analyses of three-dimensional braided composites. The method is a numerical technique that applies the separate material properties individually at the n^{th} Gauss point $\hat{\xi}_i^n$ within the numerical integral calculation of the stiffness matrix \mathbf{K}^e .

$$\mathbf{K}^e = \sum_{m=1}^{N_{gp}} \sum_{n=1}^{N_{gp}} \sum_{p=1}^{N_{gp}} w_1^m w_2^n w_3^p [\mathbf{B}(\hat{\xi}_1^m, \hat{\xi}_2^n, \hat{\xi}_3^p)]^T \mathbf{C}(\hat{\xi}_1^m, \hat{\xi}_2^n, \hat{\xi}_3^p) \mathbf{B}(\hat{\xi}_1^m, \hat{\xi}_2^n, \hat{\xi}_3^p) \det(\mathbf{J}) \quad (4.3)$$

As previously discussed in Chapter Two Section 2.4.4, Zeng *et al.* [12] used this method to study the effects of braid angle on engineering properties; compared against experimental results from literature, the method showed reasonable accuracy for planar tensile modulus while showing exceptional accuracy for out-of-plane tensile modulus. No experimental comparisons were made for shear modulus or Poisson's ratio. The method was also used to predict the failure of braided composites with reasonable agreement to experimental results [64]. There is, however, room for improvement in both studies, as discussed in Section 4.2.3.

This approach to the finite elements problem is beneficial in that it alleviates the issues involved with meshing complex geometries by accommodating multiple material properties within an element. The element can reference an analytic geometric

function, results from a scan of a geometry, or even a preexisting mesh to determine the material property at each Gauss point. For the purpose of this study, the element presented by Zeng *et al.* will be referred to as the Basic Multiphase Voxel Element (B–MVE).

4.2.3 Tensile Modulus Corrected Multiphase Voxel Element (TMC–MVE)

Caselman [1], in his thesis, evaluated the applicability of the B–MVE for a unidirectional fiber reinforced composite by altering the volume composition of the element’s two materials and solving for the effective material properties. For both a one–dimensional and three–dimensional isotropic system, Caselman discovered that the B–MVE element produces a rule–of–mixtures result that was not characteristic of the actual system. He postulated that the B–MVE did not account for the change in the strain field that occurs across the material boundary within the element. This is because the selected interpolation functions $\boldsymbol{\psi}(\boldsymbol{\xi})$ from Equation (3.34) are forced to be linear across the entire heterogeneous element, whereas the strain is only truly linear within the same material.

Using a one–dimensional spring analogy (as depicted in Figure 4.2), Caselman proposed a means to “correct” the strain within the element by using the material properties to adjust the derivatives of the interpolation functions (which are analogous to the strain in the finite element equations). Assuming a two–material spring system with stiffnesses k^1 and k^2 , the effective stiffness of the springs in series k^{eff} can be determined.

$$k^{eff} = \frac{k^1 k^2}{k^1 + k^2} \quad (4.4)$$

Recognizing that the tensile modulus E^q , where q is the q^{th} material in a line of springs, both constituent materials and the effective material E^{eff} can be related to

their respective spring constants by

$$k^q = \frac{E^q A}{L^q} \quad (4.5)$$

where L^q refers to the length of the material and A refers to the cross-sectional area. Using Equation (4.5) in Equation (4.4), the value of E^{eff} evaluates to (assuming equal cross-section areas)

$$E^{eff} = \frac{E^1 E^2}{\beta^1 E^2 + \beta^2 E^1} \quad (4.6)$$

where β^q is a line fraction evaluated as

$$\beta^q = \frac{L^q}{L^1 + L^2} \quad (4.7)$$

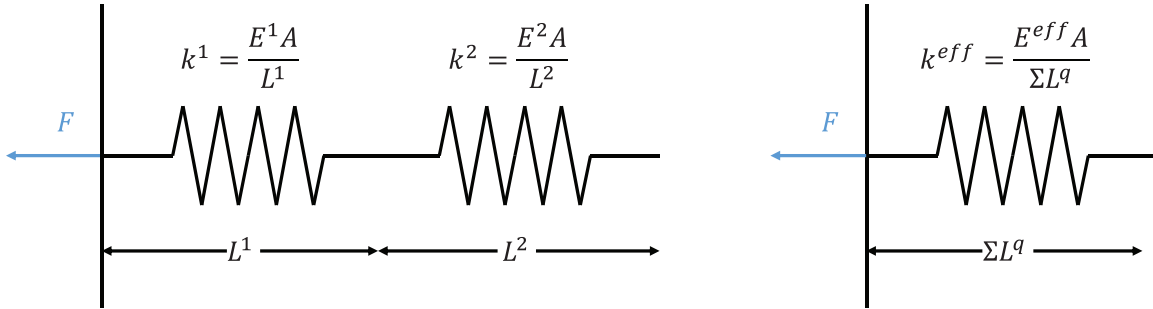


Figure 4.2: A visual depiction of the spring analogy used by Caselman [1]

Two springs in series have different values of strains ε^q distributed across the two materials. By only applying the material that is at each Gauss point, the value of strain calculated ε_{eff} would be equivalent in both materials. To correct this, a relationship between the actual strain within the material and the effective strain being calculated (the “correction”) needs to be determined. This is done by using the force-equivalent nature of two springs in series and their resultant equivalent spring, expressed as

$$\frac{F}{A} = E^1 \varepsilon^1 = E^2 \varepsilon^2 = E^{eff} \varepsilon^{eff} \quad (4.8)$$

Solving for the ratio of each material strain to the effective strain yields the correction factor α^q that is applied to the interpolation functions at each Gauss point.

$$\alpha^q = \frac{\varepsilon^q}{\varepsilon^{eff}} = \frac{E^{eff}}{E^q} \quad (4.9)$$

At each Gauss point, this correction factor is multiplied into terms within the strain-displacement matrix \mathbf{B} . The value of the correction factor depends on the material at the Gauss point. For a one-dimensional system, this is mathematically equivalent to applying E^{eff} to the entire element.

The extension to three dimensions may be made by treating each line of Gauss points as a spring system. Each Gauss point is treated as a part of three different spring systems, each with their own line fraction.

In Caselman's presentation [1], only the isotropic tensile modulus E of two materials is used; there is no extension of the method to orthotropic materials that have different tensile moduli (E_1, E_2, E_3) in each of the coordinate directions or to elements containing more than two materials. Caselman only needed two isotropic materials for his studies of short fiber composites, so in this research his efforts are extended to more than two orthotropic materials within the element. The tensile moduli E_i will be used instead of the isotropic tensile modulus E . This modified element will be referred to the Tensile Modulus Corrected Multiphase Voxel Element (TMC-MVE).

Expanding into three dimensions, the evaluation of the correction factors expand to include a dimension on the line fraction β^q . So now the subscript i refers to the dimension x_i in which the value is calculated. Thus the corrections in Equation (4.9) become

$$\alpha_i^q = \frac{E_i^{eff}}{E_i^q} \quad (\text{no sum on } i) \quad (4.10)$$

where

$$E_i^{eff} = \frac{E_i^1 E_i^2}{\beta_i^1 E_i^2 + \beta_i^2 E_i^1} \quad (\text{no sum on } i) \quad (4.11)$$

and

$$\beta_i^q = \frac{L_i^q}{L_i^1 + L_i^2} \quad (\text{no sum on } i) \quad (4.12)$$

The TMC–MVE was originally developed for an element containing two isotropic materials for use in analysis of short fiber composites [1]. Short fiber composites may contain glass or carbon fibers within a polymer matrix, both isotropic, so this element worked well for that application. However, woven composites are made from an isotropic matrix and a transversely isotropic strand. Because of this difference, the strand’s properties vary with direction, meaning there are more than two sets of stiffness tensors to account for in the formulation of \mathbf{K}^e .

Returning to Caselman’s original derivation, in Equation (4.4), he presents the effective stiffness of two springs in series. This is actually the specific case of a more generalized form for calculating the effective stiffness of multiple springs in series; the method can be extended to calculate the effective stiffness of N_{gp} Gauss points springs in series as

$$\frac{1}{k_i^{eff}} = \sum_{q=1}^{N_{gp}} \frac{1}{k_i^q} \quad (4.13)$$

When including the relation between k^q and E^q in Equation (4.5), Equation (4.13) becomes

$$\frac{1}{E_i^{eff}} = \sum_{q=1}^{N_{gp}} \frac{\beta_i^q}{E_i^q} \quad (\text{no sum on } i) \quad (4.14)$$

where β_i^q is (as generalized from Equation (4.7))

$$\beta_i^q = \frac{L_i^q}{\sum_{r=1}^{N_{gp}} L_i^r} \quad (\text{no sum on } i) \quad (4.15)$$

It is worth noting that β_i^q can also be calculated from the Gauss weights w_i^q used in

the numerical integration.

$$\beta_i^q = \frac{w_i^q}{2} \quad (4.16)$$

With this more general form for calculating the effective stiffness E_i^{eff} , the correction factors α_i^q can be calculated for any number of materials included within the element.

These expanded correction factors are then applied to each of the individual submatrices of the strain–displacement matrix presented in Equation (3.40) by multiplying the strain correction α_i^q with the corresponding $\psi_{,i}^m$ as

$$\hat{\mathbf{B}}_m^q = \begin{bmatrix} \alpha_1^q J_{1X}^{-1} \psi_{,X}^m & 0 & 0 \\ 0 & \alpha_2^q J_{2X}^{-1} \psi_{,X}^m & 0 \\ 0 & 0 & \alpha_3^q J_{3X}^{-1} \psi_{,X}^m \\ 0 & \alpha_3^q J_{3X}^{-1} \psi_{,X}^m & \alpha_2^q J_{2X}^{-1} \psi_{,X}^m \\ \alpha_3^q J_{3X}^{-1} \psi_{,X}^m & 0 & \alpha_1^q J_{1X}^{-1} \psi_{,X}^m \\ \alpha_2^q J_{2X}^{-1} \psi_{,X}^m & \alpha_1^q J_{1X}^{-1} \psi_{,X}^m & 0 \end{bmatrix} \quad (4.17)$$

These corrections are applied based upon the representation of the strain ε_{ij} in the finite element equations. From Equation (3.1), strains are represented as spatial derivatives of the displacement u_i . However, from the approximation of the displacement in Equation (3.14), the spatial derivatives are applied to the interpolation functions $\psi_{,i}^m$. Ergo, the strain corrections α_i^q in Equation (4.10) multiply into the derivatives of the interpolation functions because these derivatives are analogous to strain.

With Equation (4.17), the elemental stiffness matrix is evaluated as

$$\mathbf{K}^e = \sum_{m=1}^{N_{gp}} \sum_{n=1}^{N_{gp}} \sum_{p=1}^{N_{gp}} w_1^m w_2^n w_3^p [\hat{\mathbf{B}}^q(\hat{\xi}_1^m, \hat{\xi}_2^n, \hat{\xi}_3^p)]^T \mathbf{C}(\hat{\xi}_1^m, \hat{\xi}_2^n, \hat{\xi}_3^p) \hat{\mathbf{B}}^q(\hat{\xi}_1^m, \hat{\xi}_2^n, \hat{\xi}_3^p) \det(\mathbf{J}) \quad (4.18)$$

where $\hat{\mathbf{B}}^q$ is the corresponding strain–displacement matrix for the integration point located at $(\hat{\xi}_1^m, \hat{\xi}_2^n, \hat{\xi}_3^p)$ with the appropriate corrections as calculated in Equation (4.17).

The strain corrections for the TMC–MVE reduce down to the strain corrections presented in Caselman [1] when there are only two materials within the domain of the element and both materials are isotropic.

4.2.4 *Stiffness Tensor Corrected Multiphase Voxel Element (STC–MVE)*

For non–isotropic materials, the other stiffness properties (such as shear modulus G) are independent of the tensile modulus E . Thus it is desirable to expand the TMC–MVE to account for the coupling between extension and shearing prevalent in the non–isotropic materials that compose woven composites. A new element is presented that utilized strain corrections based directly on the components of the stiffness tensor and will therefore be referred to as the Stiffness Tensor Corrected Multiphase Voxel Element (STC–MVE).

For a three dimensional object, stress and strain are expressed in terms of the stiffness tensor C_{ijkl} using Equation (3.3). The stiffness tensor components will therefore be used in lieu of engineering constants. A similar form for the strain correction α_{ij}^q is defined, where some effective stiffness tensor component C_{ijkl}^{eff} is divided by the individual property of the material C_{ijkl}^q at the Gauss point q in question as

$$\alpha_{ij}^q = \frac{C_{ijkl}^{eff}}{C_{ijkl}^q} \quad (\text{no sum on } i, j) \quad (4.19)$$

This form, similar to Equation (4.10), is used to maintain the analogy that a line of integration points is analogous to a line of springs. The difference here is that the stiffness of each spring is now defined by components of the stiffness tensor C_{ijkl} , rather the tensile moduli E_i . The theory is that, for a three–dimensional system, the stiffness tensor C_{ijkl} more directly relates an applied strain ε_{ij} to a resulting stress σ_{ij} , as expressed in Equation (3.3). Further, this set of corrections includes contributions from the shear stiffness terms C_{2323} , C_{1313} , and C_{1212} , absent from the TMC–MVE.

With this proposed generalization, only the terms C_{ijij}^q (no sum on i, j) are used for the strain corrections. It is proposed that the six diagonal terms in the contracted form of the stiffness tensor \mathbf{C} most affect the six strain states as they most directly relate an applied strain ε_{ij} with its corresponding stress σ_{ij} . However, there is also expected to be some contribution from the other extension–extension terms (i.e., C_{1122} , C_{1133} , and C_{2233}), but this contribution is neglected in this present formulation. This choice will therefore neglect effects from the Poisson’s ratios. Future work should be performed to determine a way to apply the contributions from these terms.

The corrected individual strain–displacement submatrices in Equation (4.17) is then updated to include the shear stiffness corrections, thus becoming

$$\hat{\mathbf{B}}_m^q = \begin{bmatrix} \alpha_{11}^q J_{1\chi}^{-1} \psi_{,\chi}^m & 0 & 0 \\ 0 & \alpha_{22}^q J_{2\chi}^{-1} \psi_{,\chi}^m & 0 \\ 0 & 0 & \alpha_{33}^q J_{3\chi}^{-1} \psi_{,\chi}^m \\ 0 & \alpha_{23}^q J_{3\chi}^{-1} \psi_{,\chi}^m & \alpha_{23}^q J_{2\chi}^{-1} \psi_{,\chi}^m \\ \alpha_{13}^q J_{3\chi}^{-1} \psi_{,\chi}^m & 0 & \alpha_{13}^q J_{1\chi}^{-1} \psi_{,\chi}^m \\ \alpha_{12}^q J_{2\chi}^{-1} \psi_{,\chi}^m & \alpha_{12}^q J_{1\chi}^{-1} \psi_{,\chi}^m & 0 \end{bmatrix} \quad (4.20)$$

The question now remains how the effective linear stiffness C_{ijij}^{eff} is calculated. There are two separate ways this term is calculated, one for the axial terms C_{iiii} and one for the shear terms C_{ijij} (where $i \neq j$).

The underlying argument for the axial strain corrections is that each Gauss point is a part of three spring systems, one in each of the orthogonal directions x_i , as depicted in Figure 4.3 (imagine each point is a spring with the value of stiffness labeled). A line of springs extending in the x_1 direction, for example, is affected by a strain in that direction (i.e., ε_{11}) alone. Therefore, the stiffness of these springs are determined only by the property that is affected by ε_{11} , in this case C_{1111} (again, the off–diagonal terms are being ignored as a part of this derivation). Thus, the effective

property C_{1111}^{eff} is calculated similar to that of E^{eff} in Equation (4.14) as

$$\frac{1}{C_{1111}^{eff}} = \sum_{q=1}^{N_{gp}} \frac{\beta_1^q}{C_{1111}^q} \quad (4.21)$$

A similar argument can be presented for C_{2222}^{eff} and C_{3333}^{eff} , or just C_{iii}^{eff} in general.

$$\frac{1}{C_{iii}^{eff}} = \sum_{q=1}^{N_{gp}} \frac{\beta_i^q}{C_{iii}^q} \quad (\text{no sum on } i) \quad (4.22)$$

Note that, again, a constraint for this approach is that only the material properties in the x_i direction contribute to C_{iii}^{eff} for any particular Gauss point. This will be an important concept to understand for deriving the effective shear components.

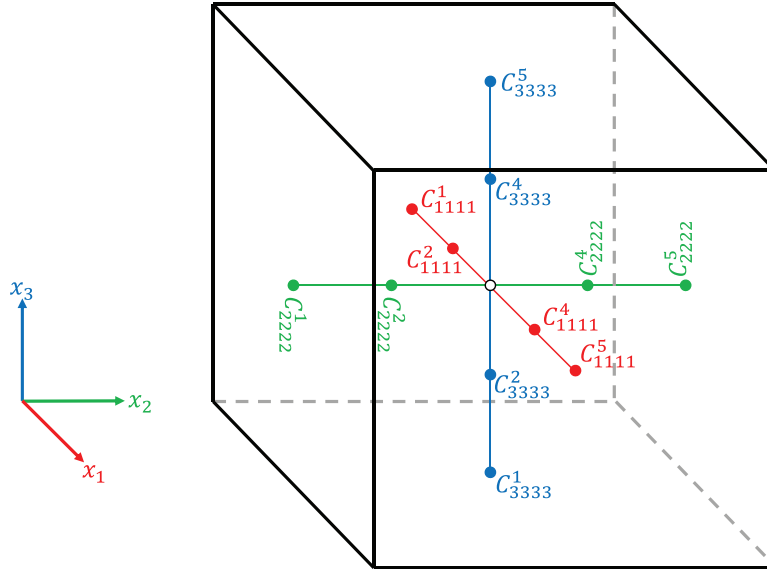


Figure 4.3: A visual demonstration showing which stiffness tensor components are accounted for in the axial effective stiffness components C_{iii}^{eff} . The white point is the integration point in question.

The shear terms are not as straight-forward. Because the shear strain ε_{ij} ($i \neq j$) affects two planes (the x_i - x_j plane), contributions of the shear stiffness tensor components C_{ijij} are required from the two lines of “springs” passing through a Gauss point in both the x_i and x_j directions. To further complicate matters, the material composition may not be equivalent in both of these directions. To overcome this

obstacle, a simple means of combining the properties from the two lines of springs into one is presented, producing a \bar{C}_{ijij}^{eff} that can be used in a form similar to Equation (4.22).

For simplicity, the shear term C_{2323}^q will be used in this explanation. Once the explanation is complete, similar techniques may be applied for C_{1212}^{eff} and C_{1313}^{eff} . Figure 4.4 visually demonstrates how to calculate the effective shear stiffness components. There are two sets of material properties that need to be considered: ${}^2C_{2323}^q$ and ${}^3C_{2323}^q$. The purpose of the superscript preceding these terms is to help describe from which axis x_i the material properties are coming from by adding directionality. So, for example, ${}^3C_{2323}^q$ refers to the stiffness tensor component C_{2323} located at the q^{th} Gauss point in the line of Gauss points extending in the x_3 direction.

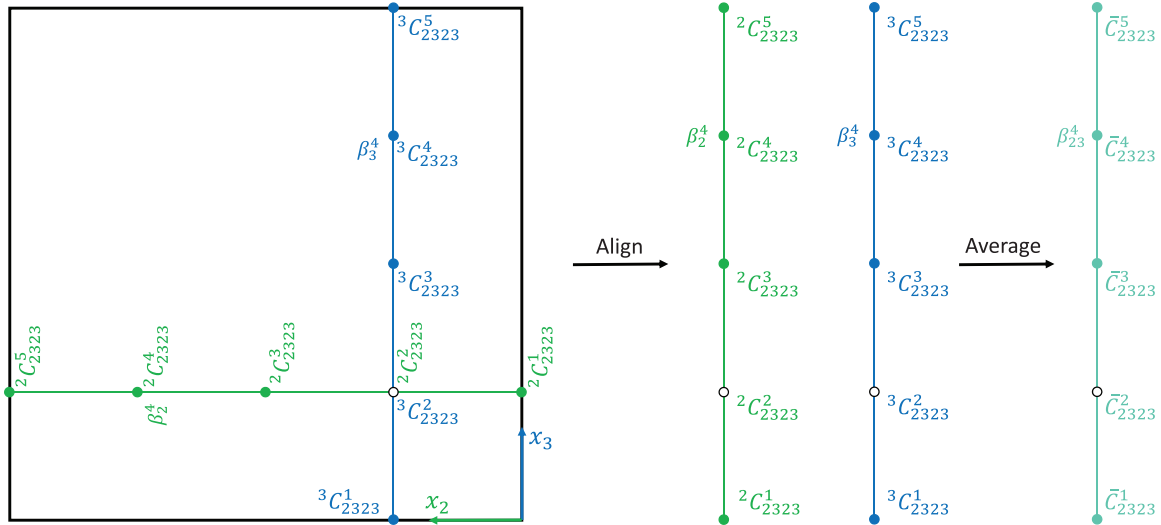


Figure 4.4: A visual demonstration showing how the shear stiffness tensor components are accounted for in the calculation of the effective shear stiffness component C_{2323}^{eff} . The white point is the integration point in question

To include the contributions from both of these materials, they are averaged together to form \bar{C}_{2323}^q . So, in general,

$$\bar{C}_{2323}^q = \frac{1}{2} ({}^2C_{2323}^q + {}^3C_{2323}^q) \quad (4.23)$$

This series of q averaged terms \bar{C}_{2323}^q are used in the calculation of C_{2323}^{eff} ;

$$\frac{1}{C_{2323}^{eff}} = \sum_{q=1}^{N_{gp}} \frac{\beta_{23}^q}{\bar{C}_{2323}^q} \quad (4.24)$$

where β_{23}^q is calculated in a similar manner as \bar{C}_{2323}^q as

$$\beta_{23}^q = \frac{1}{2} (\beta_2^q + \beta_3^q) \quad (4.25)$$

where β_i^q is the line fraction at the q^{th} integration point in the i^{th} dimension.

Table 4.1: List of all of the equations to determine the strain corrections for the STC-MVE

i	j	α_{ij}^q	$(C_{ijij}^{eff})^{-1}$	\bar{C}_{ijij}^q	β_{ij}^q
1	1	$\frac{C_{1111}^{eff}}{C_{1111}^q}$	$\sum \frac{\beta_{11}^q}{C_{1111}^q}$	${}^1C_{1111}^q$	β_1^q
2	2	$\frac{C_{2222}^{eff}}{C_{2222}^q}$	$\sum \frac{\beta_{22}^q}{C_{2222}^q}$	${}^2C_{2222}^q$	β_2^q
3	3	$\frac{C_{3333}^{eff}}{C_{3333}^q}$	$\sum \frac{\beta_{33}^q}{C_{3333}^q}$	${}^3C_{3333}^q$	β_3^q
2	3	$\frac{C_{2323}^{eff}}{C_{2323}^q}$	$\sum \frac{\beta_{23}^q}{\bar{C}_{2323}^q}$	$\frac{1}{2} ({}^2C_{2323}^q + {}^3C_{2323}^q)$	$\frac{1}{2} (\beta_2^q + \beta_3^q)$
1	3	$\frac{C_{1313}^{eff}}{C_{1313}^q}$	$\sum \frac{\beta_{13}^q}{C_{1313}^q}$	$\frac{1}{2} ({}^1C_{1313}^q + {}^3C_{1313}^q)$	$\frac{1}{2} (\beta_1^q + \beta_3^q)$
1	2	$\frac{C_{1212}^{eff}}{C_{1212}^q}$	$\sum \frac{\beta_{12}^q}{\bar{C}_{1212}^q}$	$\frac{1}{2} ({}^1C_{1212}^q + {}^2C_{1212}^q)$	$\frac{1}{2} (\beta_1^q + \beta_2^q)$

Summarizing Equations (4.23)–(4.25) for a general effective shear stiffness C_{ijij}^{eff}

(no sum on i, j):

$$\bar{C}_{ijij}^q = \frac{1}{2} ({}^iC_{ijij}^q + {}^jC_{ijij}^q) \quad (4.26)$$

$$\frac{1}{C_{ijij}^{eff}} = \sum_{q=1}^{N_{gp}} \frac{\beta_{ij}^q}{\bar{C}_{ijij}^q} \quad (4.27)$$

$$\beta_{ij}^q = \frac{1}{2} (\beta_i^q + \beta_j^q) \quad (4.28)$$

Further, Table 4.1 summarizes all of the necessary Equations to calculate all of the strain correction factors α_{ij}^q in Equation (4.19).

For the axial corrections, because the stiffness tensor components C_{iiii} (no sum on i) depend on both the tensile modulus E and Poisson's ratio ν (see e.g., [6]), the only time these corrections reduce down to the corrections in Caselman [1] is when there are two materials within the domain of the element that are both isotropic and have the same Poisson's ratio. For the shear corrections C_{ijij} (no sum on i, j), because of the averaging scheme to calculate the effective shear stiffness, the only time these corrections will reduce down to Caselman's formulation is if the shear moduli G of both materials is equivalent. However, if the materials are isotropic, the shear moduli depends upon both the tensile modulus and Poisson's ratio (see e.g. [6]). Therefore, the only time the corrections for the STC–MVE reduce down to Caselman's corrections is when the element is homogeneous.

4.3 Volume Fraction Studies

Before applying these MVEs to their desired application of woven composites, a set of studies is presented for simple systems to investigate their limits. The results are compared to traditional finite element results with a mesh that takes the material boundary into account. The next three sections each develop simple tests to compare the results of each of the introduced elements and provide the results over to a variety of material systems. The first test is based on volume fraction, the second test is based on rotation of the material properties, and the third on the the material boundary angle.

4.3.1 Description of Test Method

Caselman [1], in his thesis, used a simple test to compare the B–MVE to his own element; this test is depicted in Figure 4.5. A cube divided into two materials

is built. The material boundary is then shifted across the cube to alter the volume fraction of the two materials; at each volume fraction, the material properties are recorded and compared to the true finite element result with a high resolution mesh. The results are then plotted with respect to volume fraction.

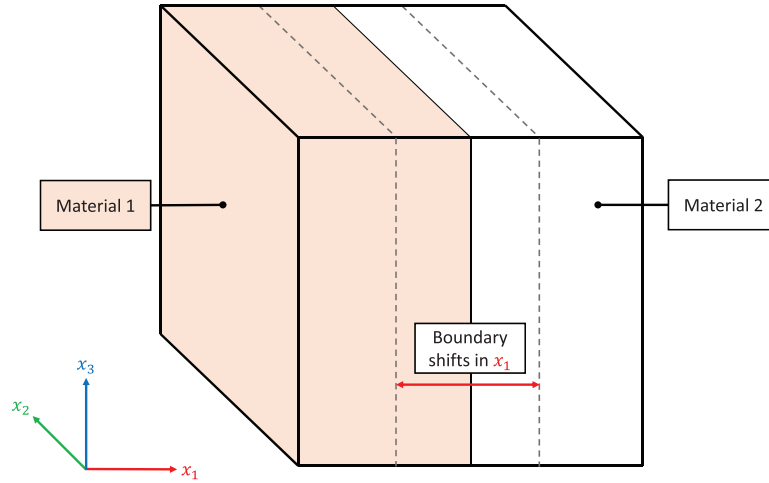


Figure 4.5: The volume fraction study

For this research, a similar study is performed using finite element code written in MATLAB. A two-material cube spanning $0 \leq x_i \leq 1$ for $\{i = 1, 2, 3\}$ was built with the material boundary parallel to the x_2 - x_3 plane. The material boundary was then shifted along the x_1 axis, recording the material properties at each volume fraction. The nine major non-zero stiffness tensor components (C_{1111} , C_{2222} , C_{3333} , C_{1122} , C_{1133} , C_{2233} , C_{2323} , C_{1313} , C_{1212}) are then plotted with respect to volume fraction.

The mesh for the traditional finite element solution is a simple mesh of $10 \times 10 \times 10$ linear hexahedral elements, with each material always containing 5 elements in the x_1 direction. For the numerical integration, three Gauss points in each direction are used for each element. The mesh of MVEs is $9 \times 9 \times 9$ equally sized elements, each element containing nine Gauss points in each direction. The MVE mesh remains constant, independent of the material boundary's position within the domain.

Two studies will be performed for each material system. For the first study, the volume fraction V_f of the first material will be altered from $\frac{4}{9} \leq V_f \leq \frac{5}{9}$. This is selected to allow the material boundary to pass through the middle set of element in the MVE; as V_f goes from $\frac{4}{9}$ to $\frac{5}{9}$, the plane shifts from one edge of the middle element to the opposite edge. This is meant to determine the behavior of each MVE depending on where the material boundary is within the element. The resulting stiffness tensor components for each MVE (as well as the true finite element response) are then plotted against the volume fraction. The absolute error for each MVE is also plotted; this is calculated by using the standard finite element approach as the true value:

$$Err_{ijkl}(V_f) \equiv \left| \frac{C_{ijkl}^{\text{true}}(V_f) - C_{ijkl}^{\text{MVE}}(V_f)}{C_{ijkl}^{\text{true}}(V_f)} \right| \quad (4.29)$$

The boundary locations selected in this study are the points directly between the Gauss points. The resolution of each MVE is affected by the number of integration points present; the material properties recorded will be the same as long as the material boundary remains between the same two Gauss points. An example of this is provided in Figure 4.6; the C_{1212} component for the isotropic/transversely isotropic study is plotted with respect to volume fraction at 30 equally-spaced points. Note how the solution does not change between Gauss points, marked by the dashed vertical lines. Selecting the point directly between each Gauss point provides a smooth curve by which a trend can more easily be determined.

The second set of results to be investigated in each MVE system will provide a more quantitative basis for comparing each MVE. The analysis of the cube is expanded to $0 \leq V_f \leq 1$, calculating the properties at fifty equally-spaced material boundary locations. Once all the material properties are calculated, the integral absolute error e_{ijkl} is calculated over the entire domain for each component of C_{ijkl} to

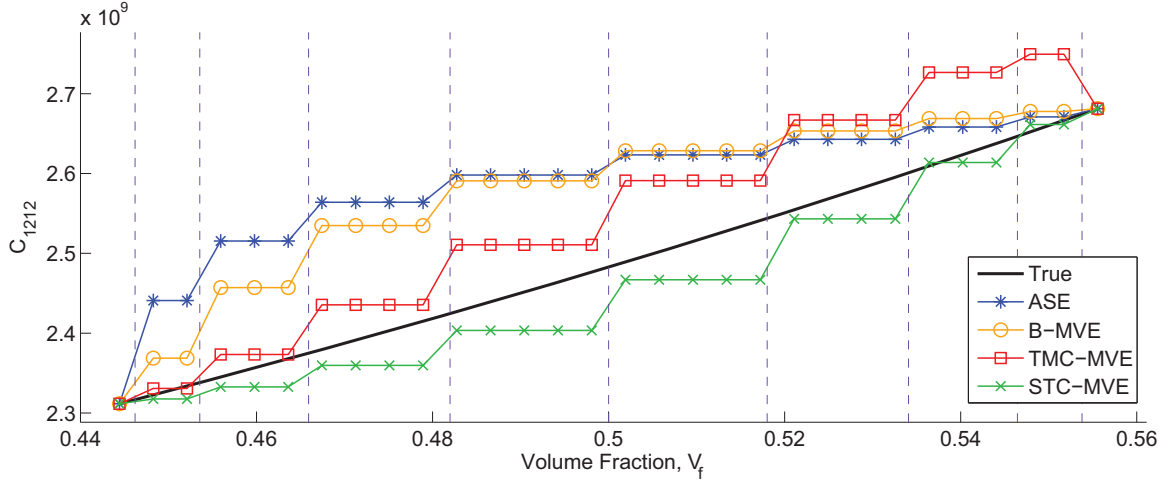


Figure 4.6: An example of the “stairstep-like” plot produced when the stiffness component is evaluated at an arbitrary number of volume fractions. The vertical dashed lines represent the locations of Gauss points.

provide one overall number to describe the total error of the MVE.

$$e_{ijkl} = \int_0^1 \left| \frac{C_{ijkl}^{\text{true}}(V_f) - C_{ijkl}^{\text{MVE}}(V_f)}{C_{ijkl}^{\text{true}}(V_f)} \right| dV_f \quad (4.30)$$

4.3.2 Results — Two Isotropic Materials

Isotropic materials are the most common material models system used. Most metals, as well as polymer matrices and fiber materials, are isotropic. An isotropic material has an infinite number of planes of symmetry, meaning they are invariant to rotation. The contracted form of the stiffness tensor \mathbf{C} of an isotropic material can be reduced to a relationship of two independent constants, C_{1111} and C_{1122} , as (see e.g., [6])

$$\mathbf{C} = \begin{bmatrix} C_{1111} & C_{1122} & C_{1122} & 0 & 0 & 0 \\ C_{1122} & C_{1111} & C_{1122} & 0 & 0 & 0 \\ C_{1122} & C_{1122} & C_{1111} & 0 & 0 & 0 \\ 0 & 0 & 0 & \frac{1}{2}(C_{1111} - C_{1122}) & 0 & 0 \\ 0 & 0 & 0 & 0 & \frac{1}{2}(C_{1111} - C_{1122}) & 0 \\ 0 & 0 & 0 & 0 & 0 & \frac{1}{2}(C_{1111} - C_{1122}) \end{bmatrix} \quad (4.31)$$

The material properties of the two isotropic materials (a fiber and a matrix) used were adapted from Sun and Vaidya [2] for a boron/aluminum composite, but the tensile moduli from are divided by 10 to better represent a fiber/matrix system (this has no effect on the trend of the results). These properties are listed in Table 4.2.

Figures 4.7 and 4.8 show the results of the one–element sweep for the two isotropic material system from the custom MATLAB code. Figure 4.7 presents various components of the effective stiffness tensor from each of the aforementioned methods, and Figure 4.8 shows the error as calculated using Equation (4.30) for each of the methods.

Table 4.2: The properties of the two isotropic materials used in this study, adapted from [2]

	Material 1 (Fiber)	Material 2 (Matrix)
E (GPa)	37.93	6.83
ν	0.1	0.3

The ASE tends to either undulate around the true solution or overpredict it, but never correctly follows the trend of the true finite element solution. The error of this element is, in general, the greatest on all nine of the major components test.

The B–MVE performs well in the directions where there is no change in material (C_{2222} , C_{3333} , C_{2233} , and C_{2323}), matching the trends of the true finite element solution almost perfectly (the error is on the order of 10^{-3}). However, this trend breaks down for any stiffness property that is affected by the material discontinuity in x_1 . Regardless, visually, the B–MVE performs better than the averaging method in nearly all scenarios as seen by the error plot of Figure 4.8.

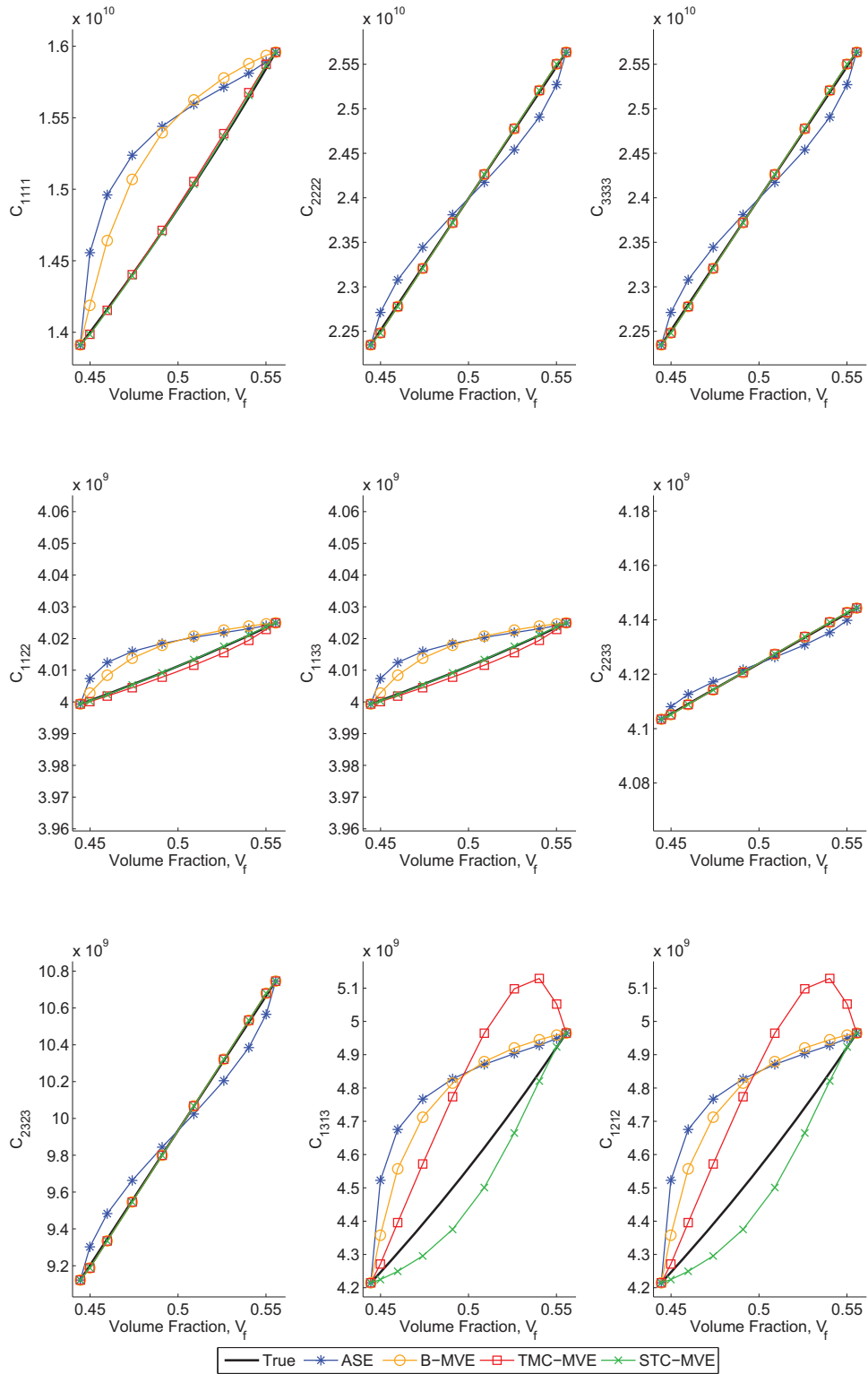


Figure 4.7: The values of the stiffness tensor C_{ijkl} vs. volume fraction (V_f) for the two isotropic material system

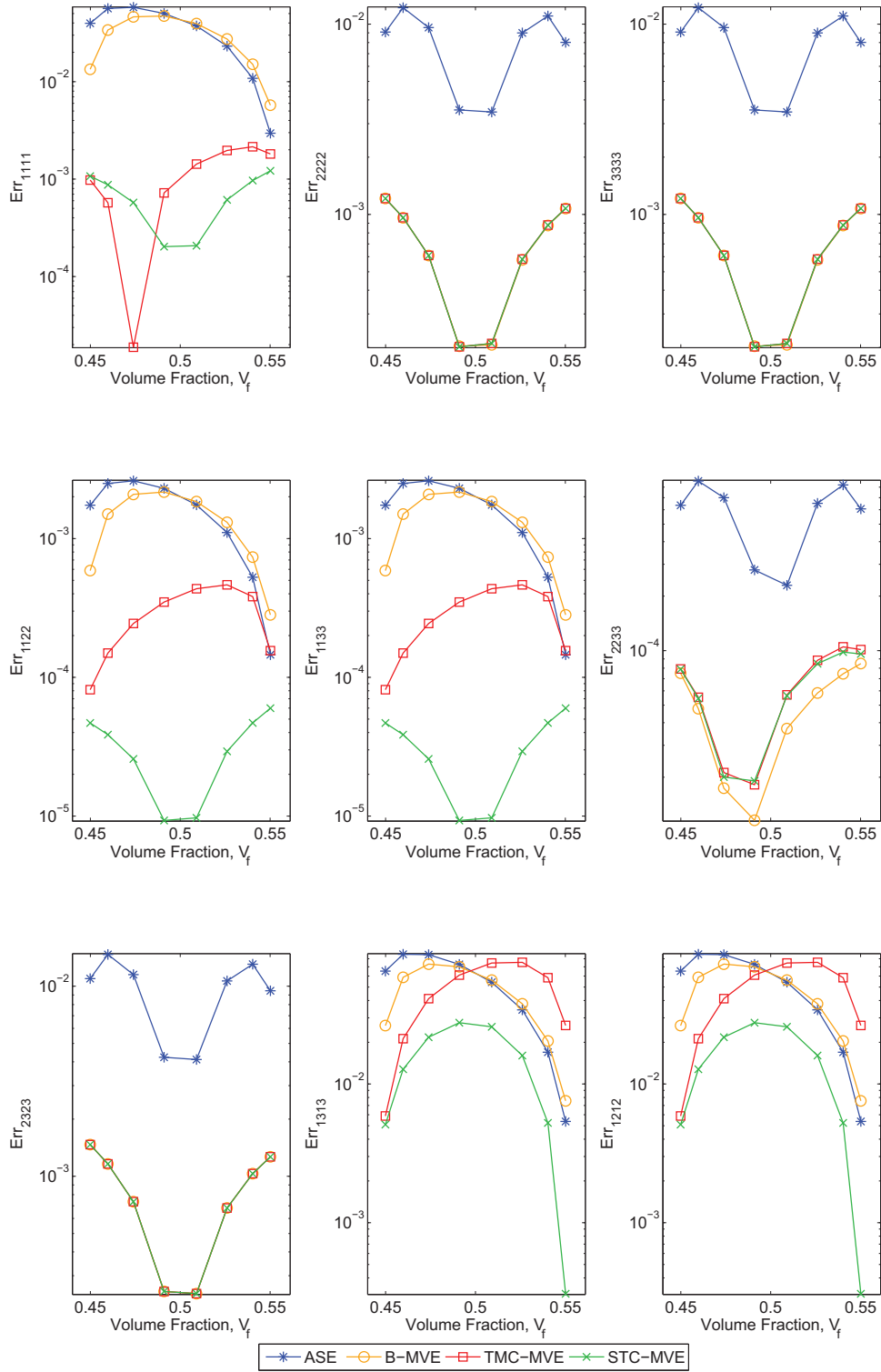


Figure 4.8: The error of the stiffness tensor Err_{ijkl} vs. volume fraction (V_f) for the two isotropic material system, calculated using Equation (4.29)

The TMC–MVE does well to correct most of the components from the B–MVE, with the exception of the shear stiffness terms C_{1122} and C_{1133} . The overall error is still much lower than with the B–MVE. However, it comes at the cost of an increased error in certain scenarios the shear terms C_{1212} and C_{1313} . Overall, outside of those shear terms, the TMC–MVE is an improvement upon the B–MVE.

The STC–MVE, as noted by Figure 4.8, is the most accurate method of those investigated in all but a few scenarios. But in those few cases, specifically C_{2233} and C_{1111} , the error remains less than the third significant digit. In the two worst performing stiffness component predictions — C_{1313} and C_{1212} — the STC–MVE still yields an error of $10^{-2} \sim 10^{-3}$; these results are better than all alternative methods presented.

Table 4.3: The percent integral absolute error for the isotropic study, calculated using Equation (4.30)

(%)	ASE	B–MVE	TMC–MVE	STC–MVE
e_{1111}	4.12	3.56	0.56	0.55
e_{2222}	0.91	0.52	0.52	0.52
e_{3333}	0.91	0.52	0.52	0.52
e_{1122}	0.25	0.22	0.05	0.04
e_{1133}	0.25	0.22	0.05	0.04
e_{2233}	0.06	0.03	0.03	0.03
e_{2323}	1.18	0.67	0.67	0.67
e_{1313}	6.81	5.98	4.94	2.15
e_{1212}	6.81	5.98	4.94	2.15

Table 4.3 provides the average percent absolute error for the stiffness tensor calculations for $0 \leq V_f \leq 1$, as described in Equation (4.30). Again, the ASE performs the worst in all cases. The B–MVE shows slight improvement from the ASE in most cases, but not by much; in the worst cases (C_{1313} and C_{1212}), the B–MVE

only reduces the error from 6.81% to 5.98%. The TMC–MVE is a much more substantial improvement over the averaging case than the B–MVE provided, dropping the error on C_{1111} from 3.56% to 0.56%. While the STC–MVE performs similarly to the TMC–MVE in most cases, the drop from 4.94% to 2.15% error on the C_{1313} and C_{1212} terms is noteworthy. Overall, the STC–MVE is either as good as or better than the alternative elements. The error on the calculation of the transverse shear stiffness terms C_{1313} and C_{1212} present the greatest error for all elements tested, ranging from 2.15% for the STC–MVE to 6.81% for the ASE. Given the results from Figures 4.7 and 4.8, this is not unexpected. None of the elements followed the trend for these shear stiffness terms perfectly, so it is expected that the error on these terms will be the greatest. Again, the trend previously noted still holds: the B–MVE provides marginal improvement over the ASE, the TMC–MVE provides a significant improvement over the B–MVE element, with the STC–MVE presenting the best overall performance.

4.3.3 Results — One Isotropic Material and One Transversely Isotropic Material

A transversely isotropic material is a material that has one plane of symmetry, and can be defined by five independent constants (C_{1111} , C_{2222} , C_{1122} , C_{2233} , and C_{1313} if the x_2 – x_3 plane is the plane of symmetry). An example of a transversely isotropic material is a unidirectional bundle of fibers infused within a matrix: the stiffest properties are aligned in the direction of the fiber. The stiffness tensor for a transversely isotropic material is given as (see e.g., [6])

$$\mathbf{C} = \begin{bmatrix} C_{1111} & C_{1122} & C_{1122} & 0 & 0 & 0 \\ C_{1122} & C_{2222} & C_{2233} & 0 & 0 & 0 \\ C_{1122} & C_{2233} & C_{2222} & 0 & 0 & 0 \\ 0 & 0 & 0 & \frac{1}{2}(C_{2222} - C_{2233}) & 0 & 0 \\ 0 & 0 & 0 & 0 & C_{1313} & 0 \\ 0 & 0 & 0 & 0 & 0 & C_{1313} \end{bmatrix} \quad (4.32)$$

A system of an isotropic and a transversely isotropic material is analogous to that of the constituent materials in a laminated composite; the matrix is generally isotropic, and the strand of fibers (a fiber/matrix system) is often considered transversely isotropic. Therefore, the set of material properties from one of the woven composites analyzed in the Chapter Five was selected for this study. The properties come from Scida *et al.* [3] for a plain weave E-glass/vinylester composite. The properties used are listed in Table 4.4.

Table 4.4: The properties of the isotropic material (vinylester) and the transversely isotropic material (E-glass/vinylester) used in this study, from [3]

		Material 1 (E-glass/Vinylester)	Material 2 (Vinylester)
E_{11}	(GPa)	57.5	3.4
$E_{22} = E_{33}$	(GPa)	18.8	3.4
$G_{12} = G_{13}$	(GPa)	7.44	1.49
G_{23}	(GPa)	7.26	1.49
$\nu_{12} = \nu_{13}$		0.25	0.35
ν_{23}		0.29	0.35

Figures 4.9 and 4.10 show the results from the volume fraction study performed in MATLAB for $\frac{4}{9} \leq V_f \leq \frac{5}{9}$, or across one set of MVEs. Some trends observed in the isotropic study are also observed here. The ASE performed worst overall and either undulates around the true solution or overpredicts it. The B-MVE performs well when the stiffness term is not affected by the material boundary moving in x_1 , but only provides marginal improvement on the other terms. The TMC-MVE underpredicts C_{1122} and C_{1133} , even more so than previously with the isotropic material, and the terms C_{1313} and C_{1212} are overpredicted around the same order that the ASE and B-MVE. Even so, the TMC-MVE performs well for the other components. The STC-MVE results are graphically indistinguishable for almost all of the stiffness tensor

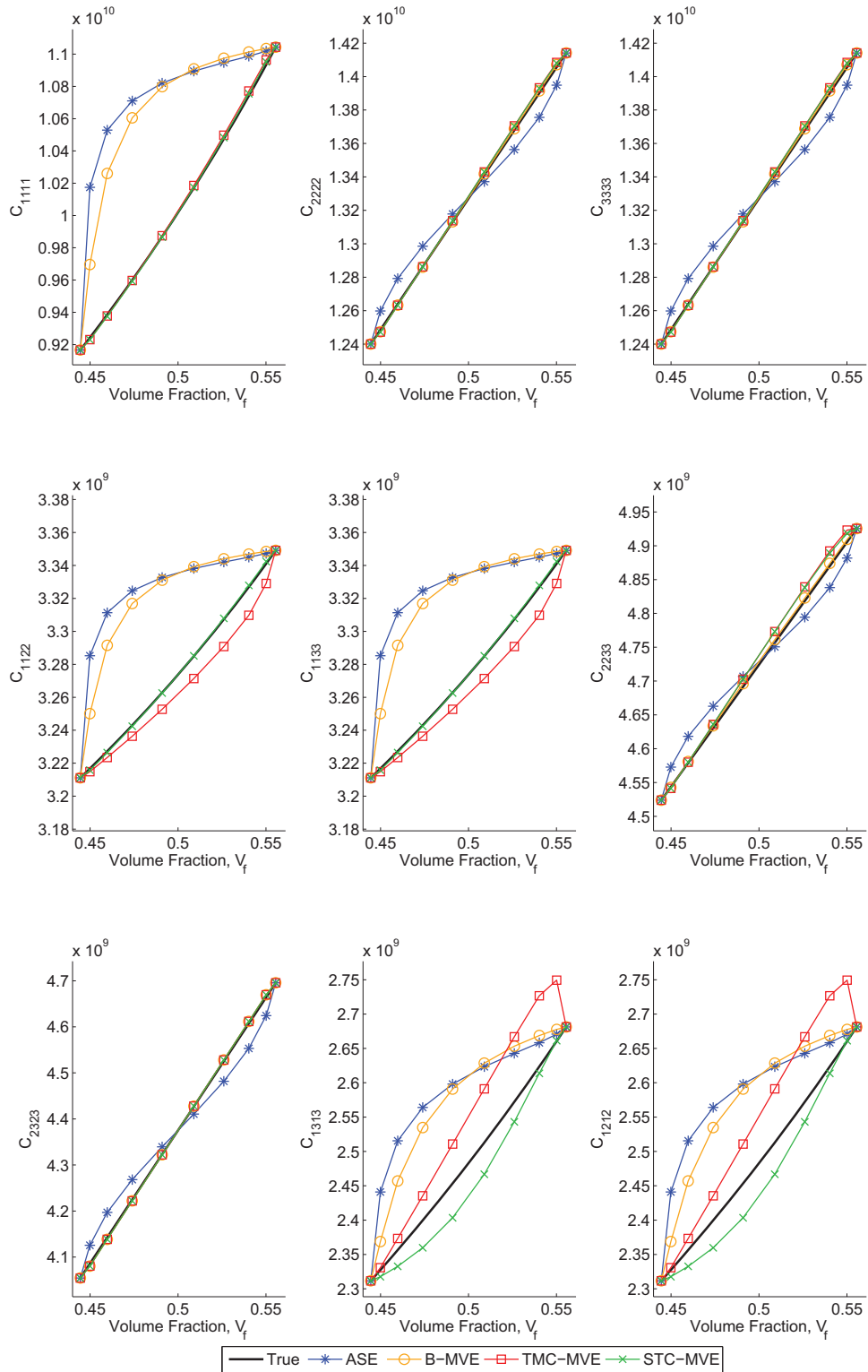


Figure 4.9: The values of the stiffness tensor C_{ijkl} vs. volume fraction (V_f) for the isotropic/transversely isotropic material system

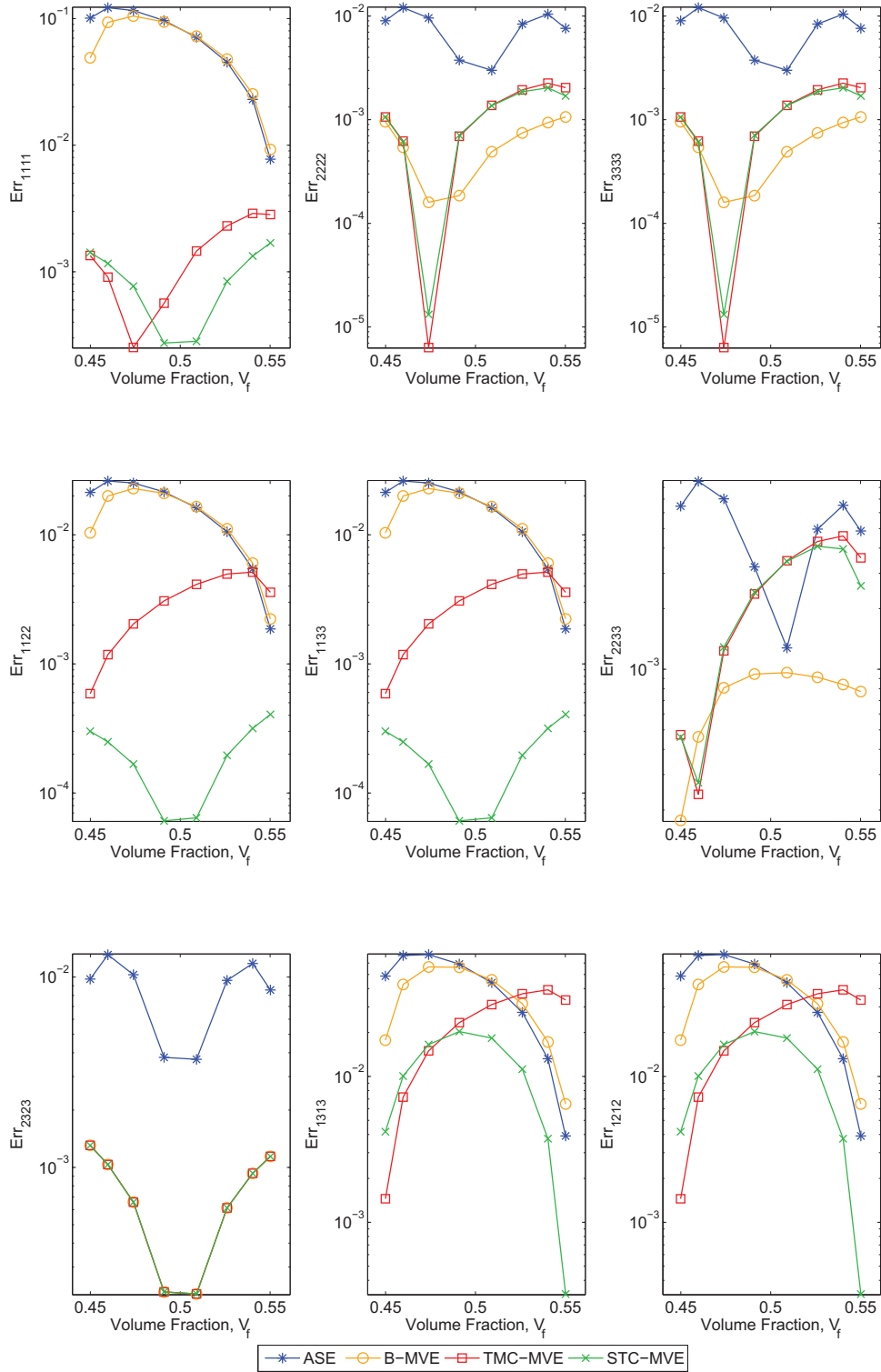


Figure 4.10: The error of the stiffness tensor Err_{ijkl} vs. volume fraction (V_f) for the isotropic/transversely isotropic material system, calculated using Equation (4.29)

components, with the exception of the shear stiffness terms C_{1313} and C_{1212} . There is also a slight overprediction on C_{2233} at the higher volume fractions (a similar case is noticed with the TMC–MVE). But as noted in Figure 4.10, the STC–MVE error for C_{1313} and C_{1212} is less than all alternatives and is between 10^{-2} and 10^{-3} .

Table 4.5 shows the percent integral absolute error for $0 \leq V_f \leq 1$, as calculated in Equation (4.30). As before, the ASE has the highest calculated error for each stiffness term; also as before, the B–MVE only provides a slight improvement over the ASE. The strain–corrected MVEs, the TMC–MVE and the STC–MVE, have similar errors, with the STC–MVE having reduced error over the TMC–MVE in the shear stiffness terms C_{1313} and C_{1212} (a 1.53% error versus 2.86% error).

Table 4.5: The percent integral absolute error for the isotropic/transversely isotropic study, calculated using Equation (4.30)

(%)	ASE	B–MVE	TMC–MVE	STC–MVE
e_{1111}	10.83	9.71	0.98	0.97
e_{2222}	0.88	0.49	0.49	0.49
e_{3333}	0.88	0.49	0.49	0.49
e_{1122}	3.75	3.40	0.52	0.38
e_{1133}	3.75	3.40	0.52	0.38
e_{2233}	0.62	0.37	0.38	0.37
e_{2323}	1.00	0.57	0.57	0.57
e_{1313}	5.08	4.42	2.86	1.53
e_{1212}	5.08	4.42	2.86	1.53

Again, the shear stiffness terms C_{1313} and C_{1212} were the among the least accurate for all of the MVEs studied. Interestingly, compared to the isotropic results in Table 4.3, the shear stiffness terms calculated by all of the MVEs were more accurate on this study. For example, for the ASE, the error for C_{1313} was calculated at 6.81% for the isotropic study, versus an error of 5.08% for the present study; this

also occurs despite an increase of error in C_{1111} from 4.12% in Table 4.3 to 10.83% in Table 4.5. This may suggest a correlation between the ratio of the stiffness properties of the materials within the MVE and the accuracy of the MVE. For reference, in the isotropic study, $G \approx 17.24$ GPa for material 1, and $G \approx 2.63$ GPa for material 2. Therefore, the ratio between these two properties is 6.56. In the present study, the ratio between the G_{12} value of material 1 and material 2 is 5.03, a slight decrease. The ratios of tensile moduli E_{11} for both studies presents a greater difference; in the isotropic study, the ratio is 5.55, whereas in the transversely isotropic study, the ratio is 16.9. This larger difference in ratio correlates to a larger error calculation.

4.3.4 Results — Two Orthotropic Materials

An orthotropic material is a material that exhibits symmetry only across two orthogonal planes (and subsequently, across a third mutually orthogonal plane) [6]. The representative volume element for a laminated woven composite, when the axes are aligned to the principal directions, are often orthotropic materials. The contracted form of the tensor for an orthotropic material is dependent upon nine independent constants as (see e.g., [6])

$$\mathbf{C} = \begin{bmatrix} C_{1111} & C_{1122} & C_{1133} & 0 & 0 & 0 \\ C_{1122} & C_{2222} & C_{2233} & 0 & 0 & 0 \\ C_{1133} & C_{2233} & C_{3333} & 0 & 0 & 0 \\ 0 & 0 & 0 & C_{2323} & 0 & 0 \\ 0 & 0 & 0 & 0 & C_{1313} & 0 \\ 0 & 0 & 0 & 0 & 0 & C_{1212} \end{bmatrix} \quad (4.33)$$

The materials selected for this study of two orthotropic materials are a stack of two woven laminated composites, a E-glass/vinylester plain weave composite and a carbon/bakelite twill weave composite. The properties selected are estimates from the MESOTEX analytic method presented in [3] and are listed in Table 4.6. Figure

4.11 shows the calculated components of the stiffness tensor against the volume fraction of the E-Glass/vinylester composite, and Figure 4.12 shows the error as compared to the true solution. Interestingly, the error on this study is much lower than the other two studies. Regardless, the same trends appear as in the previous two studies. The ASE performs the worst overall by either overpredicting or undulating around the solution. The B-MVE improves upon the solution from the ASE slightly while being close to exact for the stiffness terms not associated with the material discontinuity that occurs in x_1 .

The results from the TMC-MVE are quite reasonable except for a slight overprediction on C_{1313} and C_{1212} . However, unlike in the other studies, the TMC-MVE does not underpredict C_{1122} and C_{1133} ; the error for these terms hover around 10^{-4} . The STC-MVE's performance is similar to the TMC-MVE, with the exception of the C_{1313} and C_{1212} terms; the STC-MVE yields a result that is accurate to the fourth significant digit.

Table 4.6: The properties of the two orthotropic materials (E-glass/vinylester composite and carbon/bakelite composite) used in this study, from [3]

		Material 1 (E-glass/Vinylester)	Material 2 (Carbon/Bakelite)
E_{11}	(GPa)	25.33	46.11
$E_{22} = E_{33}$	(GPa)	13.46	8.18
$G_{12} = G_{13}$	(GPa)	5.24	3.09
G_{23}	(GPa)	5.19	3.33
$\nu_{12} = \nu_{13}$		0.29	0.44
ν_{23}		0.12	0.042

Table 4.7, the percent integral absolute error for the full cube study, further confirms the reduced error in the newly proposed element STC-MVE, with all terms

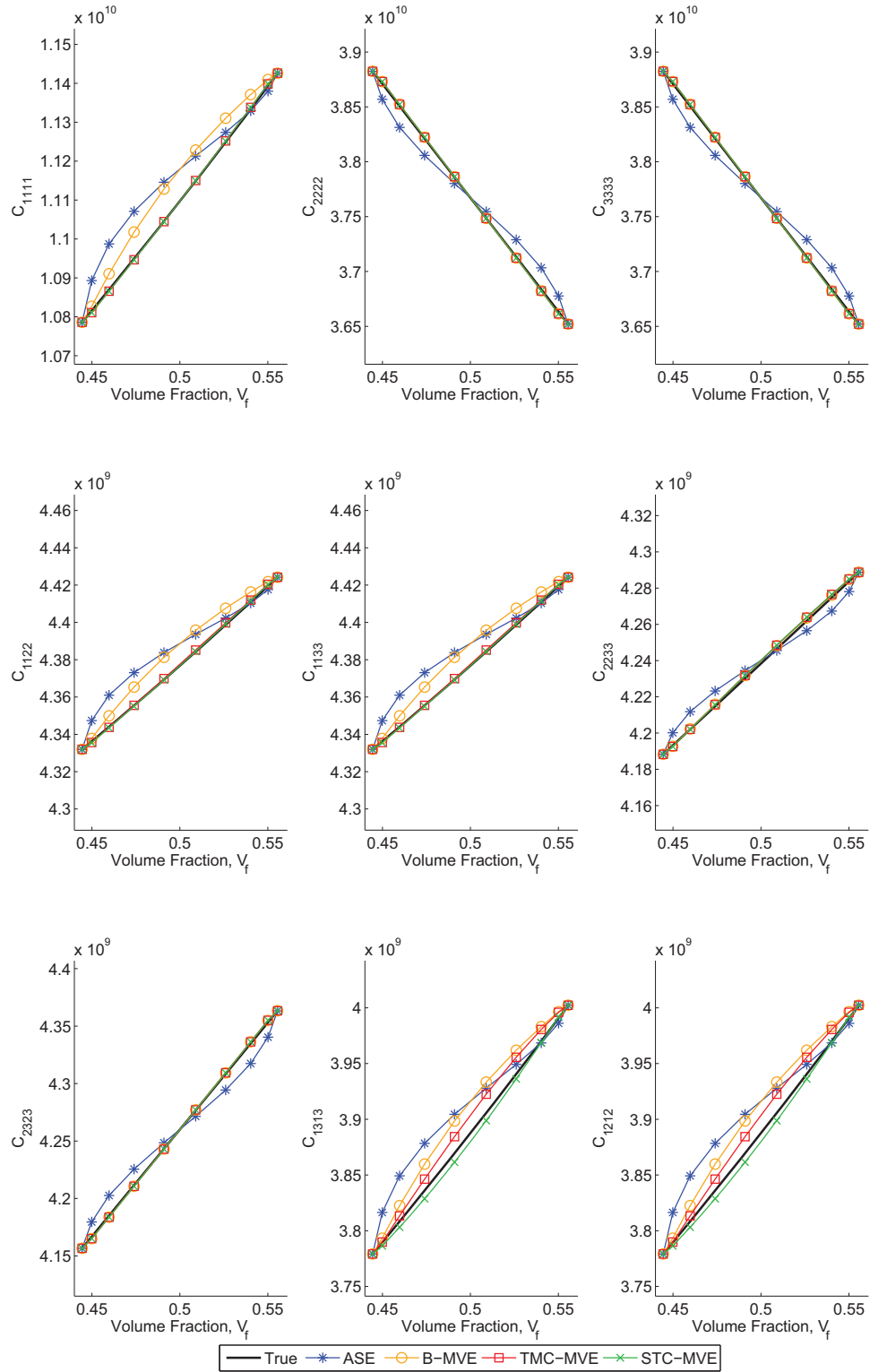


Figure 4.11: The values of the stiffness tensor C_{ijkl} vs. volume fraction (V_f) for the two orthotropic material system

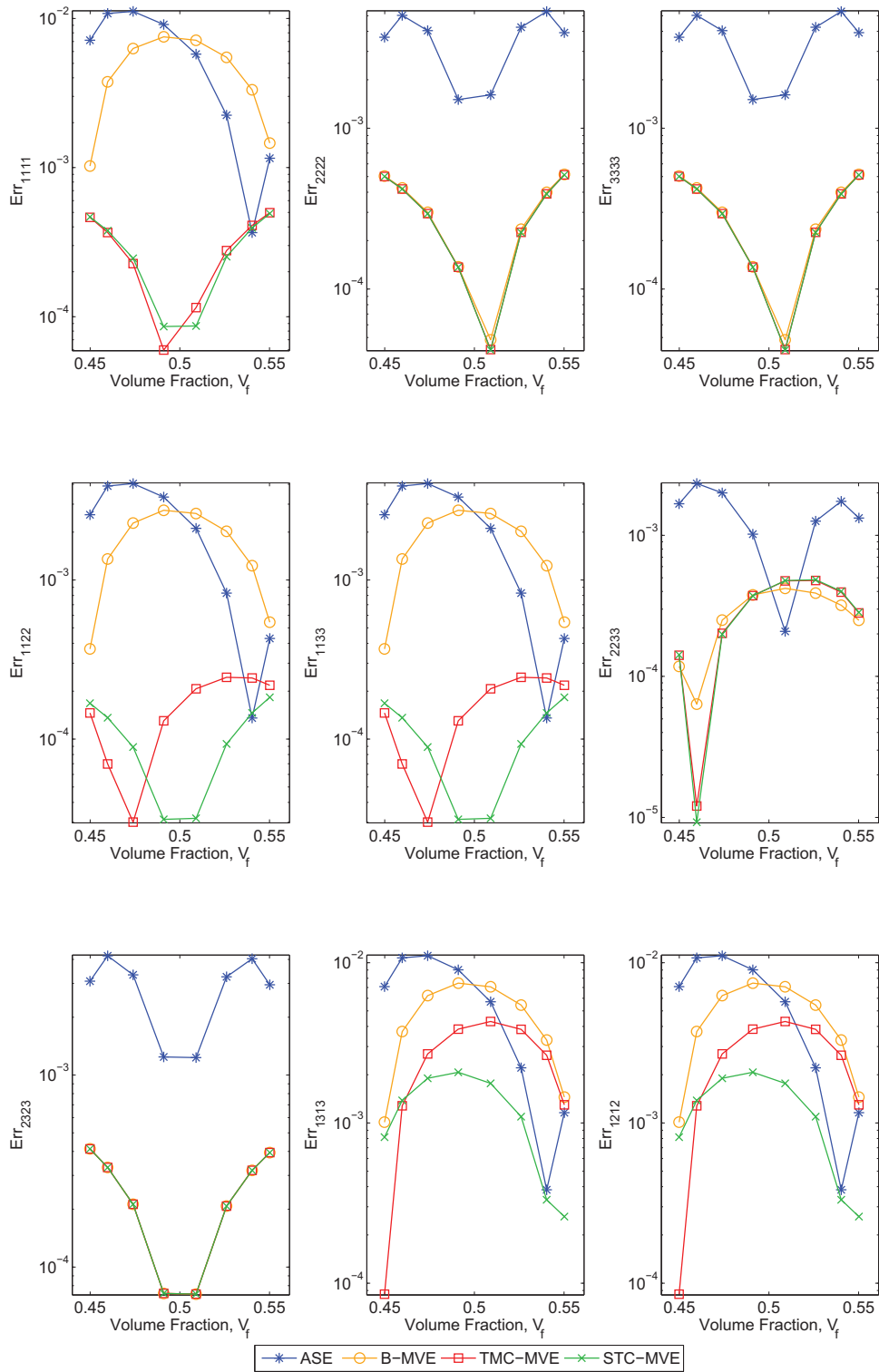


Figure 4.12: The error of the stiffness tensor Err_{ijkl} vs. volume fraction (V_f) for the two orthotropic material system, calculated using Equation (4.29)

having an error less than 1% error. While it is difficult to draw any useful conclusions when all of the elements performed well, it can be noted that the ASE still performs worst overall and the newly presented TMC–MVE and newly presented STC–MVE both perform the best.

Table 4.7: The percent integral absolute error for the orthotropic study, calculated using Equation (4.30)

(%)	ASE	B–MVE	TMC–MVE	STC–MVE
e_{1111}	0.63	0.50	0.20	0.20
e_{2222}	0.37	0.21	0.21	0.21
e_{3333}	0.37	0.21	0.21	0.21
e_{1122}	0.23	0.19	0.07	0.07
e_{1133}	0.23	0.19	0.07	0.07
e_{2233}	0.14	0.08	0.08	0.08
e_{2323}	0.29	0.16	0.16	0.16
e_{1313}	0.62	0.50	0.30	0.22
e_{1212}	0.62	0.50	0.30	0.22

As done with the transversely isotropic and isotropic study, comparing this study to the previous two studies may suggest there is a correlation between the ratio of the two sets of constituent material properties and the accuracy of the MVE. For example, in Table 4.6, E_{11} for the constituent materials used in the orthotropic study differed by a factor of 2; the error for C_{1111} in Table 4.7 ranged from 0.20% \sim 0.63%. In Table 4.2, E for the constituent materials used in the isotropic study differed by a factor of 5.5 and the error for C_{1111} in Table 4.3 ranged from 0.55% \sim 4.12%. Finally, in Table 4.4, E_{11} for the constituent materials used in the isotropic/transversely isotropic study differed by a factor of 17; the error for C_{1111} in Table 4.5 ranged from 0.97% \sim 10.83%. This suggests in general that an increase in ratio between two

sets of material properties correlates to an increase in error in the stiffness properties calculated by the MVEs.

4.4 Material Angle Study

Isotropic materials have an infinite number of planes of symmetry, so they are invariant to rotation. Transversely isotropic materials, such as strands from a laminated composite, are variant to rotation. This property of a nonisotropic material can adversely affect the performance of the MVE; therefore, a test was developed to determine the effect of material rotation on the accuracy of the MVE. This test was performed using custom finite element code written in MATLAB.

4.4.1 Description of Test Method

Figure 4.13 visually demonstrates how this test was performed. Using the two-material unit cube from the volume fraction test, an isotropic material and a transversely isotropic material are placed side-by-side, each composing half of a unit cube. The isotropic material remains unchanged throughout the test, but the transversely isotropic material is rotated from the principal frame to a number of local coordinate frames. The material properties of the cube are then evaluated and plotted.

Figure 4.14 shows how the property rotation is performed (see e.g., [78]). A stiffness tensor in the local principal direction of the fiber C'_{ijkl} is rotated into the global frame using the rotation tensor $\mathbf{Q}(\theta, \phi)$, defined as

$$\mathbf{Q}(\theta, \phi) = \begin{bmatrix} \sin \theta \cos \phi & \sin \theta \sin \phi & \cos \theta \\ -\sin \phi & \cos \phi & 0 \\ -\cos \theta \cos \phi & -\cos \theta \sin \phi & \sin \theta \end{bmatrix} \quad (4.34)$$

where θ is the angle from the positive x_3 axis, and ϕ is the angle measured from the positive x_1 axis about the x_3 axis in the x_1 - x_2 plane. The rotation tensor in Equation (4.34) is used to obtain the global stiffness tensor C_{ijkl} from the local principal stiffness

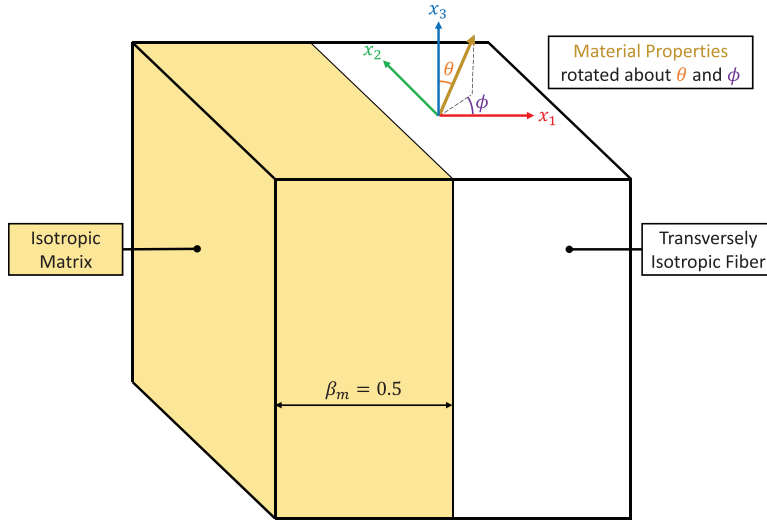


Figure 4.13: The material angle study

tensor C'_{ijkl} through a series of summations as

$$C_{ijkl} = Q_{ip}(\theta, \phi)Q_{jq}(\theta, \phi)Q_{kr}(\theta, \phi)Q_{ls}(\theta, \phi)C'_{pqrs} \quad (4.35)$$

This global stiffness tensor C_{ijkl} is what is used in the Gauss point integration and where the corrections for the TMC–MVE and STC–MVE are derived from.

The values of the angles tested were a 15×15 grid of equally spaced points spanning $0 \leq \theta \leq \frac{\pi}{2}$ and $0 \leq \phi \leq \frac{\pi}{2}$. While this does not cover the full hemisphere needed to fully test this method, this choice only affects the anisotropic terms in the stiffness tensor; the nine orthotropic terms being studied are symmetric about $\theta = \frac{\pi}{2}$ and $\phi = \frac{\pi}{2}$.

The mesh of the cube is the same as for the volume fraction study, with $10 \times 10 \times 10$ elements for the true solution and $9 \times 9 \times 9$ for the MVE mesh, with 9 integration points in each dimension within each element. The material properties used come from Table 4.4, the material properties from the isotropic/transversely isotropic volume fraction study, and the volume fraction was set to $V_f = 0.5$.

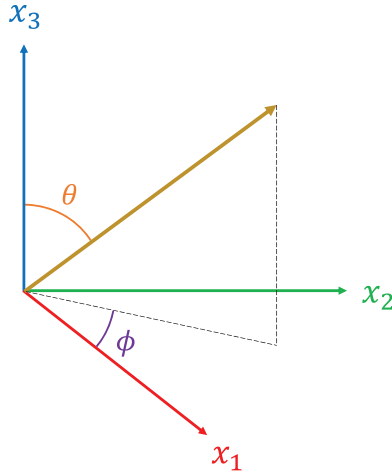


Figure 4.14: The definitions of θ and ϕ , which define the coordinate system which material properties are rotated to.

The error calculation e_{ijkl} is similar to the calculation made in Equation (4.30), but is not exactly the same. A double integration is required to determine the percent integral absolute error, as C_{ijkl} is now dependent on two variables instead of just one.

$$e_{ijkl} = \int_0^{\frac{\pi}{2}} \int_0^{\frac{\pi}{2}} \left| \frac{C_{ijkl}^{\text{true}}(\theta, \phi) - C_{ijkl}^{\text{MVE}}(\theta, \phi)}{C_{ijkl}^{\text{true}}(\theta, \phi)} \right| d\phi d\theta \quad (4.36)$$

4.4.2 Results

Figure 4.15 plots a surface with the calculated values of the material stiffness tensor at each θ and ϕ , and Figure 4.16 plots the error against the true solution, as found from Equation (4.29). While the nature of the surface plots make it difficult to analyze, a few useful trends are noticed. From Figure 4.15, all of the MVEs appear to at least follow the trend of the true solution; although, often, the MVEs are shifted in some fashion vertically from the true solution. A notable exception is the prediction of C_{1313} and C_{1212} for the TMC-MVE. Interestingly, the slope of the surface as it changes in θ at $\phi = 0$ is much steeper than the other elements. Overall, it appears

the TMC–MVE and the STC–MVE have the lowest overall error, but it is hard to tell from Figures 4.15 and 4.16.

Table 4.8: The percent integral absolute error for the material angle study, calculated using Equation (4.36)

(%)	ASE	B–MVE	TMC–MVE	STC–MVE
e_{1111}	10.44	9.96	1.87	2.08
e_{2222}	1.10	1.58	1.99	1.98
e_{3333}	1.09	1.61	1.87	1.86
e_{1122}	6.95	6.65	1.78	0.95
e_{1133}	6.41	6.13	1.77	0.98
e_{2233}	0.82	0.72	1.67	1.61
e_{2323}	1.46	2.19	2.16	2.18
e_{1313}	13.12	12.65	10.45	8.37
e_{1212}	13.82	13.35	12.02	8.86
e_{2313}	33.21	31.79	35.83	17.28

Table 4.8 shows the percent integral absolute error, as calculated by Equation (4.36). The ASE again has the highest error overall, but does not have the highest error in all cases. In fact, the ASE is the most accurate method for calculating C_{2222} , C_{3333} , and C_{2323} for this study. The B–MVE provides slight improvements on the ASE for some of the terms, but degrades in accuracy on the C_{2222} , C_{3333} , and C_{2323} terms. These terms only generate equivalent or slightly higher error for the TMC–MVE and STC–MVE, but these two come with the benefit of having a much improved accuracy on C_{1111} (a drop from about 10% to about 2%). While the TMC–MVE performs the best on C_{1111} , the STC–MVE has the best overall performance, being the only element with an error less than 10% on C_{1313} and C_{1212} terms. All other terms for the STC–MVE have an error of 2.2% or below (similar to the TMC–MVE).

This test proved to be more rigorous for the MVEs as the test introduced some anisotropic behavior. The last row of Table 4.8 provides the error calculation one of

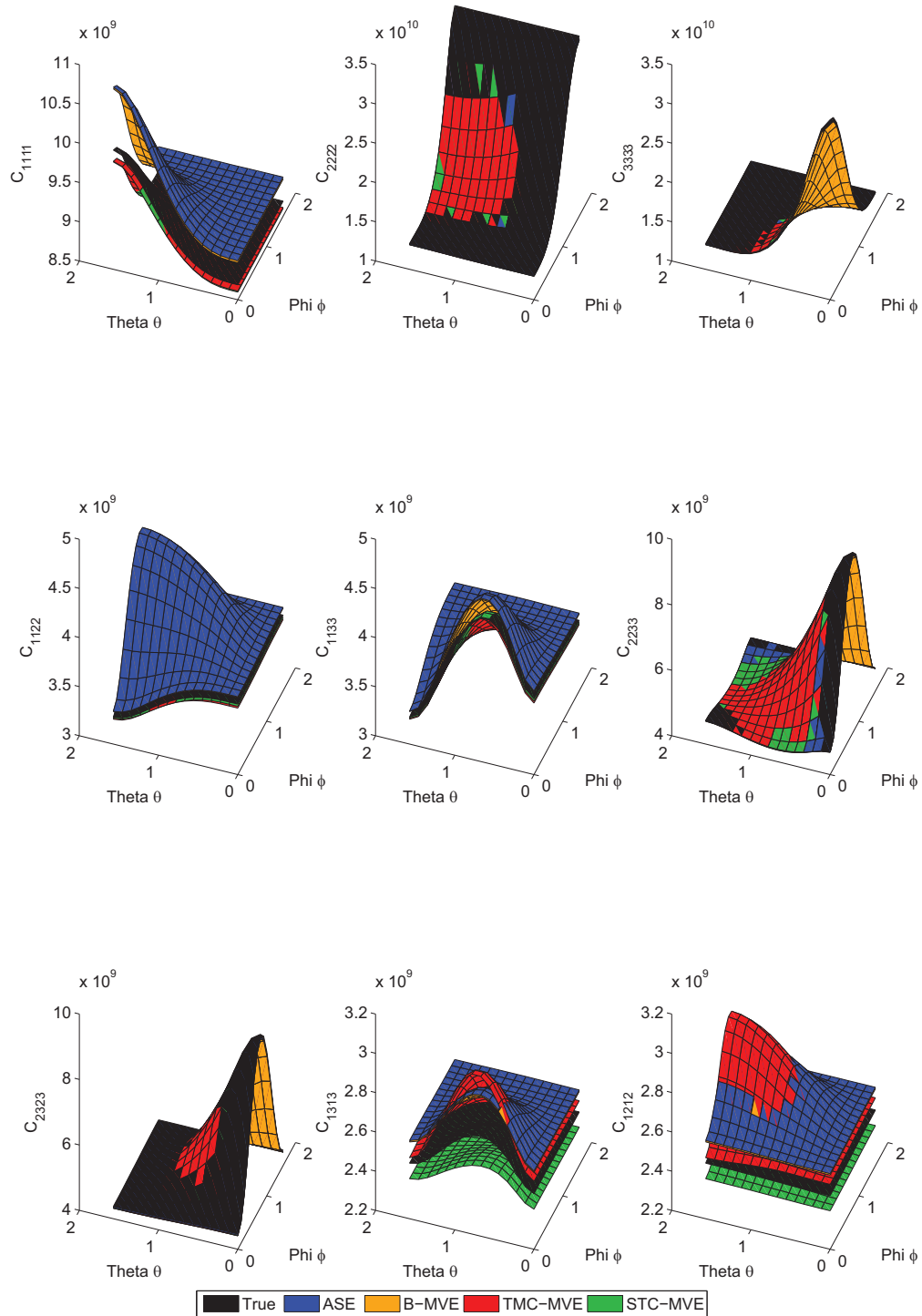


Figure 4.15: The values of the stiffness tensor C_{ijkl} vs. material rotation angles θ and ϕ

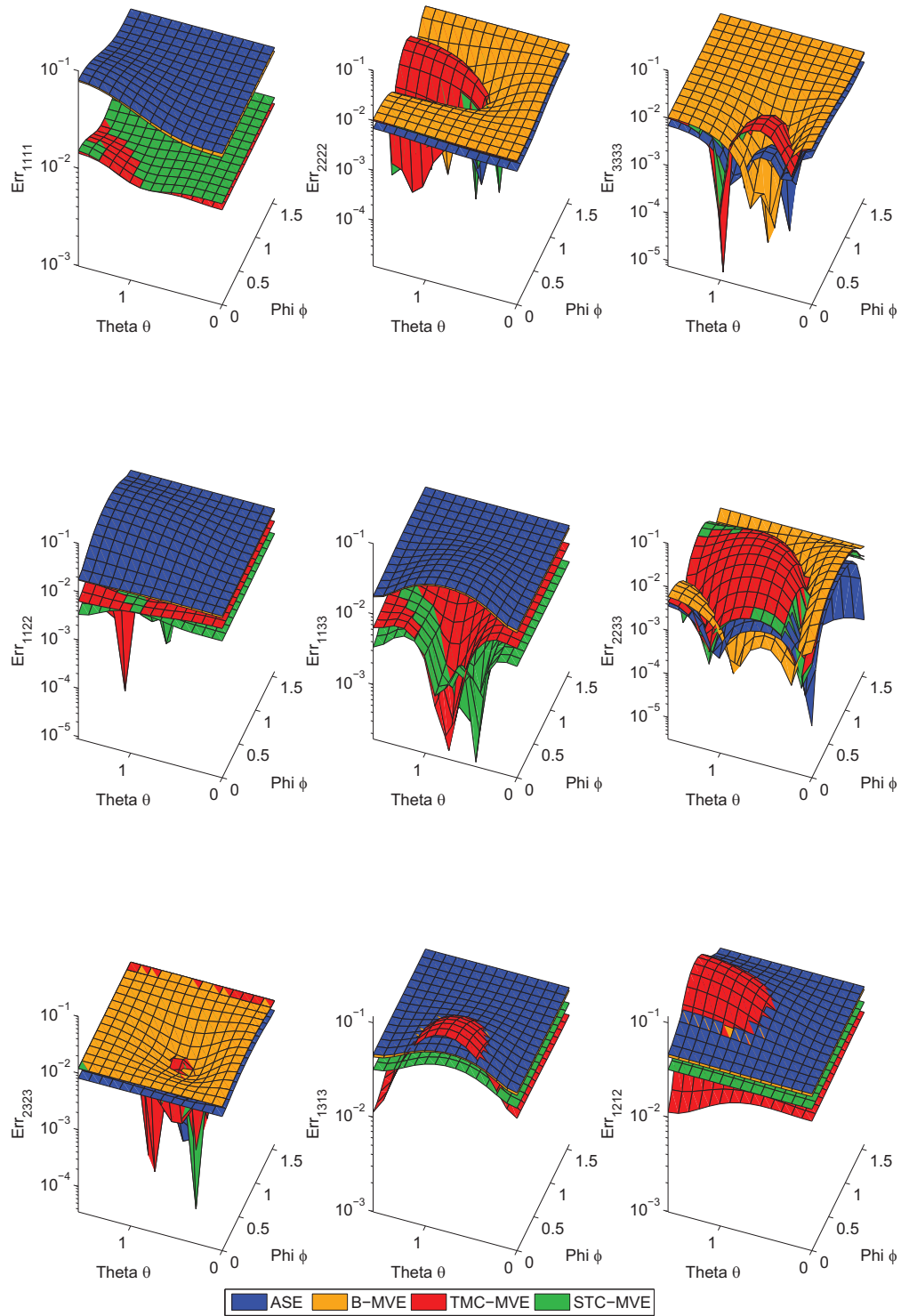


Figure 4.16: The error of the stiffness tensor Err_{ijkl} vs. material rotation angles θ and ϕ , calculated using Equation (4.29)

these anisotropic terms, C_{2313} . The actual values for this stiffness component is at a maximum on the order of 10^8 Pa, as opposed to 10^9 Pa for the nine orthotropic terms. Because the value of this component is zero for certain conditions, the calculation can sometimes result in minute inaccuracies at the machine-precision level, which can cause spikes in the error calculation in Equation (4.36). To prevent this, the values of C_{2313} were truncated at 10^5 before calculating the error.

The error for this anisotropic stiffness component is fairly high in comparison to the other stiffness tensor components. This is because not all stiffness tensor components are accounted for in the calculation of strain corrections of the applicable MVEs. Future work is required to incorporate more terms of the stiffness tensor in the calculation of each MVE.

Outside of the shear terms C_{1313} and C_{1212} , the TMC-MVE and STC-MVE maintained overall a low error from the true solution.

4.5 Boundary Angle Study

The previous studies had a cube with a boundary that was parallel to the x_2 - x_3 plane, which will not be the case when working with complex geometries such as woven composites. Sometimes, the material boundaries will be at oblique angles, which may adversely affect the accuracy of the MVEs. This study tests the accuracy of each MVE when the material boundary changes angles. Further, a study on how the number of Gauss points used affects accuracy will be performed.

4.5.1 Description of Test Method

Figure 4.17 depicts a representation of the geometry used for this study. The boundary between Material 1 and Material 2 is a sideways chevron, which is done to keep the geometry periodic (i.e., so the boundaries on the top and bottom line up with each other). The boundary line therefore consists of two parts, an upper and

a lower part, that each “pivot” about the black points marked in Figure 4.17. The angle θ is measured from the positive x_1 axis to the lower boundary portion; this angle θ has the same magnitude as the angle between the top edge and the upper boundary.

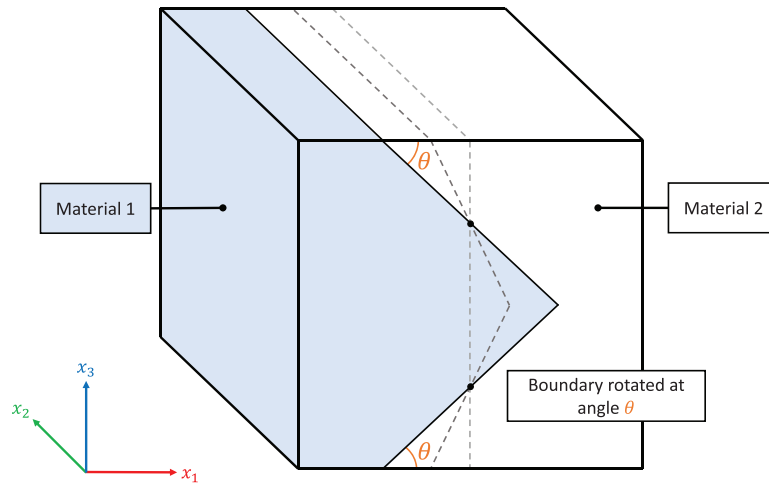


Figure 4.17: The boundary angle study

The material properties for this study are the same isotropic properties found in Table 4.2. The range of the angle θ was chosen to be $\frac{\pi}{6} \leq \theta \leq \frac{5\pi}{6}$ radians, or $30^\circ \leq \theta \leq 150^\circ$. This is about the maximum range of θ before the boundary collides with the left- or right-most edge of the geometry.

The mesh of the cube is $9 \times 9 \times 9$ for the MVE mesh, with 9 Gauss points in each dimension, just as the previous two studies. The mesh for the true solution is shown in Figure 4.18. Due to the more complex nature of the geometry, the study for the true solution was performed in commercial finite element software (COMSOL Multiphysics 5.2) instead of MATLAB. However, the MVE solutions are still computed using custom finite element code in MATLAB.

For the Gauss point study, the angled boundary cube in Figure 4.17 with a boundary angle of 60° is used. The cube is analyzed using the MVEs with the number

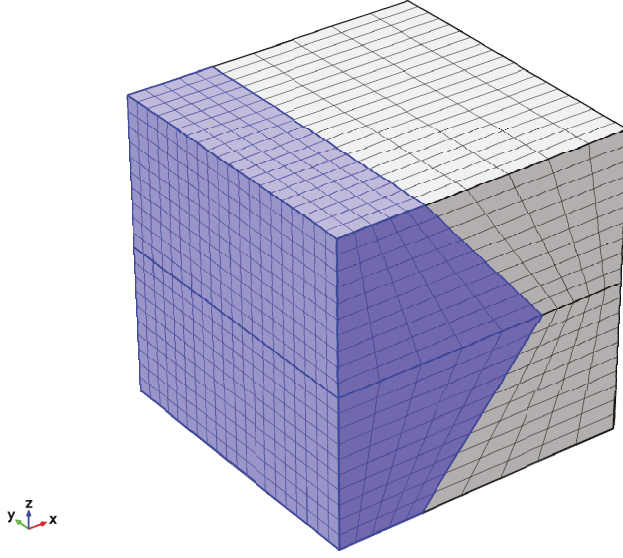


Figure 4.18: The mesh for the true solution to boundary angle study for $\theta = 50^\circ$

of Gauss points $N_{gp} \in \{1, 2, \dots, 10\}$. The relative error is calculated and plotted as a function of the number of Gauss points; this error can be calculated as

$$\text{Rel Err}_{ijkl}(N_{gp}) \equiv \left| \frac{C_{ijkl}^{\text{MVE}}(10) - C_{ijkl}^{\text{MVE}}(N_{gp})}{C_{ijkl}^{\text{MVE}}(N_{gp})} \right| \quad (4.37)$$

The integral absolute error calculation e_{ijkl} is similar to the calculation made in Equation (4.30), but is calculated over the angle of the planes in Figure 4.17 as

$$e_{ijkl} = \int_{\frac{\pi}{6}}^{\frac{5\pi}{6}} \left| \frac{C_{ijkl}^{\text{true}}(\theta) - C_{ijkl}^{\text{MVE}}(\theta)}{C_{ijkl}^{\text{true}}(\theta)} \right| d\theta \quad (4.38)$$

4.5.2 Results – Gauss Point Study

Figure 4.19 shows the relative error of each MVE as calculated in Equation (4.37) against the number of Gauss points used within each MVE. The purpose of this study is to determine the number of Gauss points required for a converged solution.

As shown in the figure, for all of the MVEs, the relative error is below the 1% line (the dashed-dotted line) by around three or four Gauss points. Even though

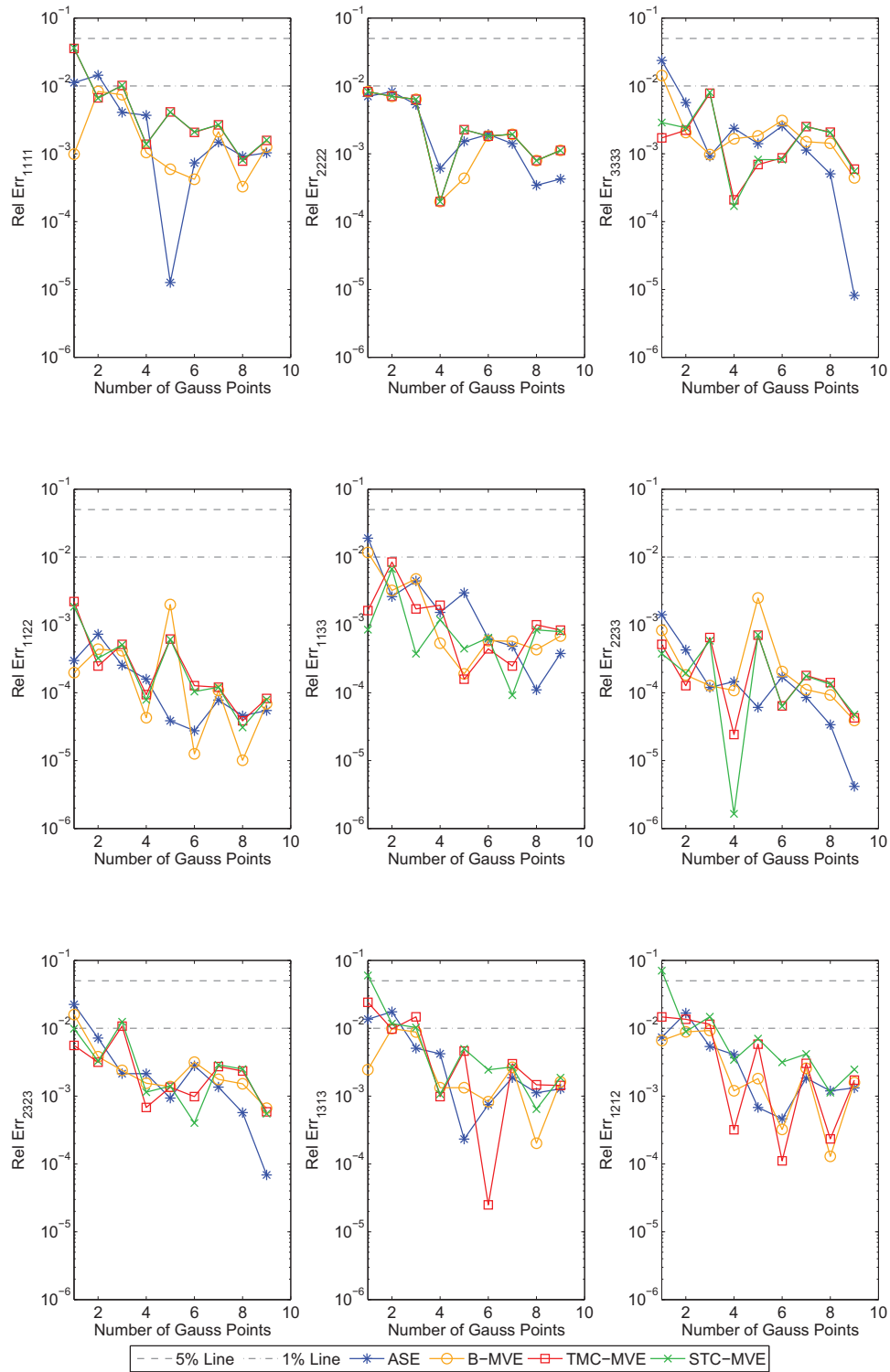


Figure 4.19: The relative error of the MVEs versus the number of Gauss points. The dashed line represents 5% error, and the dashed-dotted line represents 1% error.

the solution still fluctuates some past this, it stays within 1% of the 10 Gauss point solution.

An interesting phenomenon occurs as the solution is calculated for an even and odd number of Gauss points. It appears that an odd number of Gauss points generates a much higher error than the even numbered counterparts. It is unknown why this occurs; it may be a function of the geometry tested. To prevent this type of response in the future, an adaptive quadrature scheme can be used to force integration points to areas where more refinement is required (i.e., at material boundaries).

Regardless of this odd phenomenon, the solution is converged by four Gauss points, so the use of nine Gauss points in these studies is justified.

4.5.3 Results – Boundary Angle Study

Figure 4.20 shows the calculated stiffness tensor components as a function of the angle of the material boundary θ in degrees. Figure 4.21 shows the error from the true solution as calculated by Equation (4.29).

One thing that is apparent right away is the symmetry of the solution; the geometry is symmetric about 90° , so the results are expected to be symmetric as well. Another thing that is apparent is the large error in all of the MVEs studied for the shear stiffness terms C_{1313} and C_{1212} ; in Figure 4.21, these terms show error consistently in excess of 10^{-1} , or 10%. From previous studies, it is understood these terms will have the highest error, but the error is much larger in this study than in previous studies.

Except for C_{1313} , the MVE results tend to follow the trend of the true solution very well. The accuracy of each MVE is more so affected by a vertical shift up or down from the true solution. Similar to the previous studies, the TMC–MVE and STC–MVE remain the most accurate, with the STC–MVE having the lowest error on

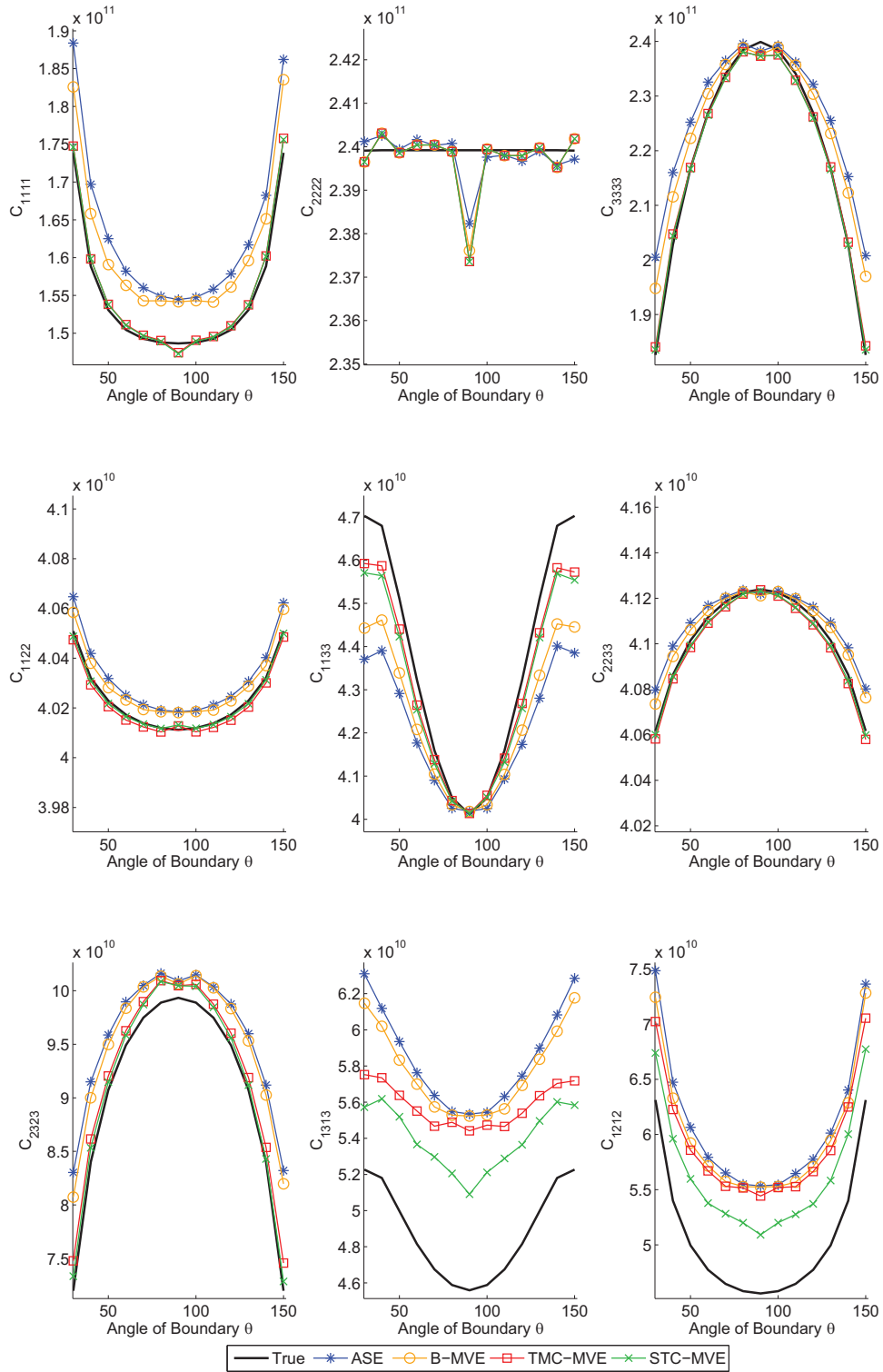


Figure 4.20: The values of the stiffness tensor C_{ijkl} vs. the boundary angle θ

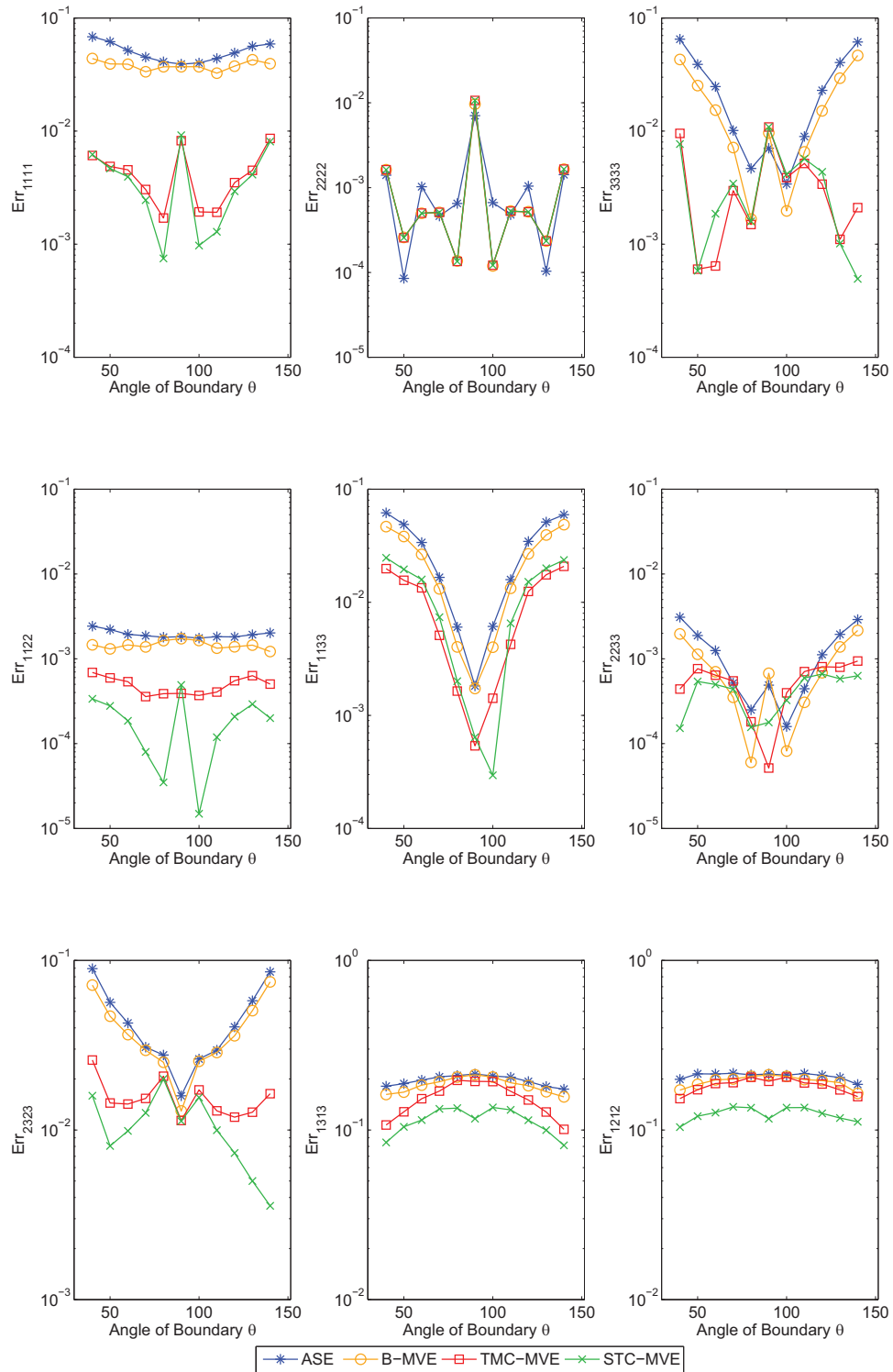


Figure 4.21: The error of the stiffness tensor Err_{ijkl} vs. the boundary angle θ , calculated using Equation (4.29)

the C_{1313} and C_{1212} terms. The MVEs, in most cases, follow the trend of the stiffness terms fairly well; inaccuracies draw from either being vertically shifted from the true solution (see the ASE and B-MVE on C_{1111}) or having gradually increasing error as the angle drifts from 90° (see all elements on C_{1133}).

Interestingly, on the C_{2222} term, all of the MVEs drop dramatically in value right at the 90° mark. This can be seen in the other terms as well, to a lesser extent. The reason for this is that, at 90° , the material boundary is directly vertical and on top of a Gauss point. This is the worst case performance for the MVE: when the boundary is right on top of the integration point. This causes a miscalculation in the properties because both sets of material properties exist at that point, so just using one set will produce an inaccurate result.

Table 4.9: The percent integral absolute error for the boundary angle study, calculated using Equation (4.38)

(%)	ASE	B-MVE	TMC-MVE	STC-MVE
e_{1111}	11.03	8.23	0.99	0.90
e_{2222}	0.27	0.29	0.31	0.31
e_{3333}	6.74	4.79	0.88	0.82
e_{1122}	0.43	0.31	0.11	0.05
e_{1133}	7.07	5.54	2.41	2.89
e_{2233}	0.32	0.22	0.12	0.09
e_{2323}	11.48	9.91	3.68	2.35
e_{1313}	41.19	38.45	31.16	22.99
e_{1212}	43.10	39.77	37.13	25.06

As alluded to in the previous tests, C_{1313} and C_{1212} are the terms calculated with the highest error. This is demonstrated also in Table 4.9, which calculates the percent integral absolute error defined in Equation (4.38). For these shear stiffness terms, the error is significantly higher than for the other terms. For example, the TMC-MVE has error on the order of 1%–2% for most of the terms which then jumps

to around 35% for these shear stiffness terms. As expected, the STC–MVE predicts these two terms with the lowest error, but this error is still on the order of 25%.

4.6 Overall Conclusions

In all tests performed, the TMC–MVE and STC–MVE performed about the same on most of the stiffness terms, but the STC–MVE consistently has the best performance across the board, specifically the shear stiffness terms C_{1313} and C_{1212} . This is most likely attributed to how this element handles the correction on the shear stiffness terms. Further, the STC–MVE uses the stiffness tensor terms directly in calculating the strain corrections (unlike the TMC–MVE, which only uses the tensile moduli).

Despite the improved accuracy of the STC–MVE on these shear terms, the calculation of these terms could still be improved. The way the STC–MVE handles the calculation of the strain corrections for the shear stiffness terms is a step in the correct direction, but more research into alternate methods should be performed to further decrease this error. Of specific improvement would be to include extension–extension coupling and shear–extension coupling to the corrections, something that is neglected in the present formulation.

From the volume fraction studies, it is hypothesized the accuracy of the MVEs are most directly related to the magnitude of separation between the material properties present within the element. The orthotropic study had the most accurate performances of the MVEs overall, but this may be attributed to the relative magnitudes of the stiffness in the two materials being much closer than for the first set of studies. The isotropic/transversely isotropic study had the greatest error; the material properties spanned a larger magnitude for this study.

CHAPTER FIVE

Analysis of Woven Composites using Multiphase Voxel Elements

With the multiphase voxel elements (MVEs) fully developed and tested, they can now be applied to the finite element analysis (FEA) of a representative volume element (RVE) of various woven composite laminae. In this chapter, the structure of the MATLAB code for the analysis of woven composite laminae will be introduced, and results will be presented for several types of laminae: a plain weave, a satin weave, and a twill weave. Special emphasis will be given to the plain weave to validate the approach proposed in this thesis due to the wide availability of results, both experimental and computational, in the literature. The results of a satin-weave composite and twill weave composite are presented, and results are in reasonable agreement with those available in literature.

5.1 Structure of MATLAB Code

The finite element analysis for these studies were performed in the MATLAB coding environment; this was done to better implement the use of custom elements. Figure 5.1 shows a flowchart detailing the general structure of the MATLAB code used in the following analyses. There are four sets of tasks: an initialization stage, an assembly and solver stage, the elemental construction function, and the geometrical construction function. An input tab-delimited DAT file is generated first; this input file contains information about the mesh used (i.e., the global nodal locations and the element connectivity), the boundary conditions, and information about the composite laminae such as the constituent material properties and the weave type. This input file is imported into the initialization file, which reads the information contained in the input file and stores that information in the appropriate variables.

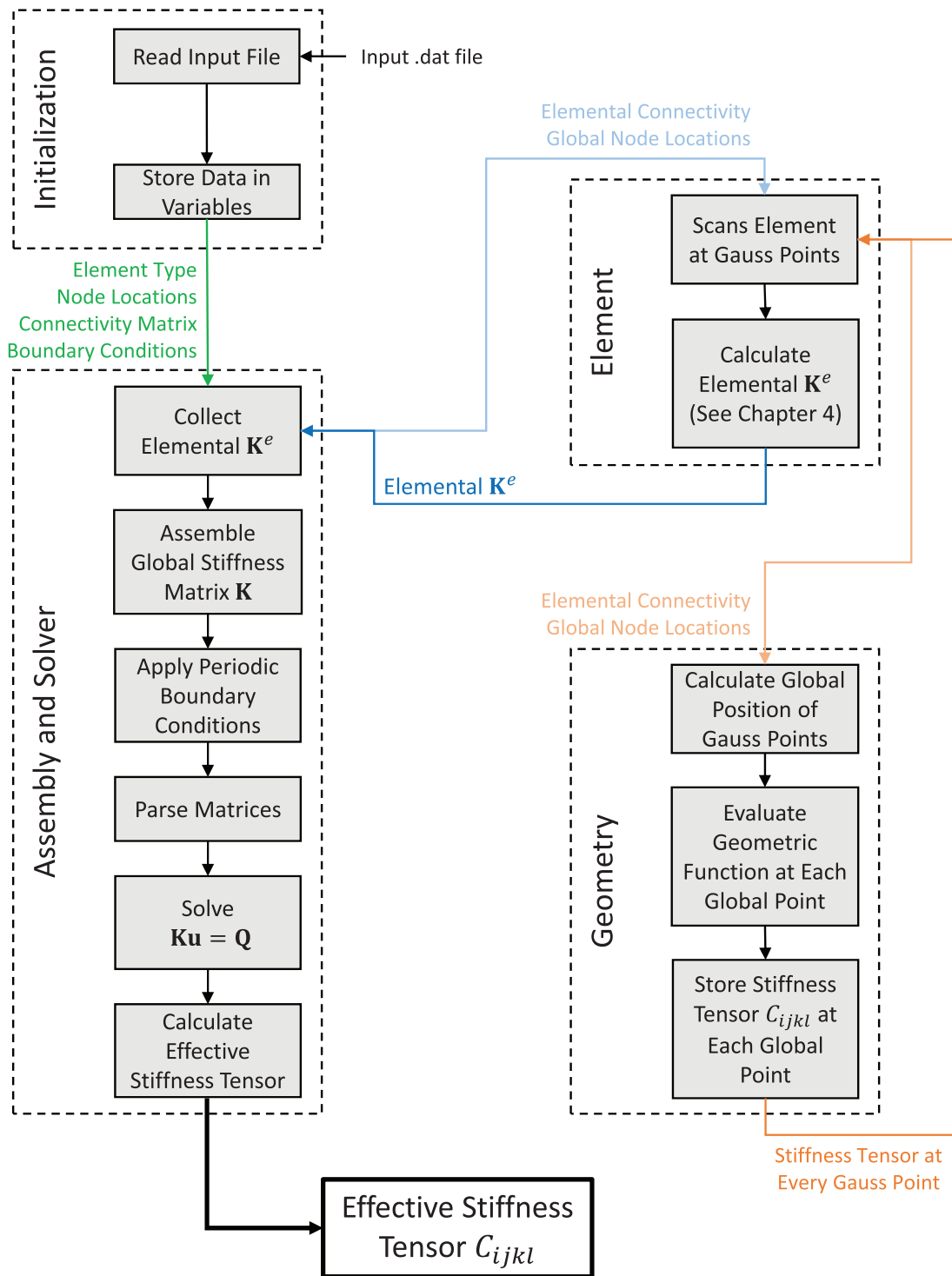


Figure 5.1: The structure of the MATLAB code used in the finite element analyses performed with MVEs

The variables generated in the initialization file are then passed to the assembly and solver file. This assembly and solver file acts as the “master” file which handles most of the information and calculation. First, it collects the elemental stiffnesses \mathbf{K}^e from the elemental file, as calculated in general in Equation (3.27). Once all the elemental stiffnesses have been calculated, the assembly and solver file assembles the global stiffness matrix \mathbf{K} , as presented in Equation (3.51). After the full global stiffness matrix is formed, the periodic boundary conditions are applied as described in Equation (3.62). With this reduced \mathbf{K} matrix, the system is parsed as in Equation (3.64) and the unknown global displacements \mathbf{u} and the global reaction forced \mathbf{Q} are calculated. Using the \mathbf{Q} matrix from all six strain states, the effective stiffness tensor C_{ijkl} for the geometry is calculated as in Equation (3.75).

There are four separate element files, one for each of the four MVEs presented in Chapter Four (ASE, B-MVE, TMC-MVE, and STC-MVE); the element file used is selected in the input file at the beginning of the analysis. Each MVE has its own element file, but the general structure of the inputs and outputs of the code is the same. The selected element method file “scans” the domain of the element at each individual Gauss point and determines the material located at that Gauss point via a geometry file. The spatially varying anisotropic stiffness tensor for that material is returned, along with, in the case of the fiber strands, the rotations of the stiffness tensor cause by the tow undulation. With this information, the MVEs can be calculated as presented in Chapter Four to calculate the elemental stiffness matrix \mathbf{K}^e for that element. Example MATLAB code for the element file of each of the MVEs is provided in the appendices.

The geometry file uses the global node locations provided by the element file to determine the material at that point via the use of the appropriate geometric

function. It evaluates the function at the input integration point, determines the material using a set of piecewise relations, and then stores the appropriate reduced stiffness tensor into a data structure. This data structure contains the stiffness tensor at every individual Gauss point within the element, which is necessary to calculate the strain corrections for the TMC–MVE and the STC–MVE.

In Chapter Four Section 4.5.2, it was determined that for the boundary angle study, four Gauss points in each direction was needed to have a converged solution. Because a woven composite is more complex than the boundary angle model, a higher resolution of Gauss points will be chosen. To increase resolution within the element, eight Gauss points in each of the three dimensions, as opposed to two or three for most standard finite element analyses, is selected to be used. This choice does cause the code to become computationally expensive, but this is offset by less user time required to mesh the domain. The loop that contains the evaluation of the elemental file is unique for each element, thus this loop is parallelized using the `parfor` option in MATLAB. To further optimize the computational resources, the element files are generated as MEX functions [79], which converts the MATLAB code to a C or C++ format and wraps it in a format that MATLAB can read.

5.2 Analysis of a Plain Weave Composite Lamina

After over 100 pages of background information, upper–level math, and multiple analyses of cubes, we have finally reached the part where the material properties of a woven composite lamina is calculated using multiphase voxel elements, just as it is promised in the title of this thesis. If the reader has made it this far, the author would like to note that he admires his or her tenacity and determination.

To determine the accuracy of the MVEs presented in practical applications, a plain weave composite lamina is analyzed. A picture of carbon fiber plain weave

fabric is shown in Figure 5.2. Plain weave composite laminae are one of the simplest weave types, having both the smallest RVE of all woven geometries investigated in this research and a simple geometry that is estimated in this study with sinusoidal functions. Due to their simplicity and common use in industry, they are often chosen as the first set of laminae tested for a new mesomechanical model (see e.g., [36]). Further, plain weave fabrics are easier to drape than unidirectional fabrics, so they are often used for parts with complex curvature, and they have a high degree of stability so they will not unravel as easily (see e.g., [80]). Example applications extend from hobbyist applications, such as the spoiler of a car, to structural applications, such as an airplane wing, to acoustic applications, such as a cello bow.

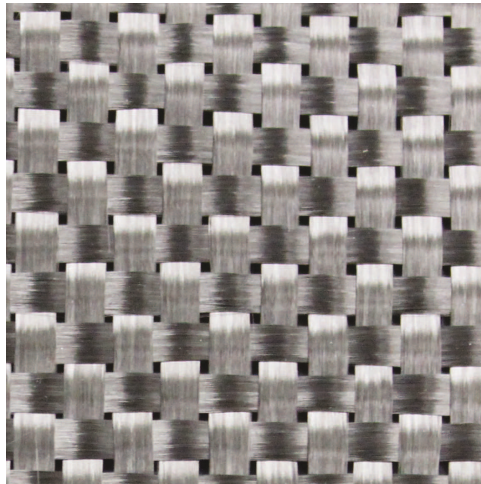


Figure 5.2: A picture of carbon fiber plain weave fabric

For the analysis, the geometry is evaluated with traditional finite elements using the commercial code COMSOL Multiphysics, and with MVEs in the MATLAB code detailed in Section 5.1. The stiffness tensor components calculated are compared to each other and to experimental results from Scida *et al.* [3] to demonstrate accuracy. A convergence study to determine the number of elements required to achieve acceptable accuracy levels is also presented. From the results shown in

the following section, the accuracy of the MVE method is equal to that of traditional finite element approaches, and also aligns nicely with the experimental results.

5.2.1 Geometry

In order to analyze the RVE of a woven composite lamina, its geometry must first be defined. For this study (as well as the studies that follow), the geometry is defined using analytic functions. Figure 5.3 shows top and side views of the plain weave composite lamina.

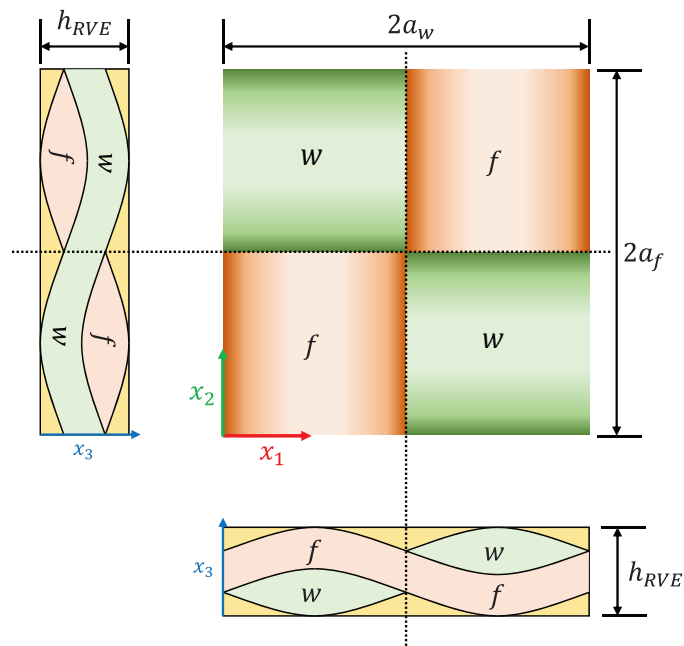


Figure 5.3: Top and side views of a plain weave composite lamina. Fill strands (f) are represented in red, and warp strands (w) are represented in green.

5.2.1.1 Geometric Functions. Figure 5.4 shows a cut-plane view of the geometry of the plain weave lamina analyzed with the geometric functions labeled. The geometric functions used were adapted from those presented in Scida *et al.* [13], who define a plain weave composite RVE with no fiber gap using sinusoidal functions for both the strand undulation and thickness. The functions were originally defined for

a quarter RVE and have been adapted to define a full RVE to allow the application of the periodic boundary conditions.

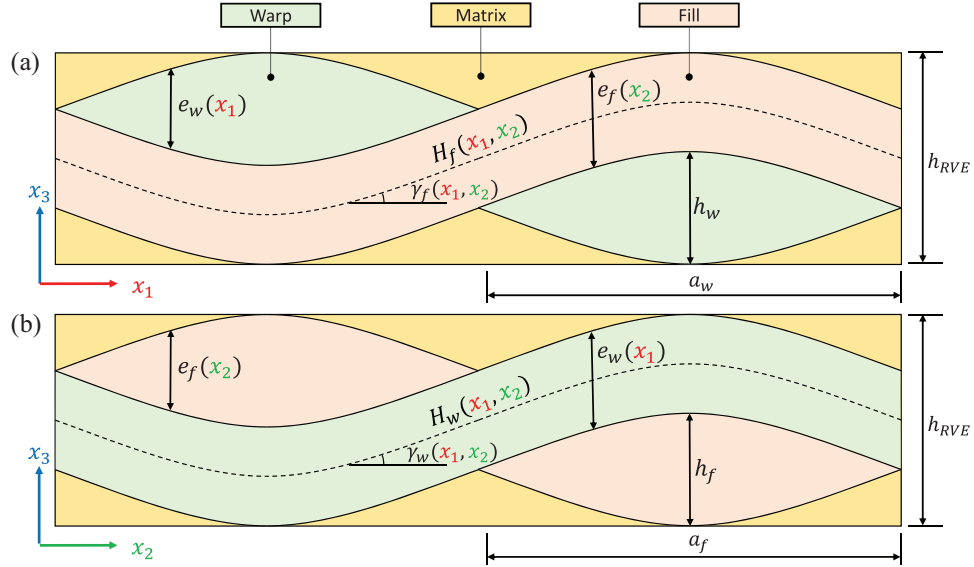


Figure 5.4: 2D cut-plane view of a plain-weave woven composite, with geometric functions labeled. (a) View along the positive x_2 -axis to highlight geometry of fill, and (b) view along the positive x_1 -axis to highlight geometry of warp

Scida *et al.* [13] originally used the functions to model composite laminae with two different types of fiber tows; therefore, the following functions will differentiate between those describing the fill strand (as denoted by the subscript f) and the warp strand (the subscript w). For the purpose of this thesis, the fill strand undulates in the x_1 direction and the warp strand undulates in the x_2 direction, with the x_3 direction being in the direction of the composite thickness.

The undulation of the fill strand through space $H_f(x_1, x_2)$ and the warp strand $H_w(x_1, x_2)$ are defined in terms of a sinusoidal function as

$$H_f(x_1, x_2) = \begin{cases} \frac{h_w}{2} \sin \frac{\pi x_1}{a_w} & 0 \leq x_2 \leq a_w \\ -\frac{h_w}{2} \sin \frac{\pi x_1}{a_w} & a_w \leq x_2 \leq 2a_w \end{cases} \quad (5.1)$$

$$H_w(x_1, x_2) = \begin{cases} -\frac{h_f}{2} \sin \frac{\pi x_2}{a_f} & 0 \leq x_1 \leq a_f \\ \frac{h_f}{2} \sin \frac{\pi x_2}{a_f} & a_f \leq x_1 \leq 2a_f \end{cases} \quad (5.2)$$

where h_f and h_w refer to the thickness of the strands, and a_f and a_w refer to the width of the strands; the domain of the RVE is defined in the region $\{0 \leq x_1 \leq 2a_w; 0 \leq x_2 \leq 2a_f; -(h_f + h_w) \leq x_3 \leq (h_f + h_w)\}$. The piecewise nature of the formulae ensure that the two sets of fill and warp strands undulate 180° out of phase with each other, as is characteristic of plain weaves. Note that while a resin pocket is sometimes included between the fill and warp strand, this case is not considered in the following studies. For the laminae studied, the full height h_{RVE} is calculated as the sum of h_f and h_w for ease of generating the reference model in COMSOL. Future studies should focus on analyzing more realistic geometries.

The functions defining the strand shape transverse to the strand direction, $e_f(x_2)$ and $e_w(x_1)$, are defined as

$$e_f(x_2) = \frac{h_f}{2} \sin \frac{\pi x_2}{a_f} \quad (5.3)$$

$$e_w(x_1) = \frac{h_w}{2} \sin \frac{\pi x_1}{a_w} \quad (5.4)$$

This set of sinusoidal functions defines the curvature on the top and bottom surface of the strand. When used in tandem with the undulation functions in Equations (5.1) and (5.2), it can be determined whether the point (x_1, x_2, x_3) is in the fill, warp, or matrix. Then the stiffness tensor of Equation at a point $C_{ijkl}(x_1, x_2, x_3)$ may be defined as either the stiffness tensor of the fill strand (C_{ijkl}^F), the warp strand (C_{ijkl}^W), or the matrix (C_{ijkl}^M). This can be done using the following piecewise relationship:

$$C_{ijkl}(x_1, x_2, x_3) = \begin{cases} C_{ijkl}^F & H_f(x_1, x_2) - e_f(x_2) \leq x_3 \leq H_f(x_1, x_2) + e_f(x_2) \\ C_{ijkl}^W & H_w(x_1, x_2) - e_w(x_2) \leq x_3 \leq H_w(x_1, x_2) + e_w(x_2) \\ C_{ijkl}^M & \text{else} \end{cases} \quad (5.5)$$

5.2.1.2 *Fiber Rotation.* As discussed in Chapter Four, because the strands are transversely isotropic materials, they are variant to rotation. Therefore, C_{ijkl}^F depends upon the angle of the local principal frame with respect to the global frame. To reiterate, the local stiffness tensor C'_{ijkl} can be rotated into the global frame as C_{ijkl} via the rotation tensor $\mathbf{Q}(\theta, \phi)$ as (see e.g., [78])

$$C_{ijkl} = Q_{ip}(\theta, \phi)Q_{jq}(\theta, \phi)Q_{kr}(\theta, \phi)Q_{ls}(\theta, \phi)C'_{pqrs} \quad (5.6)$$

where θ is the angle from the positive x_3 axis and ϕ is the angle measured from the positive x_1 axis for a rotation about the x_3 axis, and the rotation tensor is

$$\mathbf{Q}(\theta, \phi) = \begin{bmatrix} \sin \theta \cos \phi & \sin \theta \sin \phi & \cos \theta \\ -\sin \phi & \cos \phi & 0 \\ -\cos \theta \cos \phi & -\cos \theta \sin \phi & \sin \theta \end{bmatrix} \quad (5.7)$$

In the particular case of the fill and warp strands, the values of θ and ϕ are found in relation to the geometric functions presented. The value of ϕ is trivial; as the fill strand travels in the x_1 direction, the value of $\phi_f = 0^\circ$ for the entire RVE. Similarly, the warp strand travels in the x_2 direction — a $+90^\circ$ rotation from the x_1 axis — so the value of $\phi_w = \frac{\pi}{2}$ for the entire RVE.

The values of θ_f and θ_w are dependent upon the angle of the undulation at a particular point. This is defined in terms of the tangent line to the functions $H_f(x_1, x_2)$ and $H_w(x_1, x_2)$ for, respectively, the fill and the warp angles. The angles of the tangent line, denoted as $\gamma_f(x_1, x_2)$ and $\gamma_w(x_1, x_2)$ in Figure 5.4, are calculated as [13]

$$\tan \gamma_f(x_1, x_2) = \frac{\partial H_f}{\partial x_1} \quad (5.8)$$

$$\tan \gamma_w(x_1, x_2) = \frac{\partial H_w}{\partial x_2} \quad (5.9)$$

The angle γ_f is measured from the x_1 axis, and γ_w from the x_2 axis, whereas the values of θ_f and θ_w in Equation (5.6) are both measured from the x_3 axis. The values of θ_f

and θ_w can therefore be calculated from γ_f and γ_w as

$$\theta_f(x_1, x_2) = \frac{\pi}{2} - \gamma_f(x_1, x_2) \quad \theta_w(x_1, x_2) = \frac{\pi}{2} - \gamma_w(x_1, x_2) \quad (5.10)$$

With these relations, the local stiffness tensor for each transversely isotropic fiber $\mathbf{Q}(\theta_f, \phi_f)$ or $\mathbf{Q}(\theta_w, \phi_w)$ can now be calculated.

The constitutive properties of the fiber tows and polymer matrix of the plain weave composite lamina analyzed come from Scida *et al.* [3]. The lamina is an E-glass and vinylester composite, with the geometric parameters listed in Table 5.1 and the material properties listed in Table 5.2. Note that the properties for the fiber tow are aligned in the x_1 direction and will be rotated appropriately with Equation (5.6). These are the same material properties used in the isotropic/transversely isotropic volume fraction study and the material angle study in Chapter Four, Sections 4.3.3 and 4.4, respectively.

Table 5.1: The geometric parameters of the plain weave lamina studied, from [3]

		Fill	Warp	RVE
Height h	(mm)	0.05	0.05	0.10
Width a	(mm)	0.60	0.60	1.20

Table 5.2: The properties of the plain weave lamina matrix (vinylester) and fiber tow (E-glass/vinylester) used in this study, from [3]

		Fiber Tow (E-glass/Vinylester)	Matrix (Vinylester)
E_{11}	(GPa)	57.5	3.4
$E_{22} = E_{33}$	(GPa)	18.8	3.4
$G_{12} = G_{13}$	(GPa)	7.44	1.49
G_{23}	(GPa)	7.26	1.49
$\nu_{12} = \nu_{13}$		0.25	0.35
ν_{23}		0.29	0.35

5.2.2 COMSOL Model

A model of the described geometry was created and analyzed in COMSOL to provide a set of reference results to compare the MVE elements against. Figure 5.5 presents the model used; the left image shows the unmeshed geometry of the full RVE with both the matrix and the strands. To demonstrate the woven architecture, the center and right images show the matrix removed and the quarter RVE, respectively.

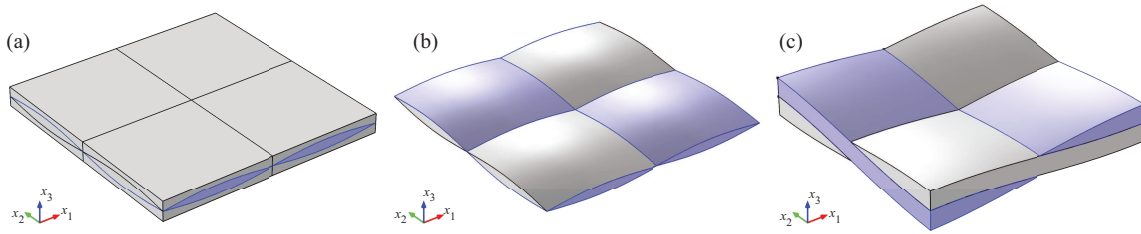


Figure 5.5: The plain weave woven geometry as modeled in COMSOL. (a) The full RVE model domain, (b) the full RVE with the matrix is removed, and (c) the quarter RVE without matrix to highlight the tow geometry.

COMSOL 5.2 contains a feature to apply periodic boundary conditions, but does not directly allow the application of added displacements. However, a method for applying periodicity in older versions of the software (specifically, Version 4.0) was found, and a similar procedure was adapted for use in this study [81]. A linear extrusion of the boundary is imposed from the desired source face to the desired destination face. This extrusion is then used in a pointwise constraint, which constrains the defined input expression to equal zero. The pointwise constraint from Equation (3.54) for mathematical periodicity is applied to the destination face with the equivalent expression

$$u^{\text{dest}} - u^{\text{src}} - c_{ij} = 0 \quad (5.11)$$

set as the constraint. From a comparison of results with the two-dimensional shear

study from Xia *et al.* [25], it was determined this method for applying the periodic boundary conditions in COMSOL yielded identical results to those from Xia *et al.* [25].

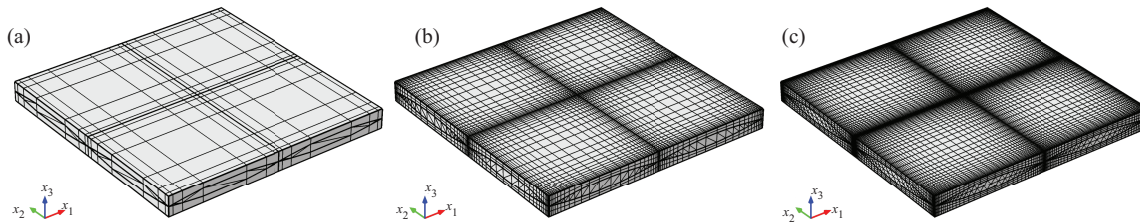


Figure 5.6: The plain weave woven geometry as meshed in COMSOL, with (a) 1,064 elements, (b) 19,600 elements, and (c) 68,968 elements.

The mesh of the COMSOL model (shown in Figure 5.6) was tested for convergence by running the stiffness tensor prediction study for different mesh densities. The purpose of this study is to determine how many elements are needed to determine a consistent solution. To determine this, the relative error as a function of the number of elements used N_{el} is calculated as

$$\text{Rel Err}_{ijkl}(N_{el}) \equiv \left| \frac{C_{ijkl}(N_{el}^{\max}) - C_{ijkl}^{\text{MVE}}(N_{el})}{C_{ijkl}^{\text{MVE}}(N_{el}^{\max})} \right| \quad (5.12)$$

where N_{el}^{\max} is the maximum number of elements used in the entire study.

Figure 5.7 shows the relative error from select stiffness tensor components obtained from the RVE analysis as a function of increasing elements (i.e., mesh refinement). The dashed line is the 5% of the true answer bound, and the dash-dotted line is the 1% error bound. As noted in the figure, by around 4,000 elements, a relatively coarse mesh, the calculated values of the stiffness tensor are within 1% of the values obtained from the highest mesh refinement. From this study, it was determined that COMSOL converges to a solution even with a low number of elements. Throughout the remainder of this study, the reference values for comparison will be

from the COMSOL model with 68,968 elements, the highest refinement mesh studied and depicted in Figure 5.6(c).

5.2.3 Results

Using the MATLAB code developed as part of this thesis and presented in the appendices, the geometry of the plain weave lamina defined in Tables 5.1 and 5.2 was analyzed using the MVEs described in Chapter Four and compared to the reference COMSOL model from the previous section and experimental results from Scida *et al.* [3]. Eight Gauss points were used in each coordinate direction within each MVE. A convergence study is also presented to determine if the number of elements used was enough to obtain a consistent result, as well as a computation time study to determine the effects of using parallelization and MEX functions.

For the analysis of the composite laminae, it is more intuitive to compare the engineering stiffness properties (tensile modulus E , shear modulus G , and Poisson's ratio ν) rather than the individual components of the stiffness tensor C_{ijkl} . For an orthotropic material, the nine independent engineering properties can be calculated from the compliance matrix \mathbf{S} as [6]

$$\mathbf{S} = \begin{bmatrix} \frac{1}{E_{11}} & -\frac{\nu_{12}}{E_{11}} & -\frac{\nu_{13}}{E_{11}} & 0 & 0 & 0 \\ -\frac{\nu_{12}}{E_{11}} & \frac{1}{E_{22}} & -\frac{\nu_{23}}{E_{22}} & 0 & 0 & 0 \\ -\frac{\nu_{13}}{E_{11}} & -\frac{\nu_{23}}{E_{22}} & \frac{1}{E_{33}} & 0 & 0 & 0 \\ 0 & 0 & 0 & \frac{1}{G_{23}} & 0 & 0 \\ 0 & 0 & 0 & 0 & \frac{1}{G_{13}} & 0 \\ 0 & 0 & 0 & 0 & 0 & \frac{1}{G_{12}} \end{bmatrix} = \mathbf{C}^{-1} \quad (5.13)$$

where \mathbf{S} is the matrix inverse of the contracted form of the stiffness tensor \mathbf{C} . To quantify the error between the MVE approach and the “true” finite element solution from COMSOL, the percent absolute error of the engineering properties is defined as

$$\text{Error} = \left| \frac{\text{True Value} - \text{Approx. Value}}{\text{True Value}} \right| \quad (5.14)$$

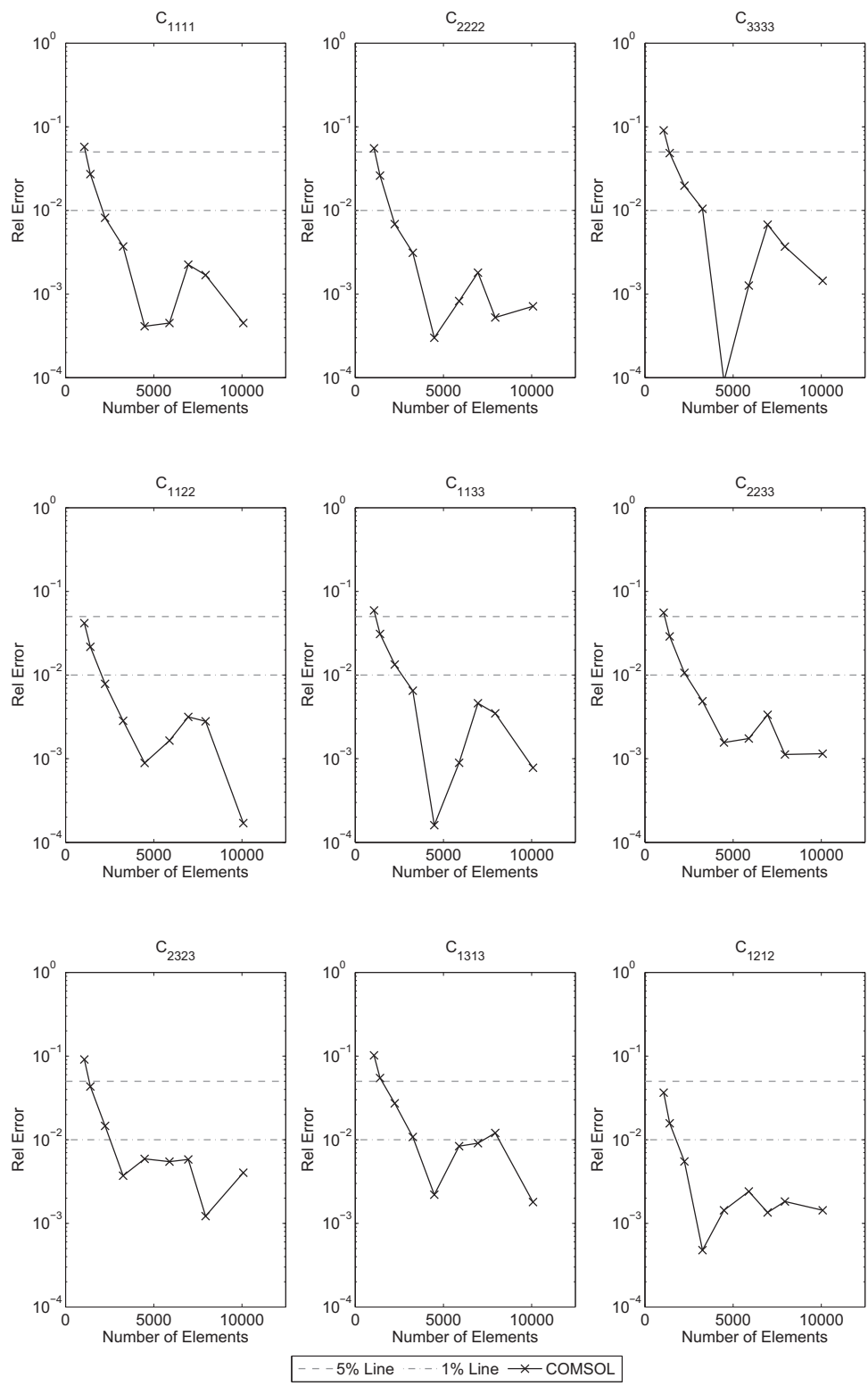


Figure 5.7: The relative error defined in Equation (5.12) of select engineering properties through analysis in COMSOL. By 4,000 elements, most of the values converge to within 1% of the “true” solution

5.2.3.1 Computation Time. To demonstrate the savings in computation time with the use of parallelization and MEX function generation, the STC–MVE implementation of Figure 5.1 was used to analyze the plain weave composite described in Tables 5.1 and 5.2. The machine used for this analysis has two Intel Xeon E5-2665 processors, each with eight cores, and 256 GB of shared memory; within MATLAB, a parallel pool of 12 workers was created. At 2,000 nodes (1,444 elements), the MATLAB code was timed using the `tic` and `toc` commands with the various combinations of optimization methods; these times are listed in Table 5.3. As indicated in the table, parallelization and the use of MEX functions individually cut the computation down nearly eight fold; using both enhancements together drops the computation time to almost 2% of the original run time.

Table 5.3: Comparison of computation time for the STC–MVE using various combinations of optimization methods

	Time (s)
No Optimization	380.6
Parallelization	51.1
MEX Functions	50.2
Both	8.7

While these times could be compared to COMSOL, the comparison would not be a fair one for a number of reasons. Due to the proprietary nature of the code used in COMSOL, there is little way of determining how the program calculates the parametric study used to calculate the six strain states. Further, as COMSOL is a software package that is sold commercially, it is expected that the code is more optimized.

5.2.3.2 Convergence. To determine the number of elements needed to present a converged solution using the MVE technique, the plain weave composite lamina

was analyzed with increasingly finer meshes. The mesh in the thickness direction x_3 is refined at a quarter of the rate of the planar coordinates; for example, one of the meshes tested had 48 nodes in both the x_1 and x_2 directions, and 12 nodes in the x_3 direction (or $47 \times 47 \times 11$ elements). This ratio was chosen as a balance between keeping the dimensions of the elements as equivalent as possible and having an equal number of elements in all directions.

Because of the large planar dimensions relative to the through thickness, at the extremes, keeping the elements close to cuboid does not allow for much refinement through the thickness of the lamina, but having an equal number of elements along each dimension over-refines the mesh in x_3 , which can use computational resources that could be better applied towards analyzing the much larger and more complex planar geometry.

The engineering stiffness properties were calculated for a variety of mesh sizes, and the relative error is calculated using Equation (5.12) and presented in Figure 5.8. This result does not show convergence to the true solution, but only that there is no benefit with further mesh refinements. Accuracy of the MVEs will be discussed in Section 5.2.3.3.

For almost all cases, the relative error is within 1% of the finest mesh by around 20,000 elements and was therefore determined to be sufficient for a 4-to-1 element ratio. For the planar properties (E_{11} , E_{22} , G_{12} , and ν_{12}), the ASE and B-MVE converged faster, but for the other properties, the TMC-MVE and STC-MVE converged faster. This is almost 5 times the number of elements required in the COMSOL solution. However, the COMSOL model is using quadratic elements, with 9 nodes in a hexahedral element; this is inherently a more accurate element, but

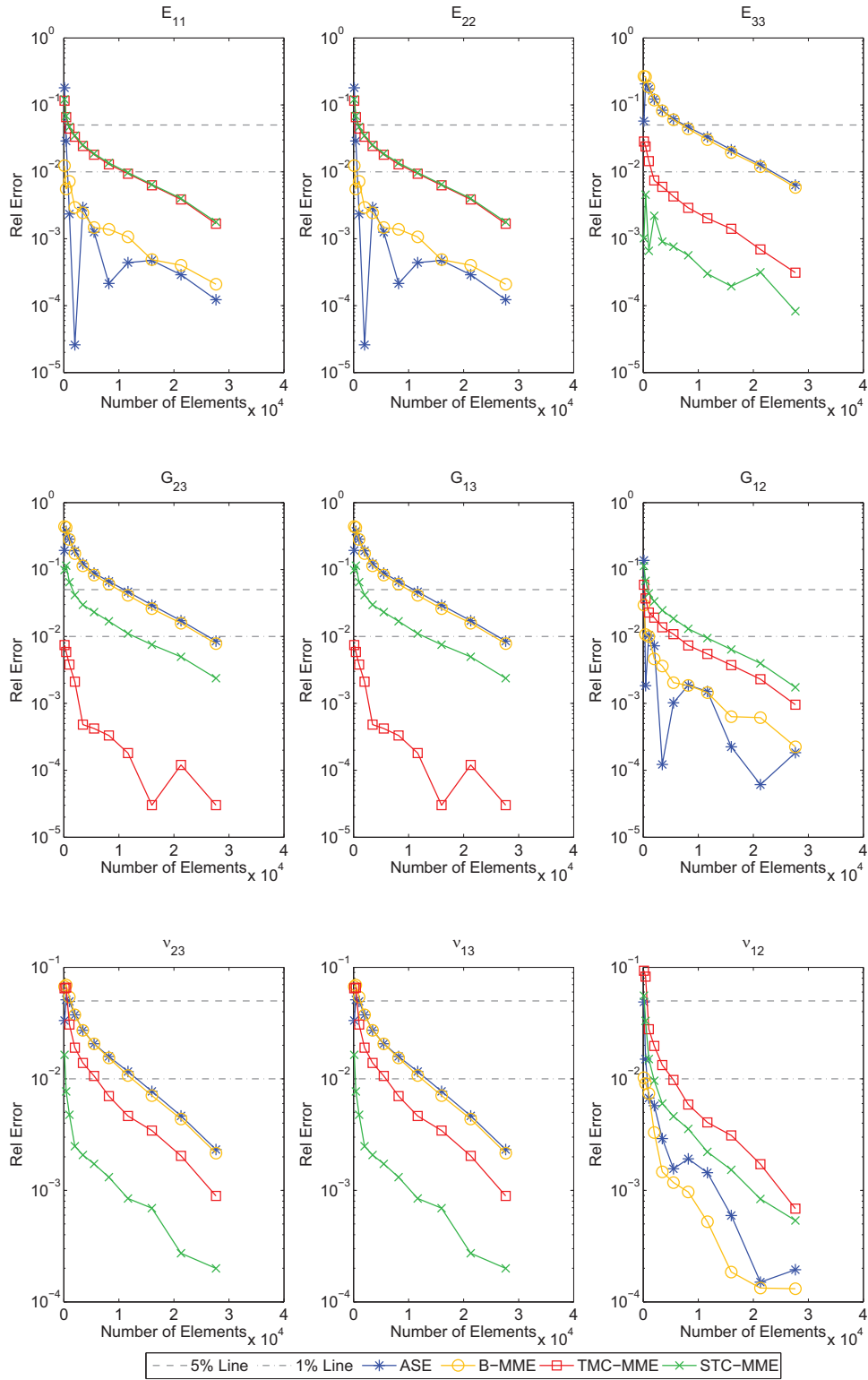


Figure 5.8: The relative error as defined in Equation (5.12) of select engineering stiffness properties through analysis of the plain weave lamina with the MVEs. The planar-to-thickness element ratio is 4:1

is more computationally expensive. The MVEs presented are linear elements, which compute faster, but are less accurate.

A similar convergence study was run for a 2:1 planar-to-thickness element ratio. Compared to the 4:1 planar-to-element ratio, some of the error for the out of plane components was reduced, but overall, the change in results was negligible. Therefore, a 4:1 ratio will be used.

5.2.3.3 Comparison of Calculated Engineering Properties. For the following MVE studies, a mesh of 39,325 elements ($55 \times 55 \times 13$) was selected as it was available from the convergence study. Table 5.4 shows the calculated engineering properties for the plain weave composite lamina, determined from using the MATLAB FEA code for MVEs to calculate the contracted form of the stiffness tensor \mathbf{C} from the periodic RVE and then computing the engineering properties using Equation (5.13). The experimental results from Scida *et al.* [3] are presented in Table 5.4, along with a solution using COMSOL with classic finite elements.

Comparing the COMSOL results with the experimental results in Table 5.4 shows that the plain weave geometry used for the analysis is in good agreement with experimental results. While finding an accurate woven geometry model for use in finite element analysis is not an objective of this study, it is useful to know that experimental results from literature can be used as a rough point of comparison for the MVEs when a COMSOL model is not available. An interesting artifact from the geometry can be observed in the calculation of E_{33} ; because there is no resin pocket between the fill and warp strands in the COMSOL model, the influence of the strands is overpredicted in the x_3 direction of the model. Therefore, as the transverse stiffness of the strands are stiffer than the matrix, the stiffness is overpredicted as compared

to the mean of experimental results (but is still within the experimental measurement error margin presented by [3]).

Table 5.4: The calculated values of the plain weave lamina engineering stiffness properties with the MVEs, classic finite elements, and experimental values from [3]

	ASE	B-MVE	TMC-MVE	STC-MVE	COMSOL	Exp. [3]
E_{11} (GPa)	24.92	24.92	24.36	24.34	24.47	24.8 ± 1.1
E_{22} (GPa)	24.92	24.92	24.36	24.34	24.47	24.8 ± 1.1
E_{33} (GPa)	10.99	10.85	10.24	10.20	9.90	8.5 ± 2.6
G_{23} (GPa)	3.66	3.60	3.32	3.24	3.22	4.2 ± 0.7
G_{13} (GPa)	3.66	3.60	3.32	3.24	3.22	4.2 ± 0.7
G_{12} (GPa)	4.90	4.90	4.82	4.78	4.81	6.5 ± 0.8
ν_{23}	0.32	0.33	0.33	0.33	0.34	0.28 ± 0.07
ν_{13}	0.32	0.33	0.33	0.33	0.34	0.28 ± 0.07
ν_{12}	0.14	0.14	0.14	0.14	0.14	0.1 ± 0.01

Looking at Table 5.4 qualitatively, all of the MVEs performed well in the analysis of the plain weave lamina. All values are similar to those from the classic finite element solution, as hoped for. This suggests that any of these methods are a reasonable selection for an estimate of the material properties.

The percent relative error calculations found in Table 5.5 can be used to obtain a more quantitative analysis. Table 5.5 compares the percent absolute relative error of the engineering properties calculated by MVEs as compared to the properties calculated in using the commercial finite element solver. The ASE and B-MVE perform similarly for all properties calculated. The lowest errors for these two methods are found in the planar properties (E_{11} , E_{22} , G_{12} , and ν_{12}), showing less than a 1% error for ν_{12} , while predicting the other planar properties at around a 2% error. However, the ASE and B-MVE poorly predict the out of plane properties, returning around a 10% error for E_{33} and a 12%–14% error on G_{23} and G_{13} .

The accuracy of results from the TMC-MVE and the STC-MVE improve

Table 5.5: The percent absolute error for the MVEs in the plain weave study as compared to COMSOL, calculated using Equation (5.14)

(%)	ASE	B-MVE	TMC-MVE	STC-MVE
E_{11}^{err}	1.84	1.83	0.44	0.54
E_{22}^{err}	1.84	1.83	0.44	0.54
E_{33}^{err}	10.99	9.60	3.44	3.01
G_{23}^{err}	13.64	11.82	3.07	0.69
G_{13}^{err}	13.64	11.81	3.07	0.69
G_{12}^{err}	1.96	1.88	0.26	0.58
ν_{23}^{err}	4.21	3.72	2.23	1.59
ν_{13}^{err}	4.21	3.72	2.23	1.59
ν_{12}^{err}	0.31	0.47	0.93	0.82

significantly upon the ASE and B-MVE approaches. The planar properties predicted by these two MVEs are within 1% of the stiffness results produced by COMSOL. The maximum error overall for both the TMC-MVE and STC-MVE is calculated for E_{33} , and that error is only $\sim 3.0\%$, with the STC-MVE yielding the more accurate result. While it may be worth further investigations to reduce this error, it is relatively low compared to the greater than 10% error in the predicted E_{33} from the ASE and B-MVE.

An interesting trend to note is that, relative to the other properties, the calculated error for E_{33} is consistently high for all of the MVEs as compared to COMSOL, which is inconsistent with the studies performed in Chapter Four (see e.g., Figure 4.15 and Table 4.8). A part of this may be related to the mesh refinement issue described in the convergence study in Figure 5.8; the MVEs may be sensitive to how the geometry is meshed. A future study should be performed to determine how the ratio of the number of MVEs in each direction affects the property calculation.

Overall, the newly proposed STC-MVE produced results closest to the COMSOL results for nearly all stiffness components. The greatest improvement in property prediction as compared to the other MVEs is found in the out of plane shear

moduli G_{23} and G_{13} . The ASE and B-MVE predict these properties with a greater than 10% error and the newly proposed TMC-MVE yields a 3.07% error. However, this error drops to less than 1% for the STC-MVE. Recall the STC-MVE uses exclusively the material stiffness moduli in the x_i and x_j directions for the calculation of the effective shear stiffness in Equation (4.27), which directly relates to shear moduli G_{ij} . The reduced accuracy from the B-MVE is due to the lack of strain correction in the transverse direction to a load, and the TMC-MVE only uses the tensile moduli E_i to correct these values.

5.2.4 Section Conclusion

In this section, the geometry of a plain weave composite lamina was defined and analyzed using the MVEs presented in Chapter Four. The newly presented TMC-MVE and STC-MVE showed significant improvement over the ASE and B-MVE. In particular, the error on the out of plane tensile modulus E_{33} was decreased from about 10% to about 3%. Further, the out of plane shear moduli G_{23} and G_{13} were decreased from about 12%–14% to about 3% for the TMC-MVE. The STC-MVE showed an even greater improvement on this figure, dropping the error to less than 1%.

Coupled with the simple analyses of Chapter Four, the MVE models presented here have been shown to be valid, with the STC-MVE providing the best accuracy overall. For future work, the inclusion of the extension–extension terms and perhaps the anisotropic terms from the stiffness tensor should be incorporated into the strain correction factors. Further, there is still room for improvement on the prediction of the shear stiffness terms. However, it has been effectively shown that the way the shear stiffness terms are handled within the STC-MVE helps provide a superior accuracy over the other MVEs presented.

5.3 Analyses of Other Weave Types

To demonstrate the versatility of the MVEs presented, two other woven geometries will be presented and analyzed: a satin weave and a twill weave. These weaves are also common in industry; their use is favored in applications where a highly drapable fabric is required. In other words, the fabrics are more easily laid and shaped over complex molds; plain weave composites tend not to drape very well as compared to these looser weaves [80]. However, satin and twill weaves have a more complex and larger RVE than the plain weave laminae, and therefore are harder to analyze using classical finite elements. For the MVE method, however, the mesh for the various weaves is identical and no new meshing is required for each new weave type.

5.3.1 Twill Weave Lamina

This section will detail the analysis of a twill weave lamina, as depicted in Figure 5.10. A twill weave often balances the weave stability of a plain weave lamina with the drapability of a satin weave lamina [80]. The weave depicted in Figure 5.9 is specifically referred to as a 2/2 twill weave, where a strand will pass under two strands then over two strands. Again, the pattern is offset by one each row and column, creating a “stairstep” pattern; this generates an RVE four sections by four sections.

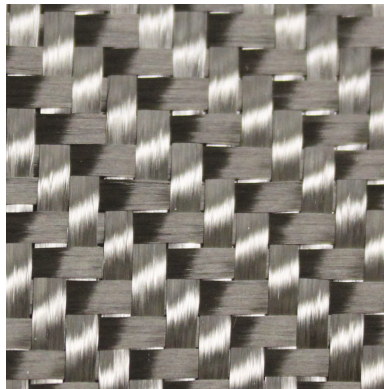


Figure 5.9: A picture of carbon fiber 2/2 twill weave fabric

No COMSOL model was generated for this study, so the properties predicted by the MVEs will again be compared to analytic and experimental results from Scida *et al.* [3].

5.3.1.1 Geometry. As with the plain weave RVE, the geometry of the twill weave RVE is based on the functions provided by Scida *et al.* [13]. Most of the functions are the same as the functions for the plain weave lamina; the thickness functions $e_f(x_2)$ and $e_w(x_1)$ are the same as in Equations (5.3) and (5.4) for the plain weave lamina. The determination of the local stiffness tensor at a given point is still found through the piecewise relationship in Equation (5.5), and the angles of the strands at a given point $\gamma_f(x_1, x_2)$ and $\gamma_w(x_1, x_2)$ are given by Equations (5.8) and (5.9). The major change between the the plain weave and twill weave is found in the definition of the undulation functions, $H_f(x_1, x_2)$ and $H_w(x_1, x_2)$.

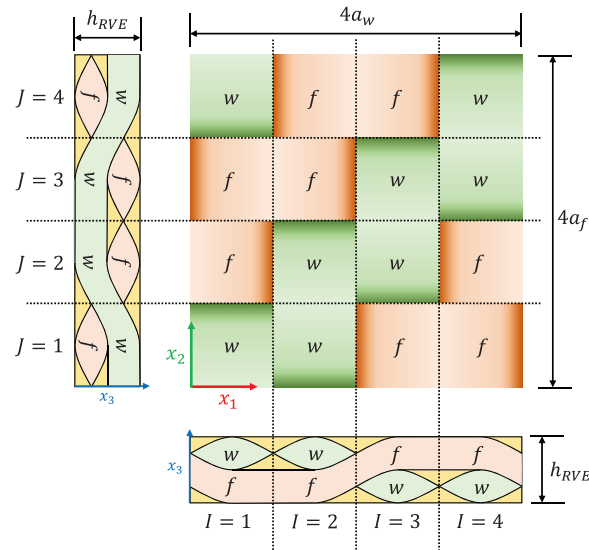


Figure 5.10: Top and side views of 2/2 twill weave composite lamina. Fill strands (f) are represented in red, and warp strands (w) are represented in green.

A piecewise function is used to define the undulation functions of a 2/2 twill weave composite lamina with the domain $\{0 \leq x_1 \leq 4a_w; 0 \leq x_2 \leq 4a_f; -(h_f + h_w) \leq$

$x_3 \leq (h_f + h_w)\}$. The lamina is split up into 4×4 sections, as depicted in Figure 5.10. The sections are assigned coordinates (I, J) to determine the interaction between the I^{th} fill strand and the J^{th} warp strand. The individual section coordinates $I \equiv I(x_1)$ and $J \equiv J(x_2)$ can be determined from the (x_1, x_2) coordinates of an arbitrary point as

$$I \equiv I(x_1) = \lceil \frac{x}{a_f} \rceil \quad J \equiv J(x_2) = \lceil \frac{y}{a_w} \rceil \quad (5.15)$$

where the brackets $\lceil \cdot \rceil$ imply rounding up the quantity in the brackets to the next integer (i.e., the ceiling function). In the case of $x_1 = 0$, I is set equal to 1, and when $x_2 = 0$, J is set equal to 1. These section coordinates can then be used to calculate the piecewise undulation function that defines the fill strand as

$$H_f(x_1, x_2) = \begin{cases} S_w(x_1, x_2) & (J - \frac{3}{2}) a_w \leq x_1 \leq (J - \frac{1}{2}) a_w \\ & \cup (J + \frac{5}{2}) a_w \leq x_1 \leq (J + \frac{7}{2}) a_w \\ -\frac{h_w}{2} & (J - \frac{1}{2}) a_w \leq x_1 \leq (J + \frac{1}{2}) a_w \\ & \cup (J - \frac{9}{2}) a_w \leq x_1 \leq (J - \frac{7}{2}) a_w \\ -S_w(x_1, x_2) & (J + \frac{1}{2}) a_w \leq x_1 \leq (J + \frac{3}{2}) a_w \\ & \cup (J - \frac{7}{2}) a_w \leq x_1 \leq (J - \frac{5}{2}) a_w \\ \frac{h_w}{2} & \text{else} \end{cases} \quad (5.16)$$

and the undulation function of the warp strand as

$$H_w(x_1, x_2) = \begin{cases} S_f(x_1, x_2) & (I + \frac{3}{2}) a_w \leq x_2 \leq (I + \frac{5}{2}) a_w \\ & \cup (I - \frac{5}{2}) a_w \leq x_2 \leq (I - \frac{3}{2}) a_w \\ -\frac{h_f}{2} & (I + \frac{1}{2}) a_w \leq x_2 \leq (I + \frac{3}{2}) a_w \\ & \cup (I - \frac{7}{2}) a_w \leq x_2 \leq (I - \frac{5}{2}) a_w \\ -S_f(x_1, x_2) & (I - \frac{1}{2}) a_w \leq x_2 \leq (I + \frac{1}{2}) a_w \\ & \cup (I - \frac{9}{2}) a_w \leq x_2 \leq (I - \frac{7}{2}) a_w \\ \frac{h_f}{2} & \text{else} \end{cases} \quad (5.17)$$

where

$$S_f(x_1, x_2) = \frac{h_f}{2} \sin \left[\left(\frac{x_2}{a_f} + I(x_1) \right) \pi \right] \quad (5.18)$$

$$S_w(x_1, x_2) = \frac{h_w}{2} \sin \left[\left(\frac{x_1}{a_w} + J(x_2) \right) \pi \right] \quad (5.19)$$

When the derivative of H_f and H_w are taken for the calculation γ_f and γ_w in Equations (5.8) and (5.9), the derivative at a point where two subfunctions meet in the piecewise functions is zero as the undulation functions by construction are first-order smooth and continuous.

The composite lamina analyzed is a 2/2 twill carbon fiber with a bakelite matrix from Scida *et al.* [3]. The geometric parameters listed in Table 5.6 and the material properties are listed in Table 5.7.

Table 5.6: The geometric parameters of the 2/2 twill weave lamina, from [3]

	Fill	Warp	RVE
Height h (mm)	0.15	0.15	0.30
Width a (mm)	1.50	1.50	6.00

Table 5.7: The properties of the 2/2 twill weave lamina matrix (Bakelite) and fiber tow (carbon/Bakelite) used in this study, from [3]

	Fiber Tow (Carbon/Bakelite)	Matrix (Bakelite)
E_{11} (GPa)	137	3.2
$E_{22} = E_{33}$ (GPa)	9.57	3.2
$G_{12} = G_{13}$ (GPa)	4.74	1.19
G_{23} (GPa)	3.23	1.19
$\nu_{12} = \nu_{13}$	0.31	0.35
ν_{23}	0.45	0.35

5.3.1.2 Results. The twill weave was analyzed using 31,212 ($51 \times 51 \times 12$) elements for each of the MVEs. Table 5.8 presents the results from these studies alongside the analytic model proposed by Scida *et al.* [3, 13] (MESOTEX), as well as the available experimental results from these papers. It should be noted that Table 5.8 compares a finite element method, an analytic method, and an experimental

method. The experimental results were only for select components of stiffness, but show a general agreement of the results from the MVE approach with experimental observations. The results here are only meant to show a general agreement of results across the different methods.

Table 5.8: The MVE calculated values of the engineering stiffness properties of the twill weave compared against analytic and experimental results from [3]

	ASE	B-MVE	TMC-MVE	STC-MVE	MESOTEX [3]	Exp. [3]
E_{11} (GPa)	44.83	44.89	43.18	42.98	46.11	49.38
E_{22} (GPa)	44.83	44.89	43.18	42.98	46.11	49.38
E_{33} (GPa)	8.13	8.05	7.80	7.77	8.18	n/a
G_{23} (GPa)	2.49	2.45	2.30	2.26	3.09	n/a
G_{13} (GPa)	2.49	2.45	2.30	2.26	3.09	n/a
G_{12} (GPa)	3.23	3.23	3.15	3.05	3.33	2.36
ν_{23}	0.46	0.46	0.46	0.46	0.44	n/a
ν_{13}	0.46	0.46	0.46	0.46	0.44	n/a
ν_{12}	0.09	0.09	0.08	0.08	0.04	0.059

The MVEs, qualitatively, are in fair agreement with the MESOTEX and experimental results. In this set of results, the ASE appears to perform the best overall as compared to MESOTEX. As compared to the experimental results, the B-MVE has the best agreement for E_{11} and E_{22} , and the STC-MVE provides the closest result for G_{12} and ν_{12} . Again, the results here are not a fully valid comparison.

Despite the fair agreement of the MVEs with the analytic and experimental results, the discrepancy in the values are enough to wonder if there was a source of this error other than inaccuracies in the MVE formulation. In Scida *et al.* [3], the material properties for the fiber tow in Table 5.7 are generated using a numerical micromechanics technique. In a results comparison made by Tucker and Liang [21], even at high aspect ratios, these micromechanics methods can disagree by upwards of 10%–15%. Thus, the STC-MVE was used to reanalyze the twill weave with a 10% increase on the modulus values presented in Table 5.7 (the Poisson’s ratios remained

the same); Table 5.9 shows the results from this “adjusted” study, compared against the relevant results from Table 5.8.

Table 5.9: The STC–MVE calculated values of the adjusted engineering stiffness properties of the twill weave compared against analytic and experimental results from [3]

		Original	Adjusted	MESOTEX [3]	Exp. [3]
E_{11}	(GPa)	42.98	46.96	46.11	49.38
E_{22}	(GPa)	42.98	46.96	46.11	49.38
E_{33}	(GPa)	7.77	8.19	8.18	n/a
G_{23}	(GPa)	2.26	2.35	3.09	n/a
G_{13}	(GPa)	2.26	2.35	3.09	n/a
G_{12}	(GPa)	3.05	3.28	3.33	2.36
ν_{23}		0.46	0.46	0.44	n/a
ν_{13}		0.46	0.46	0.44	n/a
ν_{12}		0.08	0.09	0.04	0.059

The tensile moduli from the adjusted study are in much better agreement with the experimental results. The values of E_{11} and E_{22} now differ by only about 5%, rather than about 13% in the original study. While no experimental results were given for E_{33} , the adjusted study shows better agreement with the analytic model for E_{33} . For G_{12} , the adjusted results less accurate than the original results, but this is because all of the input shear moduli were increased by 10%; therefore, the already high result from the original study became higher.

When the inputs from the micromechanics models are reasonably adjusted, the STC–MVE agreed much better with experimental results. Therefore, based on the available results, the MVEs appear to predict the properties of the twill weave with a reasonable degree of accuracy. Ideally, a traditional finite element model using the exact model as presented would be used as a reference for the MVEs, thus this will be reserved for a future study.

5.3.2 Satin Weave Lamina

This section will detail the geometry and analysis of the satin weave to show the strengths of the MVE approach. A type of satin weave is pictured in Figure 5.11. The results are compared to the select components provided by from Scida *et al.* [3].

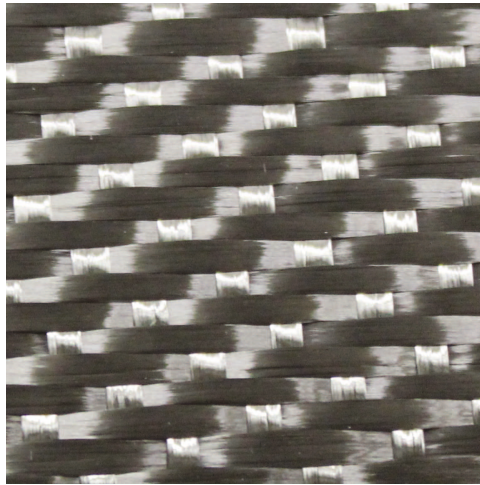


Figure 5.11: A picture of a type of carbon fiber 5HS satin weave fabric

5.3.2.1 Geometry. An n_g -harness satin weave composite is woven in such a way so that the fill and warp strands only interlace every n_g strands, where n_g refers to the harness number of the weave. For example, a 5-harness satin (5HS) weave is depicted in Figure 5.12. The 5HS has fill strands that only interlace at every 5th warp strand, and warp strands that only interlace at every 5th fill strand. The interlaced regions are offset by one section each row and column down the fabric, which visually gives the fabric a diagonal pattern. This weave pattern allows for higher drapability of the fabric, but has low stability during handling and manufacturing and can unravel easily [80]. A plain weave composite can be thought of as a 2HS weave.

As with the plain and twill weaves, the geometry of the satin weave RVE is derived from functions provided by Scida *et al.* [13]. Again, most of the functions are

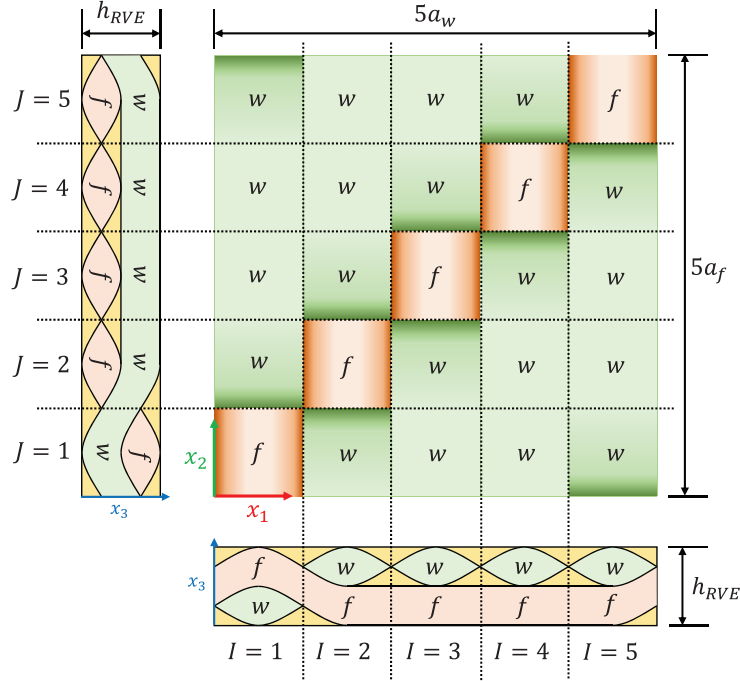


Figure 5.12: Top and side views of a 5-harness satin weave composite lamina. Fill strands (f) are represented in red, and warp strands (w) are represented in green.

the same as the functions for the plain weave and twill weave laminae, with only an alteration in the undulation functions, $H_f(x_1, x_2)$ and $H_w(x_1, x_2)$. The satin weave is defined similarly to the twill weave, using piecewise based functions dependent upon section coordinates (I, J) defined in Equation (5.15). The domain occupied by the satin weave lamina is defined by the region $\{0 \leq x_1 \leq n_g a_w, 0 \leq x_2 \leq n_g a_f, -(h_f + h_w) \leq x_3 \leq (h_f + h_w)\}$. Thus, the undulation functions for a general n_g -harness satin weave in Figure 5.12 are

$$H_f(x_1, x_2) = \begin{cases} (-1)^{n_g+1} S_w(x_1, x_2) & 0 \leq x_1 \leq \left(J + \frac{1}{2} - n_g\right) a_w \\ & \cup \left(J - \frac{3}{2} + n_g\right) a_w \leq x_1 \leq n_g a_w \\ -S_w(x_1, x_2) & \left(J - \frac{3}{2}\right) a_w \leq x_1 \leq \left(J + \frac{1}{2}\right) a_w \\ -\frac{h_w}{2} & \text{else} \end{cases} \quad (5.20)$$

$$H_w(x_1, x_2) = \begin{cases} (-1)^{n_g} S_f(x_1, x_2) & 0 \leq x_2 \leq (I + \frac{1}{2} - n_g) a_f \\ & \cup (I - \frac{3}{2} + n_g) a_w \leq x_2 \leq n_g a_f \\ S_f(x_1, x_2) & (I - \frac{3}{2}) a_f \leq x_2 \leq (I + \frac{1}{2}) a_f \\ \frac{h_f}{2} & \text{else} \end{cases} \quad (5.21)$$

where $S_f(x_1, x_2)$ is as defined in Equation (5.18) and $S_w(x_1, x_2)$ is as defined in Equation (5.19). As for the twill weave, the functions defined in Equations (5.20) and (5.21) are first-order continuous and as such the derivatives everywhere are continuous.

The composite lamina presented in this thesis is an 8-harness satin (8HS) E-glass and epoxy composite from Scida *et al.* [3]. The geometric parameters from [3] are listed in Table 5.10 and the material properties from [3] are listed in Table 5.11. Note that the calculation of the width of the RVE is found by taking the strand width and multiplying by n_g ; in this case, $n_g = 8$, so the RVE dimensions are $8a_w \times 8a_f \times h_{RVE}$.

Table 5.10: The geometric parameters of the 8HS weave lamina studied, from [3]

	Fill	Warp	RVE
Height h (mm)	0.09	0.09	0.18
Width a (mm)	0.60	0.60	4.80

Table 5.11: The properties of the 8HS weave lamina matrix (epoxy) and fiber tow (E-glass/epoxy) used in this study, from [3]

	Fiber Tow (E-glass/Epoxy)	Matrix (Epoxy)
E_{11} (GPa)	59.3	3.2
$E_{22} = E_{33}$ (GPa)	23.2	3.2
$G_{12} = G_{13}$ (GPa)	8.68	1.16
G_{23} (GPa)	7.60	1.16
$\nu_{12} = \nu_{13}$	0.21	0.38
ν_{23}	0.32	0.38

5.3.2.2 Results. The 8HS weave was analyzed using 31,212 ($51 \times 51 \times 12$) elements for each of the MVEs. Table 5.12 presents the results from these studies alongside an analytic mesomechanical model proposed by Scida *et al.* [3, 13] (MESOTEX), as well as the experimental results from these papers. The values from the mesomechanics method and the experimental method are only an approximate comparison and shows the MVE method predicts results similar to those in literature.

In general, the MVEs are in fair agreement with the MESOTEX method and the available experimental results, but there remains some room for improvement. This study does not validate or invalidate the use of the MVEs; that is best done against a full finite element mesh as was done in Section 5.2. In the plain weave study, the planar tensile moduli E_{11} and E_{22} were in very good agreement for all of the MVEs; in this study, however, it appears that E_{11} and E_{22} are consistently overpredicted by each MVE approach, while E_{33} was underpredicted. However, it should be noted that the behavior exhibited by the MVEs in this study appears to be consistent with previous studies. For example, the values calculated with the ASE and B-MVE are about the same, as in Table 5.4. The same observation is made with the tensile moduli predicted with the TMC-MVE and the STC-MVE.

It is entirely possible this is again a function of the material inputs found in Table 5.11; as discussed with the twill weave, numerically determining the properties of a fiber tow with different micromechanics models can provide a spread of results spanning 10% – 15%. However, there may be another factor at play here, namely that the method is simply not converged. Indeed, the plain weave lamina was analyzed using 55 elements in each planar direction; given there are two strands in each direction, this means that there are around 28 elements dedicated to each strand along the coordinate axes. The 8HS lamina was analyzed using 51 elements in each

planar direction (this lower number was selected due to memory constraints), and therefore only about 6 elements are dedicated to each strain along the coordinate axes. Therefore, it is plausible to postulate that the solutions in Table 5.12 are not fully converged.

Table 5.12: The MVE calculated values of the engineering stiffness properties of the 8HS weave compared against analytic and experimental results from [3]

	ASE	B-MVE	TMC-MVE	STC-MVE	MESOTEX [3]	Exp. [3]
E_{11} (GPa)	35.64	35.09	30.73	30.60	26.03	25.6
E_{22} (GPa)	35.64	35.09	30.73	30.60	26.03	25.6
E_{33} (GPa)	13.81	13.17	11.84	11.69	15.65	n/a
G_{23} (GPa)	4.05	3.74	3.08	2.94	5.42	n/a
G_{13} (GPa)	4.05	3.74	3.08	2.94	5.42	n/a
G_{12} (GPa)	5.39	5.33	4.57	4.31	5.67	5.7
ν_{23}	0.31	0.31	0.34	0.34	0.28	n/a
ν_{13}	0.31	0.31	0.34	0.34	0.28	n/a
ν_{12}	0.21	0.20	0.17	0.18	0.13	0.13

A convergence study was run for the 8HS lamina, using the relative error calculation from Equation (5.13). The results of this study are presented in Figure 5.13. The results show that the MVEs appear to still be converging when the highest number of elements is run. In each case, the relative error of the MVEs is barely passing the 1% mark (the dashed-dotted line). Further, the error curve is not smooth, but rather jagged; this may be because the material boundaries within the MVEs are changing drastically with each mesh resolution increase.

The apparent solution is to generate a mesh with more elements. However, the memory required to solve the system was on the order of 250 GB. The custom MATLAB code described in Section 5.1 is only optimized for computation time and not for memory usage; there is only a limited use of memory saving techniques, such as using sparse matrices when parsing the system into \mathbf{K}_{ff} , \mathbf{K}_{pf} , etc. as in Equation

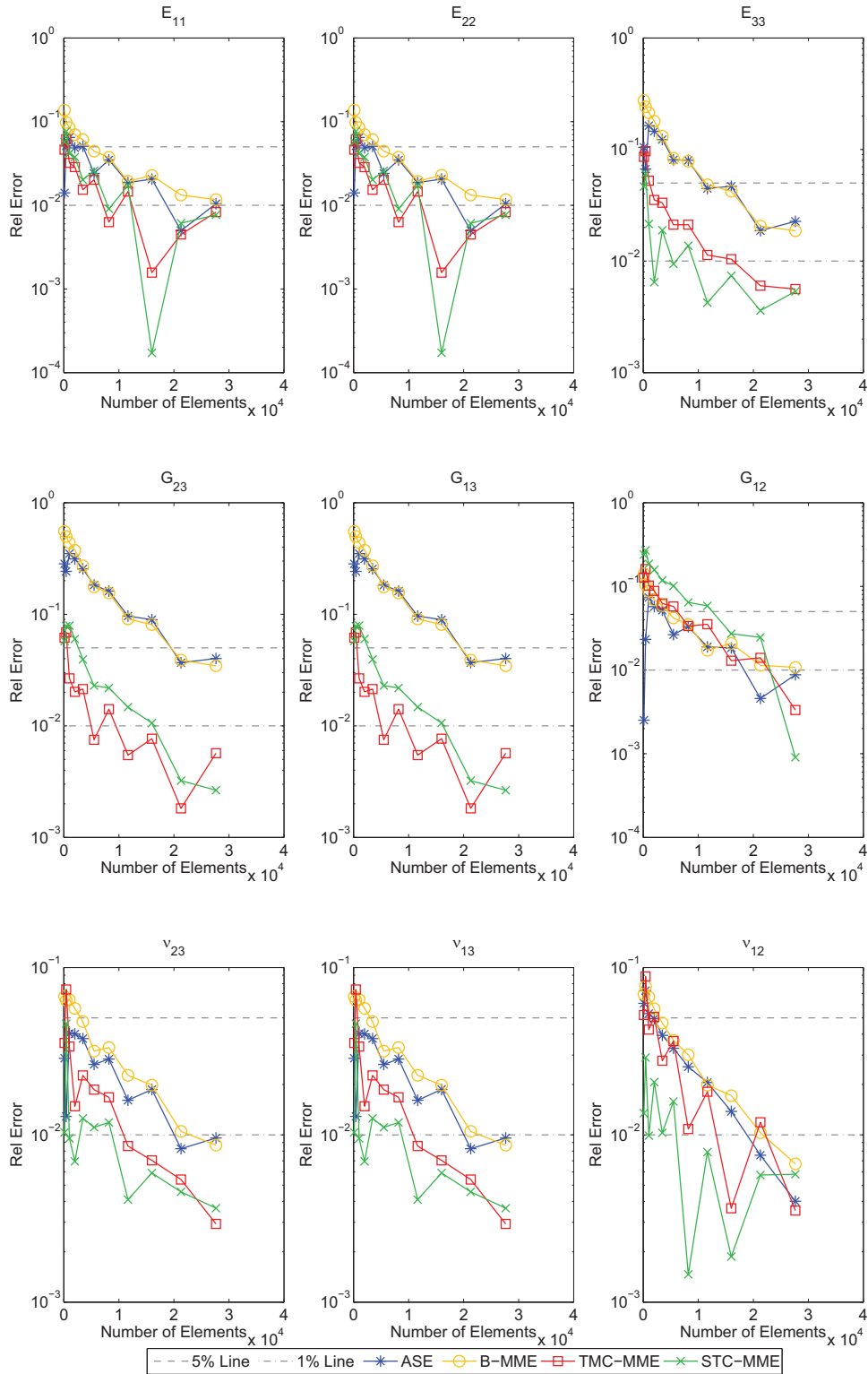


Figure 5.13: The relative error as defined in Equation (5.12) of select engineering properties through analysis of the 8HS satin weave lamina with the MVEs.

(3.64). A technique used by COMSOL to conserve memory is to use virtual memory on the hard disk of the machine [82]; a crude version of this was attempted, but significantly increased the computation time.

Currently, because of the way parallelization the periodic boundary conditions are handled in the code, the full global matrix \mathbf{K} from Equation (3.51) cannot be stored as a sparse matrix. With around 35,000 nodes, and 3 degrees of freedom for each node, this amounts to a matrix that contains 11×10^9 elements. This alone consumes about 83 GB of memory. If \mathbf{K} was allowed to be a sparse matrix, this memory consumption would be reduced to less than 1 GB. Therefore, future work on this research will require restructuring the code for more efficient memory usage.

5.4 Concluding Remarks

The structure of a custom finite element code in MATLAB was presented for use in analyzing geometries generated functionally. This finite element code was used to analyze various woven geometries using each of the MVE methods presented in Chapter Four. The geometries of a plain weave, satin weave, and twill weave composite lamina were defined and analyzed with various methods using parameter presented in Scida *et al.* [3]. Of the three laminae presented, the plain weave composite was analyzed the most extensively due to the availability of high quality experimental data and full finite element solutions.

From the analysis of the plain weave composite, the STC–MVE performed the best overall, predicting most properties with less than a 2% error as compared to a traditional finite element model defined as the true result. The most significant improvement of the STC–MVE over the other MVEs is the more accurate prediction of the out of plane shear moduli G_{23} and G_{13} ; this is due to the strain corrections taking into account the shear properties within the entire plane of interest.

For the satin and twill weaves, thorough analyses were both limited by the lack of models for the laminae in commercial software and by memory limitations. Future work should be performed to determine the accuracy of the MVEs in the application of weave types other than plain weave composites. The code used in this study should be restructured to allow for more efficient use of memory; further, a model that can be analyzed easily in both commercial software and the MATLAB code should be determined. A promising alternative is a program such as WiseTex [47] or TexGen [7, 48], the latter of which will automatically generate a woven RVE and ABAQUS mesh. These programs will work well if the constituent materials are isotropic; the fiber angle, however, is needed in order to determine the rotation of a transversely isotropic strand.

CHAPTER SIX

Conclusion

6.1 Revisiting the Thesis Objectives

To conclude the work presented here, the thesis objectives from Chapter 1 will be revisited. The objective of the research presented in this thesis was to

Construct a multiphase voxel finite element (MVE) allowing the construction of a mesh independent of internal geometry variations by incorporating material properties determined at the integration points for use in correctly predicting the averaged material stiffness tensor C_{ijkl} over the representative volume element (RVE) of a woven fabric composite lamina.

It has been shown in Chapters Four and Five that the objective of this research has been met. A set of four multiphase voxel elements (MVEs) — the ASE, B-MVE, TMC-MVE, and STC-MVE — were presented in Chapter Four, each of them utilizing material properties collected at the integration points to estimate the displacement within the element. These elements were analyzed using simple geometries and compared to a traditional finite element model; the conclusion was that the newly presented MVEs were superior to the MVEs presented in literature. In Chapter Five, these MVEs were used to extensively analyze a plain weave woven composite lamina; again, the newly presented MVEs showed superior performance in these analyses.

To detail these conclusions, the three points from Chapter One will be revisited.

- Expand upon the work of Caselman [1] by generalizing the strain correction factors within the MVE formulation to better account for the shear effect

- Determine the effectiveness of the existing methods that can be expressed in the general MVE form proposed in this thesis and the two newly proposed MVEs in calculating the averaged stiffness tensor C_{ijkl} of woven fabric composite laminae
- Expose shortcomings of the investigated MVEs in order to suggest further improvements and demonstrate the improved performance of the two newly proposed MVEs

6.1.1 *Extend the Work of Caselman*

Caselman [1] presented an element capable of applying the material properties at the integration points within an element, as opposed to the entire element domain as a whole, through the use of strain correction factors. The element presented was limited to an element containing two isotropic materials, which suited the application the element was originally developed for. For isotropic materials, he showed that the element he developed was an improvement over the element of Zeng [12], termed the B-MVE in this thesis.

The TMC-MVE presented in Chapter Four in Section 4.2.3 directly expands the formulation of Caselman's element. By replacing the isotropic tensile modulus E with the orthotropic tensile moduli E_{11} , E_{22} , and E_{33} , the formulation was expanded to include materials independent of the coordinate axis. Further, the spring analogy used by Caselman in his derivation was expanded from two springs in series to a general system of springs in series, thus expanding the number of materials that can be present within an MVE to as many integration points being used.

The STC-MVE, also presented in Chapter Four in Section 4.2.4, aimed to continue the extension of Caselman's theory on strain corrections by basing the derivation of the correction factors off of the components of the stiffness tensor C_{ijkl} instead of using the engineering stiffness properties. This was done because, through Hooke's

law, the stiffness tensor directly relates the resultant stress tensor σ_{ij} with the applied strain tensor ε_{ij} . Further, correction factors were developed for use in better predicting the shear stiffness modulus; these corrections for the shear stiffness components C_{ijij} (for $i < j$, and no sum on i or j) collect the material properties in both the x_i and x_j direction. This is based on the fact that a shear strain is applied over two faces instead of one and therefore is affected by material boundaries in both of these directions.

6.1.2 Determine the Effectiveness of the MVEs

In the latter part of Chapter Four (Section 4.3 and onwards), the four MVEs were used to estimate the material properties of simple cuboid geometries, each developed to individually test a certain aspect of the MVEs. The first test, the volume fraction test, sought to predict how the MVEs react to the placement of a material boundary within the element. Three sets of composite materials were tested: a composite of two isotropic materials, a composite of one isotropic and one transversely isotropic material, and a composite of two orthotropic materials. The STC-MVE produced the lowest error overall on all three cases, consistently providing an error of about 2% or less. The TMC-MVE also performed admirably, dropping the error on the similarly performing ASE and B-MVE to acceptable levels. The STC-MVE vastly improved upon the calculation of the shear stiffness components.

The material angle test looked to test the MVEs on a composite material of an isotropic material and a transversely isotropic material rotated at different angles out of the principal frame. Again, both the TMC-MVE and STC-MVE overall were the most accurate as compared to the true finite element result. The error for the transverse shear stiffness terms C_{1313} and C_{1212} were both higher in this study, but the

STC–MVE was still the most accurate for these terms, dropping the error to under 10%.

The boundary angle study aimed to determine the accuracy of the MVEs when used to analyze geometries with material boundaries that are not parallel to a coordinate axis. Outside the shear stiffness terms C_{1313} and C_{1212} , the TMC–MME was consistently under a 4% error, and the STC–MME was consistently under 3% error, with most terms being under 1%. All MVEs had high error for the shear stiffness terms C_{1313} and C_{1212} , but the STC–MVE was the only MVE to calculate both terms under a 30% error.

In Chapter Five, the MVEs were used to predict the properties of a plain weave fiber composite lamina, and the results were compared with the results provided from a fully meshed traditional finite element model in commercial code and experimental results provided by Scida *et al.* [3]. The results showed that all of the MVEs provided results that were reasonable, ranging from less than 1% to about 14% error as compared against the reference finite element model. However, the STC–MVE predicted all stiffness terms with less than a 3% error, with most terms being under 1% error.

Therefore, it has been shown that the newly presented STC–MVE is the most accurate MVE of the MVEs compared in this study, with the newly presented TMC–MVE also performing well.

6.1.3 Expose the Shortcomings

As these tests were performed, a few shortcomings of all the MVEs in their present formulations were discovered that were not corrected with the construction of the TMC–MVE or the STC–MVE. These shortcomings help provide a basis for recommendations for future work.

- In the volume fraction study from Chapter Four, the tests on the three different material systems showed that the MVEs are sensitive to the ratio of the constituent materials' stiffness properties. Namely, the larger the difference between the properties of two materials contained within an MVE, the less accurate the MVEs are.
- In the material angle study from Chapter Four, the error for the anisotropic stiffness term C_{2313} was calculated. It was determined from this example calculation that the MVE is sensitive to anisotropic behavior.
- In most studies performed in both Chapters Four and Five, the transverse shear stiffness terms were often the least accurate of the stiffness terms calculated, often by a large margin. The STC-MVE was usually the most accurate of the four MVEs.

6.2 Recommendations for Future Work

In this section, recommendations for future work on this research will be presented. Namely, recommendations on how to improve the theory of MVEs itself, the testing of the MVEs, and the MATLAB code used in the research will be provided.

This section starts with a review of the extended finite element method (XFEM). Both MVEs and XFEM share a similar goal of being able to impose discontinuities within the domain of a finite element, so there is potentially a way to utilize the methods from both areas to help construct a more accurate way of including discontinuities within the element domain.

6.2.1 The Extended Finite Element Method

As briefly discussed in Chapter Two, the extended finite element method (XFEM) is an extension upon standard finite element methods that utilize “enrichment functions” that allow for greater resolution within the element. This technique

allows discontinuities, such as cracks or material boundaries, to exist within an element without the addition of more nodes; rather, the nodes are enriched through the addition of extra degrees of freedom.

A brief discussion of the theory behind XFEM is provided here as an extension to the material provided in Chapter Three; for a more in-depth discussion of the methods of XFEM, see [66]. In addition, some applications to composite materials from literature will be presented; for further discussion on XFEM in regards to material modeling, see [68].

6.2.1.1 Theory. The mathematical basis for the XFEM process is the partition of unity method, first proposed by Melenk and Babuška [69]. As summarized in Belytschko *et al.* [68], the partition of unity is a set of functions $\psi_i(\mathbf{x})$ in a domain Ω that represent a partitioning of unity (i.e., one) such that

$$\sum_{i \in I} \psi_i(\mathbf{x}) = 1, \quad \forall \mathbf{x} \in \Omega \quad (6.1)$$

where I represents all nodes in Ω . These functions, which are usually the standard Lagrangian interpolation functions used in standard finite elements, can be multiplied by an enrichment function $\Phi(\mathbf{x})$ and summed over $i \in I$, which will just return the enrichment function. However, after the introduction of an unknown parameter q_i , this summation can be modified. All three of these components constitute the nodal enrichment \mathbf{u}^{enr} , which is added to the standard finite element displacement \mathbf{u}^{FE} from Equation (3.14) to approximate the global displacement function $\mathbf{u}(\mathbf{x})$ as [66, 68]

$$\mathbf{u}(\mathbf{x}) = \underbrace{\sum_{i \in I} u_i \psi_i(\mathbf{x})}_{\mathbf{u}^{\text{FE}}} + \underbrace{\sum_{i \in I} q_i \psi_i(\mathbf{x}) \Phi(\mathbf{x})}_{\mathbf{u}^{\text{enr}}} \quad (6.2)$$

where u_i refers to the i^{th} nodal displacement in Ω . Note that both u_i and q_i are unknowns; nodal enrichment adds a set of degrees of freedom. The application of

this form was first performed by Belytschko and Black for crack growth in elastic media [73], where $\Phi(\mathbf{x})$ was used to describe the near-tip displacement field for Mode I and II failure.

Because the approximation of $\mathbf{u}(\mathbf{x})$ is the summation of \mathbf{u}^{FE} and \mathbf{u}^{enr} , valid interpolation functions $\psi_i(\mathbf{x})$ from traditional finite elements are also valid in XFEM. The MVEs developed in Chapter Four can therefore be used in XFEM as well.

The form for \mathbf{u}^{enr} in Equation (6.2) is inconvenient as, in general, $u_i(\mathbf{x}_i) \neq u_i$, where \mathbf{x}_i is a nodal location [66]. This is because $\Phi(\mathbf{x})$ does not disappear at the nodal locations. While this could be solved by enriching every node in Ω , this is computationally inefficient since it doubles the number of degrees of freedom for the entire system, especially considering $\Phi(\mathbf{x})$ is a local phenomenon. Belytschko *et al.* [70] suggested subtracting off $\Phi(\mathbf{x}_i)$, the value of the function evaluated at each nodal location, before multiplying it into the enrichment function as a means to get the enrichment function to disappear at each nodal location. It was shown this reproduces $\Phi(\mathbf{x})$ exactly. Therefore, the enrichment function now only has to be applied to the subset of nodes $I^* \subset I$ that need to be enriched because of the application of $\Phi(\mathbf{x})$; this is done as [66]

$$\mathbf{u}(\mathbf{x}) = \sum_{i \in I} u_i \psi_i(\mathbf{x}) + \sum_{i \in I^*} q_i \psi_i(\mathbf{x}) [\Phi(\mathbf{x}) - \Phi(\mathbf{x}_i)] \quad (6.3)$$

There are two types of discontinuities that can be modeled with XFEM. Strong discontinuities (i.e., cracks) refer to interfaces that are entirely discontinuous, meaning there is a “jump” across the interface. Weak discontinuities (i.e., material boundaries) refer to interfaces that only have discontinuous gradients, meaning there is only a “kink” across the interface [66]. The enrichment functions for these two types of discontinuities are handled differently.

Assume there is a level-set function $f(\mathbf{x})$ that is equal to zero at the discontinuity, and has opposite signs on either side of the discontinuity. For strong discontinuities, the enrichment function is the Heaviside function of this function, written as [66, 73]

$$\Phi_{\text{strong}}(\mathbf{x}) = H(f(\mathbf{x})) = \begin{cases} 0 & f(\mathbf{x}) \leq 0 \\ 1 & f(\mathbf{x}) > 0 \end{cases} \quad (6.4)$$

If an element contains the crack tip, the enrichment function changes to include the physics of the near-tip stresses. See [68, 73] for more details.

The first proposed enrichment function for weak discontinuities was simply taking the absolute value of the level-set function as [66]

$$\Phi_{\text{weak}}(\mathbf{x}) = |f(\mathbf{x})| \quad (6.5)$$

with a gradient of

$$\nabla\Phi_{\text{weak}}(\mathbf{x}) = \text{sign}(f(\mathbf{x})) \cdot \nabla f(\mathbf{x}) \quad (6.6)$$

This form, however, leads to a problem with what are termed “blending elements” [66]. Blending elements are the elements that form the boundary between enriched elements and standard elements; therefore, they often have only some nodes enriched. Blending elements are not an issue when $\Phi(\mathbf{x})$ disappears outside of elements that contain discontinuities, but this is not the case with Equation (6.5). Convergence is greatly affected by the presence of blending elements.

Fries [83] tackled this issue with the introduction of a ramp function. By multiplying the enrichment function by a localized ramp function; this served to eliminate the effect of the enrichment within the blending elements.

An alternative formulation for the enrichment function for weak discontinuities was proposed by Moës *et al.* [71], given as

$$\Phi_{\text{weak}}(\mathbf{x}) = \sum_{i \in I} |f(\mathbf{x}_i)| \psi_i(\mathbf{x}) - \left| \sum_{i \in I} f(\mathbf{x}_i) \psi_i(\mathbf{x}) \right| \quad (6.7)$$

This form of the enrichment function disappears outside of the elements that do not contain a discontinuity; therefore there is no need to provide special consideration for blending elements.

The enrichment function presented by Moës *et al.* models a general material weak discontinuity without considering the material properties of the constituent elements. A derivation similar to that of the MVEs in Chapter Four could perhaps be used to create a specialized enrichment function that can be used specifically in the structural mechanics implementation in XFEM.

As mentioned in Chapter Two, a concern with using the enrichment functions is the numerical integration [73]. As discussed previously in Chapter Three, the calculation of the stiffness matrices require numerical integration, which is traditionally done through the use of Gauss quadrature in Equation (3.45). In XFEM, the solution space is enriched with singular or discontinuous functions, and the numerical integration of these functions are inaccurate when using standard Gauss quadrature. This could pose a problem with the unification of the MVE method and XFEM, as the MVEs presented in this thesis are by definition dependent upon the use of integration points. In the list of alternatives suggested by [68], an adaptive quadrature scheme is suggested as an option; this type of quadrature can also help to refine the MVEs around the material boundaries.

6.2.1.2 Applications in Composites. With the continued development of XFEM, its application to the study of composite materials is beginning to become more common in literature. The ability of XFEM to study both crack propagation and complex internal boundaries without remeshing allows for very efficient studies in the mechanical properties and failure of composite materials. Some recent applications of XFEM to composite materials will be presented in this section.

Huynh and Belytschko [67] described the XFEM process for studying fracture in composite materials. This particular problem is interesting as both weak and strong discontinuities exist within the domain. The tests performed include a center crack on an infinite bimaterial plate, a centered crack in a slated bimaterial plate, and three-dimensional analysis of a randomly-oriented fiber composite RVE with cracks on the fiber/matrix interface. The ramp function of Fries [83] was implemented to increase accuracy. The studies found that the methodology presented has good potential for use in studying failure in composite materials; the XFEM approach showed excellent agreement with exact analytic results.

Kästner *et al.* [84] studied simple unidirectional and woven composite geometries, both infused with a polymer resin. In these studies, the fibers were modeled as isotropic and linear elastic, while the polymer resin was modeled as viscoelastic. Using XFEM, the nonlinear stress-strain curve was reproduced with good accuracy as compared to experimental results (up until the onset of failure, which was not included in the model presented). Further, a crack propagation study was presented without comparison. The methodology presented only took the local material properties and geometry into account; there was no macroscale homogenization performed. Therefore, the model provides a real prediction of how the material would react under loading.

Safdari *et al.* [85] studied an extension to XFEM where each material boundary is modeled using a non-uniform rational B-spline (NURBS). This extension, termed the NURBS-based interface enriched generalized finite element method (NIGFEM), allows complex material boundaries to be enriched using the generated NURBS surface without having to determine a level-set function to describe the material boundary; rather, the generated NURBS surface can be used to define the enrichment

function. The results showed excellent accuracy when compared with standard finite element solutions; further, the NIGFEM mesh converged faster than the standard FEM mesh.

Yazdani *et al.* [74] applied XFEM to model delamination in composite laminates. The laminates were modeled at the macroscopic level; fiber architecture was not taken into account. The XFEM process was coupled with the first-order shear deformation theory to perform the studies. Two tests were modeled: a double cantilever beam test for pure Mode I failure, and an end notched flexure test for pure Mode II failure. Both tests were calculated using different numerical integration techniques and compared with experimental results. Very good agreement with experimental results were calculated, especially considering the focus of the study was within the nonlinear regime of the interlaminar stresses.

Savvas *et al.* [86] used XFEM to study the material properties of a two dimensional composite of a matrix with circular inclusions. The RVE was generated using a Monte Carlo simulation. The purpose of the study was to determine the aspect ratio of the window size to the diameter of the inclusion required to determine the material properties of the inclusion-filled composite. XFEM helped the study be computationally efficient as no remeshing is required to study multiple RVEs. The study showed that, for an inclusion diameter of 1, a window size of about 30 is required for converging material properties.

6.2.2 Recommendations

The following recommendations are made for the STC-MVE, the overall most accurate MVE presented in this thesis:

- **Improve Transverse Shear Stiffness Prediction.** In many of the tests throughout Chapter Four, the transverse shear stiffness terms C_{1313} and C_{1212}

were often the least accurate term predicted by all of the MVEs. The formulation of the STC–MVE, through the way it calculated the strain corrections for these terms, proved to be a step in the right direction, but there is still room for improvement here.

- **Incorporate the Extension–Extension Terms.** In the current formulation of the STC–MVE, Poisson’s effect is not taken into account as the extension–extension terms (C_{1122} , C_{1133} , and C_{2233}) are neglected. The inclusion of these terms, as well as the shear–extension terms, may help to reduce the error on the MVEs.
- **Implement an Adaptive Quadrature Scheme.** Gauss quadrature uses fixed points to calculate the numerical integral. The MVE may benefit from the use of an adaptive quadrature scheme that will focus refinement of integration points around a material boundary.
- **Extend the Formulation to Other Problems.** Currently, the STC–MVE can only be used in the three–dimensional structural mechanics problems. A similar formulation could be found for other problems, such as fluid mechanics and heat transfer.
- **Conjoin the MVE methods with XFEM.** Section 6.2.1 goes into detail about the XFEM process and some current applications in literature. As both MVEs and XFEM aim to include discontinuities within an element, there may be some way to conjoin the two methods, whether by using an MVE directly with XFEM or using the derivation of the STC–MVE as a basis for a new enrichment function.

The following recommendations are made for ways to test the MVE:

- **Use a Unidirectional Fiber Model for the Volume Fraction Study.**

Nakai *et al.* [57] used a two-dimensional circular inclusion RVE to test their finite element method with changing volume fraction. This type of test is useful as it helps provide a real world analogue for the test. A similar test with unidirectional continuous fibers could be used, where the radius of the fiber is altered to change the volume fraction.

- **Use a Rotating Fiber in Matrix Model for the Material Angle Study.**

With the purpose of providing a real world analogue for the material angle study, a single rotating fiber inclusion within a matrix can be used instead.

- **Traditional Finite Element Models should be Created for Reference.**

The analysis of the MVEs for the satin and twill weave laminae was limited by the lack of a readily available finite element model on hand for use as a reference. A reference model should be created and compared to the MVEs to better determine their accuracy for those weaves.

The following recommendations are made for the MATLAB code specifically created used in this study:

- **Restructure the Code for More Efficient Memory Usage.** The analyses of the twill and satin weave composite laminae in Chapter Five were in part limited by the inefficient handling of memory. Greater use of sparse matrices, virtual memory, and iterative solvers could be explored to reduce memory costs on the MATLAB code.
- **Adapt Code for Use with Preexisting Meshes.** Software such as TexGen [7] have been developed to automatically generate and mesh the RVE of a woven composite lamina, which can be exported as an ABAQUS mesh. The ability to read these mesh files can be useful to test multiple composite laminae.
- **Adapt Code for Use With Scans of Real Geometries.** Ultrasound scans

(see e.g., [8]) and micro CT scans (see e.g., [9]) can be used to determine the weave geometry of a real composite. The ability to read this scan data and analyze it using the MVEs would allow a means to predict the properties of a real life geometry without having to explicitly model the geometry data.

APPENDICES

APPENDIX A

MATLAB Code for ASE

The following is an example element file that can be used to calculate the element stiffness matrix of the average stiffness element (ASE), similar to the volume fraction-based formulations from Kim and Swan [14] and Watanabe *et al.* [15]. The ASE is mathematically described in Equation (4.2).

```
function K = ASE(eprop,xe)
%%%%%%%%%%%%%%%%%%%%%%%%%%%%%%%%%%%%%%%%%%%%%%%%%%%%%%%%%%%%%%%%%%%%%%%%
% This is a multiphase voxel element that uses the average of the stiffness
% tensor components as the global stiffness tensor
%
% INPUTS:
% - eprop : Properties from input.dat file
% - xe    : Global locations of nodes
%
% OUTPUTS:
% - K     : Elemental Stiffness Matrix
%%%%%%%%%%%%%%%%%%%%%%%%%%%%%%%%%%%%%%%%%%%%%%%%%%%%%%%%%%%%%%%%%%%%%%%%
% Determine Gauss points from input.dat file
Ngp = eprop(3);

% Collect material information at each Gauss point from geometry file
C_all = geom(eprop,Ngp,xe);

% Average the stiffness tensor components together
Ceff = sum(sum(sum(C_all,5),4),3)/(Ngp^3);

% Change to a typical number of Gauss points
Ngp = 3;

% Pull Gauss points and corresponding weights from table
[wgt,gpt] = gaussquad_tab(Ngp);

%% Evaluate element stiffness matrix
K = zeros(24);
% Gauss integration
for m = 1:Ngp
```

```

for n = 1:Ngp
    for p = 1:Ngp
        zeta1 = gpt(m);    zeta2 = gpt(n);    zeta3 = gpt(p);

        % Derivative of interpolation functions w.r.t. zeta
        Dpsi = 1/8*[...
            -(1-zeta2)*(1-zeta3), (1-zeta2)*(1-zeta3),...
            (1+zeta2)*(1-zeta3), -(1+zeta2)*(1-zeta3),...
            -(1-zeta2)*(1+zeta3), (1-zeta2)*(1+zeta3),...
            (1+zeta2)*(1+zeta3), -(1+zeta2)*(1+zeta3);... //
            -(1-zeta1)*(1-zeta3), -(1+zeta1)*(1-zeta3),...
            (1+zeta1)*(1-zeta3), (1-zeta1)*(1-zeta3),...
            -(1-zeta1)*(1+zeta3), -(1+zeta1)*(1+zeta3),...
            (1+zeta1)*(1+zeta3), (1-zeta1)*(1+zeta3);... //
            -(1-zeta1)*(1-zeta2), -(1+zeta1)*(1-zeta2),...
            -(1+zeta1)*(1+zeta2), -(1-zeta1)*(1+zeta2),...
            (1-zeta1)*(1-zeta2), (1+zeta1)*(1-zeta2),...
            (1+zeta1)*(1+zeta2), (1-zeta1)*(1+zeta2)];

        % Calculate the Jacobian
        Jac = Dpsi*xe;    % Jacobian
        detJ = det(Jac);    % Det(J)
        DpsiX = Jac\Dpsi;    % d(psi)/dx

        % Form strain-displacement matrix
        B = zeros(6,24);
        for ii = 1:8
            B(:,(3*ii-2):(3*ii)) = ...
                [DpsiX(1,ii),0,0,0,0,0;...
                0,DpsiX(2,ii),0,0,0,0;...
                0,0,DpsiX(3,ii),0,0,0;...
                0,DpsiX(3,ii),DpsiX(2,ii),0,0,0;...
                DpsiX(3,ii),0,DpsiX(1,ii),0,0,0;...
                DpsiX(2,ii),DpsiX(1,ii),0,0,0,0];
        end
        % Form K matrix using average stiffness tensor
        K = K + B'*Ceff*B*detJ*wgt(m)*wgt(n)*wgt(p);
    end
end
end
end
end

```

APPENDIX B

MATLAB Code for B-MVE

The following is an example element file that can be used to calculate the element stiffness matrix of the basic multiphase voxel element (B-MVE) as presented in Lippmann *et al.* [11] and Zeng *et al.* [12]. The mathematical form is expressed in Equation (4.3)

```
function K = B_MVE(eprop,xe)
%%%%%%%%%%%%%%%%%%%%%%%%%%%%%%%%%%%%%%%%%%%%%%%%%%%%%%%%%%%%%%%%%%%%%%%%
% This is a basic multiphase voxel element that applies the material
% properties at each Gauss point. From Zeng, et al.
%
% INPUTS:
%   - eprop : Properties from input.dat file
%   - xe     : Global locations of nodes
%
% OUTPUTS:
%   - K      : Elemental Stiffness Matrix
%%%%%%%%%%%%%%%%%%%%%%%%%%%%%%%%%%%%%%%%%%%%%%%%%%%%%%%%%%%%%%%%%%%%%%%%

Ngp = eprop(3);           % Determine Gauss points from input.dat file
[wgt,gpt] = gaussquad_tab(Ngp); % Pull Gauss points and corresponding
                               weights from table

% Collect material information at each Gauss point from geometry file
C_all = geom(eprop,Ngp,xe);

%% Evaluate element stiffness matrix
K = zeros(24);
% Gauss integration
for m = 1:Ngp
    for n = 1:Ngp
        for p = 1:Ngp
            zeta1 = gpt(m);    zeta2 = gpt(n);    zeta3 = gpt(p);

            % Derivative of interpolation functions w.r.t. zeta
            Dpsi = 1/8*[...
```

```

        -(1-zeta2)*(1-zeta3), (1-zeta2)*(1-zeta3),...
        (1+zeta2)*(1-zeta3), -(1+zeta2)*(1-zeta3),...
        -(1-zeta2)*(1+zeta3), (1-zeta2)*(1+zeta3),...
        (1+zeta2)*(1+zeta3), -(1+zeta2)*(1+zeta3);... //
        -(1-zeta1)*(1-zeta3), -(1+zeta1)*(1-zeta3),...
        (1+zeta1)*(1-zeta3), (1-zeta1)*(1-zeta3),...
        -(1-zeta1)*(1+zeta3), -(1+zeta1)*(1+zeta3),...
        (1+zeta1)*(1+zeta3), (1-zeta1)*(1+zeta3);... //
        -(1-zeta1)*(1-zeta2), -(1+zeta1)*(1-zeta2),...
        -(1+zeta1)*(1+zeta2), -(1-zeta1)*(1+zeta2),...
        (1-zeta1)*(1-zeta2), (1+zeta1)*(1-zeta2),...
        (1+zeta1)*(1+zeta2), (1-zeta1)*(1+zeta2)];

% Calculate the Jacobian
Jac = Dpsi*xe;      % Jacobian
detJ = det(Jac);   % Det(J)
DpsiX = Jac\Dpsi;  % d(psi)/dx

% Form strain-displacement matrix
B = zeros(6,24);
for ii = 1:8
    B(:,(3*ii-2):(3*ii)) = ...
        [DpsiX(1,ii),0           ,0           ;...
         0           ,DpsiX(2,ii),0           ;...
         0           ,0           ,DpsiX(3,ii);...
         0           ,DpsiX(3,ii),DpsiX(2,ii);...
         DpsiX(3,ii),0           ,DpsiX(1,ii);...
         DpsiX(2,ii),DpsiX(1,ii),           0];
end
% Form K matrix
K = K + B'*C_all(:, :, m, n, p)*B*detJ*wgt(m)*wgt(n)*wgt(p);
end
end
end
end
end
end

```

APPENDIX C

MATLAB Code for TMC-MVE

The following is the element file used to calculate the element stiffness matrix of the tensile modulus corrected multiphase voxel element (TMC-MME) based on the element presented in Caselman [1]. The mathematical form is found in Equation (4.18).

```
function K = TMC_MVE(eprop,xe)
%%%%%%%%%%%%%%%%%%%%%%%%%%%%%%%%%%%%%%%%%%%%%%%%%%%%%%%%%%%%%%%%%%%%%%%%
% This is a multiphase voxel that uses the tensile modulus in each
% orthogonal direction to calculate strain correction factors. Based on a
% method of Caselman
%
% INPUTS:
% - eprop : Properties from input.dat file
% - xe    : Global locations of nodes
%
% OUTPUTS:
% - K     : Elemental Stiffness Matrix
%%%%%%%%%%%%%%%%%%%%%%%%%%%%%%%%%%%%%%%%%%%%%%%%%%%%%%%%%%%%%%%%%%%%%%%%

Ngp = eprop(3); % Determine Gauss points from input.dat file
[wgt,gpt] = gaussquad_tab(Ngp); % Pull Gauss points and corresponding
                                weights from table

% Collect material information at each Gauss point from geometry file
[C_all,Ex,Ey,Ez] = geom(eprop,Ngp,xe);

% Invert Tensile Moduli
Exi = 1./Ex;
Eyi = 1./Ey;
Ezi = 1./Ez;

%% Evaluate element stiffness matrix
K = zeros(24);
% Gauss Integration
for m = 1:Ngp
```

```

for n = 1:Ngp
    for p = 1:Ngp
        zeta1 = gpt(m);    zeta2 = gpt(n);    zeta3 = gpt(p);
        Cpt = C_all(:, :, m, n, p);

        % Derivative of interpolation functions w.r.t. zeta
        Dpsi = 1/8*[...
            -(1-zeta2)*(1-zeta3), (1-zeta2)*(1-zeta3), ...
            (1+zeta2)*(1-zeta3), -(1+zeta2)*(1-zeta3), ...
            -(1-zeta2)*(1+zeta3), (1-zeta2)*(1+zeta3), ...
            (1+zeta2)*(1+zeta3), -(1+zeta2)*(1+zeta3); ... //
            -(1-zeta1)*(1-zeta3), -(1+zeta1)*(1-zeta3), ...
            (1+zeta1)*(1-zeta3), (1-zeta1)*(1-zeta3), ...
            -(1-zeta1)*(1+zeta3), -(1+zeta1)*(1+zeta3), ...
            (1+zeta1)*(1+zeta3), (1-zeta1)*(1+zeta3); ... //
            -(1-zeta1)*(1-zeta2), -(1+zeta1)*(1-zeta2), ...
            -(1+zeta1)*(1+zeta2), -(1-zeta1)*(1+zeta2), ...
            (1-zeta1)*(1-zeta2), (1+zeta1)*(1-zeta2), ...
            (1+zeta1)*(1+zeta2), (1-zeta1)*(1+zeta2)];

        % Calculate the Jacobian
        Jac = Dpsi*x;    % Jacobian
        detJ = det(Jac);    % Det(J)
        DpsiX = Jac\Dpsi;    % d(psi)/dx

        % Collect E_11 in x_1 direction
        EiX = zeros(1,Ngp);
        EiX(1,:) = Exi(:,n,p);

        % Collect E_22 in x_2 direction
        EiY = zeros(1,Ngp);
        EiY(1,:) = Eyi(m,:,p);

        % Collect E_33 in x_3 direction
        EiZ = zeros(1,Ngp);
        EiZ(1,:) = Ezi(m,n,:);

        % Calculate E_eff in each direction, using wgt/2 as beta
        % value.
        EeffX = 2/(EiX*wgt);
        EeffY = 2/(EiY*wgt);
        EeffZ = 2/(EiZ*wgt);

        % Calculate Strain Correction Factors
        corX = EeffX*Exi(m,n,p);

```

```

corY = EeffY*Eyi(m,n,p);
corZ = EeffZ*Ezi(m,n,p);

% Form strain-displacement matrix using corrections
B = zeros(6,24);
for ii = 1:8
    B(:,(3*ii-2):(3*ii)) = ...
        [corX*DpsiX(1,ii),0,0,0,0,0;...
         0,corY*DpsiX(2,ii),0,0,0,0;...
         0,0,corZ*DpsiX(3,ii);...
         0,corZ*DpsiX(3,ii),corY*DpsiX(2,ii);...
         corZ*DpsiX(3,ii),0,corX*DpsiX(1,ii);...
         corY*DpsiX(2,ii),corX*DpsiX(1,ii),0];
end
% Form K matrix
K = K + B'*Cpt*B*detJ*wgt(m)*wgt(n)*wgt(p);
end
end
end
end

```

APPENDIX D

MATLAB Code for STC–MVE

The following is the element file used to calculate the element stiffness matrix of the stiffness tensor corrected multiphase voxel element (STC–MVE) described in Table 4.1.

```
function K = STC_MVE(eprop,xe)
%%%%%%%%%%%%%%%%%%%%%%%%%%%%%%%%%%%%%%%%%%%%%%%%%%%%%%%%%%%%%%%%%%%%%%%%
% This is a multiphase voxel element that uses the stiffness tensor
% components to calculate strain correction factors.
%
% INPUTS:
%   - eprop : Properties from input.dat file
%   - xe    : Global locations of nodes
%
% OUTPUTS:
%   - K     : Elemental Stiffness Matrix
%%%%%%%%%%%%%%%%%%%%%%%%%%%%%%%%%%%%%%%%%%%%%%%%%%%%%%%%%%%%%%%%%%%%%%%%

Ngp = eprop(3); % Determine Gauss points from input.dat file
[wgt,gpt] = gaussquad_tab(Ngp); % Pull Gauss points and corresponding
                                weights from table

% Collect material information at each Gauss point from geometry file
C_all = geom(eprop,Ngp,xe);

%% Evaluate element stiffness matrix
K = zeros(24);
% Gauss integration
for m = 1:Ngp
    for n = 1:Ngp
        for p = 1:Ngp
            zeta1 = gpt(m);    zeta2 = gpt(n);    zeta3 = gpt(p);
            Ceff = zeros(6,1);
            Cpt = C_all(:, :, m, n, p);

            % Derivative of interpolation functions w.r.t. zeta
            Dpsi = 1/8*[...
```

```

    -(1-zeta2)*(1-zeta3), (1-zeta2)*(1-zeta3),...
    (1+zeta2)*(1-zeta3), -(1+zeta2)*(1-zeta3),...
    -(1-zeta2)*(1+zeta3), (1-zeta2)*(1+zeta3),...
    (1+zeta2)*(1+zeta3), -(1+zeta2)*(1+zeta3);... //
    -(1-zeta1)*(1-zeta3), -(1+zeta1)*(1-zeta3),...
    (1+zeta1)*(1-zeta3), (1-zeta1)*(1-zeta3),...
    -(1-zeta1)*(1+zeta3), -(1+zeta1)*(1+zeta3),...
    (1+zeta1)*(1+zeta3), (1-zeta1)*(1+zeta3);... //
    -(1-zeta1)*(1-zeta2), -(1+zeta1)*(1-zeta2),...
    -(1+zeta1)*(1+zeta2), -(1-zeta1)*(1+zeta2),...
    (1-zeta1)*(1-zeta2), (1+zeta1)*(1-zeta2),...
    (1+zeta1)*(1+zeta2), (1-zeta1)*(1+zeta2)];

% Calculate the Jacobian
Jac = Dpsi*xe;      % Jacobian
detJ = det(Jac);   % Det(J)
DpsiX = Jac\Dpsi;  % d(psi)/dx

% Initialize "spring" property vectors
C11 = zeros(1,Ngp);      % C_1111
C22 = zeros(1,Ngp);      % C_2222
C33 = zeros(1,Ngp);      % C_3333
C44_2 = zeros(1,Ngp);    % C_2323 in x_2
C44_3 = zeros(1,Ngp);    % C_2323 in x_3
C55_1 = zeros(1,Ngp);    % C_1313 in x_1
C55_3 = zeros(1,Ngp);    % C_1313 in x_3
C66_1 = zeros(1,Ngp);    % C_1212 in x_1
C66_2 = zeros(1,Ngp);    % C_1212 in x_2

% Calculate C_1111 Eff in x_1
C11(1,:) = 1./C_all(1,1,:,n,p);
Ceff(1) = (1/2*C11*wgt)^-1;

% Calculate C_2222 Eff in x_2
C22(1,:) = 1./C_all(2,2,m,:,p);
Ceff(2) = (1/2*C22*wgt)^-1;

% Calculate C_3333 Eff in x_3
C33(1,:) = 1./C_all(3,3,m,n,:);
Ceff(3) = (1/2*C33*wgt)^-1;

% Calculate C_2323 Eff in x_2/x_3
C44_2(1,:) = 1./C_all(4,4,m,:,p);
C44_3(1,:) = 1./C_all(4,4,m,n,:);
C44 = (C44_2+C44_3)./2;

```

```

Ceff(4) = (1/2*C44*wgt)^-1;

% Calculate C_1313 Eff in x_1/x_3
C55_1(1,:) = 1./C_all(5,5,:,n,p);
C55_3(1,:) = 1./C_all(5,5,m,n,:);
C55 = (C55_1+C55_3)./2;
Ceff(5) = (1/2*C55*wgt)^-1;

% Calculate C_1212 Eff in x_1/x_2
C66_1(1,:) = 1./C_all(6,6,:,n,p);
C66_2(1,:) = 1./C_all(6,6,m,:,p);
C66 = (C66_1+C66_2)./2;
Ceff(6) = (1/2*C66*wgt)^-1;

% Calculate strain correction factors
corX = Ceff(1)/Cpt(1,1);
corY = Ceff(2)/Cpt(2,2);
corZ = Ceff(3)/Cpt(3,3);
corYZ = Ceff(4)/Cpt(4,4);
corXZ = Ceff(5)/Cpt(5,5);
corXY = Ceff(6)/Cpt(6,6);

% Form strain-displacement matrix using corrections
B = zeros(6,24);
for ii = 1:8
    B(:,(3*ii-2):(3*ii)) = ...
        [DpsiX(1,ii)*corX,0,0,0,0,0;...
         0,DpsiX(2,ii)*corY,0,0,0,0;...
         0,0,DpsiX(3,ii)*corZ;...
         0,corYZ*DpsiX(3,ii),corYZ*DpsiX(2,ii);...
         corXZ*DpsiX(3,ii),0,corXZ*DpsiX(1,ii);...
         corXY*DpsiX(2,ii),corXY*DpsiX(1,ii),0];
end
% Form K matrix
K = K + B'*Cpt*B*detJ*wgt(m)*wgt(n)*wgt(p);
end
end
end
end

```

BIBLIOGRAPHY

- [1] E. Caselman. Elastic property prediction of short fiber composites using a uniform mesh finite element method. Master's thesis, University of Missouri - Columbia, December 2007.
- [2] C.T. Sun and R.S. Vaidya. Prediction of composite properties from a representative volume element. *Compos Sci Technol*, **56**(2):171–179, 1996.
- [3] D. Scida, Z. Aboura, M.L. Benzeggagh, and E. Bocherens. A micromechanics model for 3D elasticity and failure of woven-fibre composite materials. *Compos Sci Technol*, **59**(14):505–517, 1999.
- [4] A. Barnes. *Pernambuco vs. Carbon Fiber Bows*. Shar Music Blog. Accessed: June 26, 2016, <http://blog.sharmusic.com/>.
- [5] T.M. Mase, R.S. Smelser, and G.E. Mase. *Continuum Mechanics for Engineers*. CNC Press, Boca Raton, FL, third edition, 2010.
- [6] R.M. Jones. *Mechanics of Composite Materials*. Taylor and Francis, Inc., Philadelphia, PA, second edition, 1999.
- [7] H. Lin, X. Zeng, M. Sherburn, A.C. Long, and M.J. Clifford. Automated geometric modelling of textile structures. *Text Res J*, **82**(16):1689–1702, 2011.
- [8] S. Stair, D.A. Jack, and J. Fitch. Non-destructive characterization of ply orientation and ply type of carbon fiber reinforced laminated composites. In *Proceedings of 14th Annual Automotive Composites Conference and Exhibition*. Society of Plastics Engineers, September 2014.
- [9] S. Goris and T.A. Osswald. Fiber orientation measurements using a novel image processing algorithm for micro-computed tomography scans. In *Proceedings of 15th Annual Automotive Composites Conference and Exhibition*. Society of Plastics Engineers, September 2015.
- [10] J. Middleton. Elastic property prediction of long fiber composites using a uniform mesh finite element method. Master's thesis, University of Missouri - Columbia, August 2008.
- [11] N. Lippmann, Th. Steinkopff, S. Schmauder, and P. Gumbsch. 3D-finite-element-modelling of microstructures with the method of multiphase elements. *Comp Mater Sci*, **9**(1):28–35, 1997.
- [12] T. Zeng, L.-Z. Wu, and L.-C. Guo. Mechanical analysis of 3d braided composites: a finite element model. *Compos Struct*, **64**(3):399–404, 2004.

- [13] D. Scida, Z. Aboura, M.L. Benzeggagh, and E. Bocherens. Prediction of the elastic behaviour of hybrid and non-hybrid woven composites. *Compos Sci Technol*, **57**(12):1727–1740, 1998.
- [14] H.J. Kim and C.C. Swan. Voxel-based meshing and unit-cell analysis of textile composites. *Int J Numer Meth Engng*, **56**(7):977–1006, 2003.
- [15] K. Watanabe, Y. Iijima, K. Kawano, and H. Igarashi. Voxel based finite element method using homogenization. *IEEE T Magn*, **48**(2):543–546, 2012.
- [16] N. ElAgamy and J. Laliberté. Historical development of geometric modelling of textiles reinforcements for polymer composites: A review. *J Ind Text*, **45**(4):556–584, 2016.
- [17] Americal Society for Testing and Materials. *ASTM D3039-14 Standard Test Method for Tensile Properties of Polymer Matrix Composite Materials*, 2014.
- [18] T. Ishikawa and T.-W. Chou. Elastic behaviour of woven hybrid composites. *J Compos Mater*, **16**(1):2–19, 1982.
- [19] G.P. Tandon and G.J. Weng. The effect of aspect ratio of inclusions on the elastic properties of unidirectionally aligned composites. *Polym Composite*, **5**(4):327–333, 1984.
- [20] J.C. Halpin. Stiffness and expansion estimates for oriented short fiber composites. *J Compos Mater*, **3**(4):732–734, 1969.
- [21] C.L. Tucker and E. Liang. Stiffness predictions for unidirectional short-fiber composites: review and evaluation. *Compos Sci Technol*, **59**(5):655–671, 1999.
- [22] T. Mori and K. Tanaka. Average stress in matrix and average elastic energy of materials with misfitting inclusions. *Acta Metall Mater*, **21**(5):571–574, May 1973.
- [23] J.D. Eshelby. The determination of the elastic field of an ellipsoidal inclusion, and related problems. *P Roy Soc Lond A Mat*, **241**(1226):376–396, 1957.
- [24] A. Gusev, H.R. Lusti, and P.J. Hine. Stiffness and thermal expansion of short fiber composites with fully aligned fibers. *Adv Eng Mater*, **4**(12):927–930, 2002.
- [25] Z. Xia, Y. Zhang, and F. Ellyin. A unified periodical boundary conditions for representative volume elements of composites and applications. *Int J Solids and Struct*, **40**(8):1907–1921, 2003.
- [26] J.J. Crookston, A.C. Long, and I.A. Jones. A summary review of mechanical properties prediction methods for textile reinforced polymer composites. *P I Mech Eng L-J Mat*, **219**(2):91–109, 2005.

- [27] A. Dixit and S.H. Mali. Modeling techniques for predicting the mechanical properties of woven-fabric textile composites: a review. *Mech Compos Mater*, **49**(1):1–20, 2013.
- [28] A.G. Prodromou, S.V. Lomov, and I. Verpoest. The method of cells and the mechanical properties of textile composites. *Compos Struct*, **93**(4):1290–1299, 2011.
- [29] J. Lua. Thermal-mechanical cell model for unbalanced plain weave woven fabric composites. *Compos Part A-Appl S*, **38**(3):1019–1037, 2007.
- [30] Z.H. Zuo and Y.M. Xie. Maximizing the effective stiffness of laminate composites. *Comp Mater Sci*, **83**:57–63, 2014.
- [31] T. Ishikawa. Anti-symmetric elastic properties of composite plates of satin weave cloth. *Fibre Sci Technol*, **15**(2):127–145, 1981.
- [32] T. Ishikawa and T.-W. Chou. Stiffness and strength behaviour of woven fabric composites. *J Mater Sci*, **17**(11):3211–3220, 1982.
- [33] T. Ishikawa and T.-W. Chou. One-dimensional micromechanical analysis of woven fabric composites. *AIAA J*, **21**(12):1714–1721, 1983.
- [34] T. Ishikawa, M. Matsushima, Y. Hayashi, and T.-W. Chou. Experimental confirmation of the theory of elastic moduli of fabric composites. *J Compos Mater*, **19**(5):443–458, 1985.
- [35] I.S. Raju and J.T. Wang. Classical laminate theory models for woven fabric composites. *J Compos Tech Res*, **16**(4):289–303, 1994.
- [36] N.K. Naik and P.S. Shembekar. Elastic behavior of woven fabric composites: I - Lamina analysis. *J Compos Mater*, **26**(15):2196–2225, 1992.
- [37] N.K. Naik and V.K. Ganesh. An analytic method for plain weave fabric composites. *Composites*, **26**(4):281–289, 1995.
- [38] Ph. Vandeurzen, J. Ivens, and I. Verpoest. A three-dimensional micromechanical analysis of woven-fabric composite: I. Geometric analysis. *Compos Sci Technol*, **56**(11):1303–1315, 1996.
- [39] J. Aboudi. Micromechanical analysis of composites by the method of cells. *Appl Mech Rev*, **42**(7):193–221, 1989.
- [40] Ph. Vandeurzen, J. Ivens, and I. Verpoest. A three-dimensional micromechanical analysis of woven-fabric composite: II. Elastic analysis. *Compos Sci Technol*, **56**(11):1317–1327, 1996.
- [41] Ph. Vandeurzen, J. Ivens, and I. Verpoest. Micro-stress analysis of woven fabric composites by multilevel decomposition. *J Compos Mater*, **32**(7):623–651, 1998.

- [42] B. Liu, X. Feng, and S.-M. Zhang. The effective Young's modulus of composites beyond the Voigt estimation due to the Poisson effect. *Comp Sci Technol*, **69**(13):2198–2204, 2009.
- [43] H. Thom. Finite element modeling of plain weave composites. *J Compos Mater*, **33**(16):1491–1510, 1999.
- [44] C. Chapman and J.D. Whitcomb. Effect of assumed tow architecture on predicted moduli and stresses in plain weave composites. *J Compos Mater*, **29**(16):2134–2159, 1995.
- [45] R. Tanov and A. Taibei. Computationally efficient micromechanical models for woven fabric composite elastic moduli. *J Appl Mech*, **68**(4):553–560, 2001.
- [46] Stig, F. and Hallström, S. Spatial modelling of 3D-woven textiles. *Compos Struct*, **94**(5):1495–1502, 2012.
- [47] I. Verpoest and S.V. Lomov. Virtual textile composites software WiseTex: Integration with micro-mechanical, permeability and structural analysis. *Compos Sci Technol*, **65**(15):2563–2574, 2005.
- [48] H. Lin, M.J. Clifford, A.C. Long, K. Lee, and N. Guo. A finite element approach to the modelling of fabric mechanics and its application to virtual fabric design and testing. *J Text Inst*, **103**(10):1063–1076, 2012.
- [49] K. Woo and J.D. Whitcomb. Macro finite element using subdomain integration. *Commun Numer Methods Eng*, **9**(12):937–949, 1993.
- [50] J.D. Whitcomb, K. Woo, and S. Gundapaneni. Macro finite element for analysis of textile composites. *J Compos Mater*, **28**(7):607–618, 1994.
- [51] J.D. Whitcomb and K. Woo. Enhanced direct stiffness method for finite element analysis of textile composites. *Compos Struct*, **28**(4):385–390, 1994.
- [52] K.S. Maxwell and J.D. Whitcomb. Evaluation of macro finite elements for use in global/local analysis of textile composites. *J Compos Sci*, **46**(9):1111–1125, 2011.
- [53] B.N. Cox, W.C. Carter, and N.A. Fleck. A binary model of textile composites: I. Formulation. *Acta Metall Mater*, **42**(10):3436–3479, 1994.
- [54] J. Xu, B.N. Cox, M.A. McGlockton, and W.C. Carter. A binary model of textile composites: II. The elastic regime. *Acta Metall Mater*, **43**(9):3511–3524, 1995.
- [55] L. Chen, X.M. Tao, and C.L. Choy. Mechanical analysis of 3-D braided composites by the finite multiphase element method. *Compos Sci Technol*, **59**(15):2383–2391, 1999.
- [56] Y. Wang and X. Sun. Digital-element simulation of textile processes. *Compos Sci Technol*, **61**(2):311–319, 2001.

- [57] H. Nakai, T. Kurashiki, and M. Zako. Individual modeling of composite materials with mesh superposition method under periodic boundary condition. In *Proceedings of 16th International Conference on Composite Materials*. International Committee on Composite Materials, July 2007.
- [58] E.V. Iarve, D.H. Mollenhauer, E.G. Zhou, T. Breitzman, and T.J. Whitney. Independent mesh method-based prediction of local and volume average fields in textile composites. *Compos Part A-Appl S*, **40**(2):1880–1890, 2009.
- [59] J. Gager and H.E. Pettermann. Numerical homogenization of textile composites based on shell element discretization. *Compos Sci Technol*, **72**(7):806–812, 2012.
- [60] T. Sato, K. Watanabe, and H. Igarashi. Accuracy evaluation of three-dimensional fe analysis based on nonconforming voxel element. *COMPEL*, **33**(1/2):181–190, 2013.
- [61] S.A. Smitheman, I.A. Jones, and W. Ruijter. A voxel-based homogenization technique for the unit cell thermomechanical analysis of woven composites. In *Proceedings of the 17th International Conference on Composite Materials (ICCE-17)*. British Composites Society, July 2009.
- [62] A. Doitrand, C. Fagiano, F.-X. Irisarri, and M. Hirsekorn. Comparison between voxel and consistent meso-scale models of woven composites. *Compos Part A-Appl S*, **73**:143–154, 2015.
- [63] G. Fang, B. El Said, D. Ivanov, and S.R. Hallett. Smoothing artificial stress concentrations in voxel-based models of textile composites. *Compos Part A-Appl S*, **80**:270–284, 2016.
- [64] T. Zeng, L.-Z. Wu, and L.-C. Guo. Predicting the nonlinear response and failure of 3D braided composites. *Mater Lett*, **58**(26):3237–3241, 2004.
- [65] D.E. Smith. Computing elastic properties of short- and long-random fiber composites using a multi-gauss point finite element method. In *Proceedings of 24th Annual Technical Conference of the American Society for Composites*, volume 2, pages 1262–1278. American Society for Composites, September 2009.
- [66] T.-P. Fries and T. Belytschko. The extended/generalized finite element method: An overview of the method and its applications. *Int J Numer Meth Engng*, **84**(3):253–304, 2010.
- [67] D.B.P. Huynh and T. Belytschko. The extended finite element method for fracture in composite materials. *Int J Numer Meth Engng*, **77**(2):214–239, 2009.
- [68] T. Belytschko, R. Gracie, and G. Ventura. A review of extended/generalized finite element methods for material modeling. *Model Simul Mater Sci*, **17**(4):043001, 2009.

- [69] J.M. Melenk and I. Babuška. The partition of unity finite element method: Basic theory and applications. *Comput Method Appl Mech Engng*, **139**(1):289–314, 1996.
- [70] Belytschko, T. and Moës, N. and Usui, S. and Parimi, C. Arbitrary discontinuities in finite elements. *Int J Numer Meth Engng*, **50**(4):993–1013, 2001.
- [71] Moës, N. and Cloirec, M. and Cartraud, P. and Remacle, J.-F. A computational approach to handle complex microstructure geometries. *Comput Method Appl Mech Engng*, **192**(28):3163–3177, 2003.
- [72] W.D. Lian, G. Legrain, and P. Cartraud. Image-based computational homogenization and localization comparison between X-FEM/levelset and voxel-based approaches. *Comput Mech*, **51**(3):279–293, 2013.
- [73] T. Belytschko and T. Black. Elastic crack growth in finite elements with minimal remeshing. *Int J Numer Meth Engng*, **45**(5):601–620, 1999.
- [74] S. Yazdani, W.J.H. Rust, and P. Wriggers. An XFEM approach for modelling delamination in composite laminates. *Compos Struct*, **135**:353–364, 2016.
- [75] J.N. Reddy. *An Introduction to the Finite Element Method*. McGraw-Hill, New York, NY, third edition, 2006.
- [76] S.C. Chapra. *Applied Numerical Methods with MATLAB for Engineers and Scientists*. McGraw-Hill, New York, NY, third edition, 2012.
- [77] V.-D. Nguyen, E. Béchet, C. Geuzaine, and L Noels. Imposing periodic boundary condition on arbitrary meshes by polynomial interpolation. *Comp Mater Sci*, **55**:390–406, 2012.
- [78] I.M. Ward. Optical and mechanical anisotropy in crystalline polymers. *P Phys Soc*, **80**(5):1176–1188, 1962.
- [79] MathWorks. *MATLAB Coder: Generate C and C++ code from MATLAB code*. Accessed: June 20, 2016, <http://www.mathworks.com/>.
- [80] HEXCEL Corporation. *HexForce® Reinforcements: Technical Fabrics Handbook*. Accessed: July 12, 2016, <http://www.hexcel.com/>.
- [81] COMSOL Discussion Forum. *The periodic boundary condition and PML question about COMOL 4*. Accessed: June 22, 2016, <https://www.comsol.com/>.
- [82] W. Frei. *How much memory is needed to solve large COMSOL models?* COMSOL Blog. Accessed: July 13, 2016, <https://www.comsol.com/>.
- [83] T.-P. Fries. A corrected XFEM approximation without problems in blending elements. *Int J Numer Meth Engng*, **75**(5):503–532, 2008.

- [84] Kästner, M. and Müller, S. and Ulbricht, V. XFEM modelling of inelastic material behaviour and interface failure in textile-reinforced composites. *Procedia Mater Sci*, **2**:43–51, 2013.
- [85] M. Safdari, A.R. Najafi, N.R. Sottos, and P.H. Geubelle. A NURBS-based generalized finite element scheme for 3D simulation of heterogeneous materials. *J Comput Phys*, **318**:373–390, 2016.
- [86] D. Savvas, G. Stefanou, and M. Papadrakakis. Determination of RVE size for random composites with local volume fraction variation. *Comput Method Appl Mech Engng*, **305**:340–358, 2016.